POLITECNICO DI TORINO

Corso di Laurea Magistrale

in Ingegneria Energetica e Nucleare

Tesi di Laurea Magistrale

Experimental and Numerical investigation on the exploitability of Raschig Rings as heat transfer matrix for Concentrated Solar Power applications

Relatore:

Laura Savoldi

Correlatore:

Roberto Bonifetto

Candidato:

Antonio Bonvento

Anno Accademico 2018/2019

Abstract

In the context of Solar Towers, tubular receivers are among the most appealing absorber solution. This technology absorbs the solar radiation from the outer surface of the tubes allowing to warm up a working fluid that flows inside the absorber. At the commercial level, tubular receivers adopt liquid heat transfer fluid, like water and molten salts; however, they can easily work also with pressurized gases.

The use of a gaseous working fluid is a promising solution to improve effectively the tubular receiver performance since the gas has no upper temperature limits by itself, whereas the limits will obviously be set by the thermo-mechanics of the pipes. However, pressurized gases have a lower heat transfer coefficient with respects to liquids, which leads to higher temperatures of the tube wall and consequently higher thermal stresses. This limits the applicable solar incident heat flux on the absorber surface.

The cooling of surfaces exposed to very high heat fluxes is also common in the nuclear fusion field. In particular, the cavity of the gyrotron, a device used for the radio-frequency heating of the plasma in a Tokamak, experiences a local heat load deposition up to 20 MW/m^2. Therefore, to adequately cool the gyrotron, a solution based on a porous media made of Raschig Rings (RRs) used as a heat transfer promoter between the working cooling fluid and the gyrotron iteself has been proposed and investigated numerically at the Politecnico of Turin. A gyrotron mock-up equipped with aforementioned solution was manufactured by Thales Electron Devices (TED), entrusted to the Politecnico of Turin and tested at the Areva NP Technical Centre in 2015 and 2016 to assess the hydraulic and thermal performances of such device using water as working fluid.

Thanks to a cross fertilization with the nuclear fusion field, the aim of this Master Thesis is, to assess, both numerically and experimentally, the pure hydraulic and thermo-hydraulic performances of the above-said mock-up when using air as cooling fluid in Concentrated Solar Power applications. As a matter of fact, a test campaign at the Plataforma Solar de Alméria has been authorized and supported by the European Union's Horizon 2020 research and innovation programm: Solar Facilities for the European Research Area - Third Phase (SFERA III) under grant agreement N. 823802.

The test campaign has been prepared with the aid of a 3D computational model developed to numerically simulate the thermo-hydraulic properties of the mock-up. A suitable geometry, operating pressure, working fluid characteristics and flowrate were adopted.

First, a pure hydraulic model having no incident solar heat flux was utilized to compute the sample's pressure drop as a function of the flow-rate. Then, by introducing an incident gaussian-shaped solar heat flux into the model, the mock-up maximum and outlet temperatures were estimated in order to generate a thermo-hydraulic text matrix to be used as a guide line during the experimental campaign.

A maximum safe temperature of 400°C was chosen for the case.
The pure-hydraulic CFD model has been validated by means of the experimental data collected throughout the two weeks experimental campaign at the Plataforma Solar de Alméria, in the Solar Furnace SF-60. Thermo-hydraulic experimental data were also collected and analyzed.
With the successful validation of the computational model the hydraulic characteristic of the mock-up has been computed by comparing the previously taken pure hydraulic water experimental data collected at the AREVA center in 2015 and 2016 with the new air computed and experimental data collected at the PSA faciity in 2019. A good match, within the provided uncertainties, is achieved.

Acknowledgments

I acknowledge the financial support offered by the European Union's Horizon 2020 research and innovation programme: Solar Facilities for the European Research Area - Third Phase (SFERA - III) under grant agreement N. 823802.

I thank my supervisor, prof. L. Savoldi, who guided me throughout this Master Thesis, prof. R. Bonifetto, prof. R. Zanino, prof. J. Pye, PhD. students M. Cagnoli and A. Bertinetti.

I would like to thank all the staff of the Plataforma Solar de Alméria for the provided hospitality during the experimental campaign.

A heartfelt thanks to my family. I thank my father and my mother for supporting me all along my entire educational path, allowing me to focus on my studies and for helping me making my own experiences and becoming the person I am today. I thank my brother Giovanni for always taking care of my bureaucratic stuff, for being my "trip around the world" companion and for never letting me feel alone. I would also like to thank my grandparents, my cousins, my aunts and my uncles. A special thank also goes to my uncle Giuseppe and my aunt Sabina for being like a second parents here in Turin and for always having my back and supporting me and my needs.

Many thanks to all of my friends and to the people met during this part of my career who have shared this experience with me, Luca, Salvatore, Antonio G., Alessandro, Andrea and Antonio S.: your presence made these years a lot less harder.

I also wish to convey to the Alicata family my gratitude for the love and many moments they have shared with me. Last but definitely not least, I desire to express how I am deeply grateful to Federica, the person who more than anyone has stood by my side and that has been capable of understanding and supporting me any moment throughout difficulties. Thank you for having given me the fortitude of experimenting new ideas, get involved and for making me understand that, after all, obstacles are there to be overcome. These few lines will never be enough.

Index

List of Tables

List of Figures

1. Introduction

1.1 Concentrated Solar Power

Concentrating solar power (CSP) technologies use different mirror configurations to concentrate the sun's light energy onto a receiver and convert it into heat [1]. The sun's rays are used to heat a medium (usually a fluid or a gas) that is then used in a heat engine process (steam or gas turbine) to drive an electrical generator and produce electricity or used as industrial process heat. CSP uses only the beam component of solar radiation (direct normal irradiance), and so its maximum benefit tends to be restricted to a limited geographical range [2].
Concentrating solar power plants can integrate thermal energy storage systems that allow to generate electricity during cloudy periods or for hours after sunset or before sunrise. This attribute makes concentrating solar power stand out among other renewable energy technologies such as PV panels and wind mills that cannot use any storage [1].
CSP systems can also be combined with existing thermal-fired power plants that use coal, natural gas or even biofuels and can also be integrated with combined cycle power plants resulting in hybrid power plants which provide high-value, dispatchable power [1].
In some cases, CSP plants can also use fossil fuel to supplement the solar output during periods of low solar radiation. In those cases, a natural gas-fired heat or a gas steam boiler or re-heater is used [1].
A general scheme of the CSP technology is shown in Figure 1.1 where the three main logic blocks are highlighted.

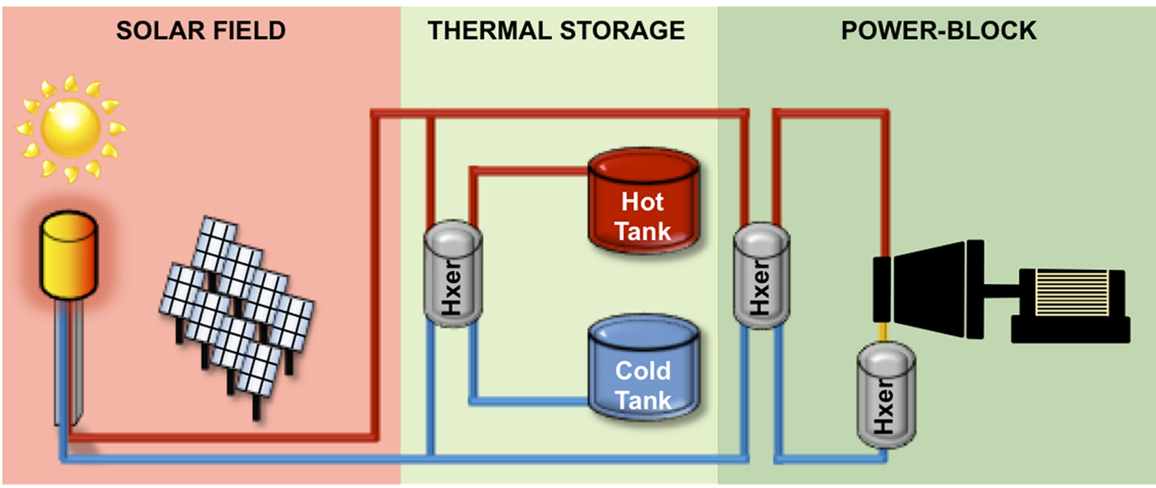

Figure 1.1: General logic block scheme of a CSP plant [3].

1.2 Types of CSP technologies

There are four types of CSP technologies used nowadays. For each of these, there are different design variations or several configurations, depending on whether thermal storage is included or not and on what methods are used to store the energy.

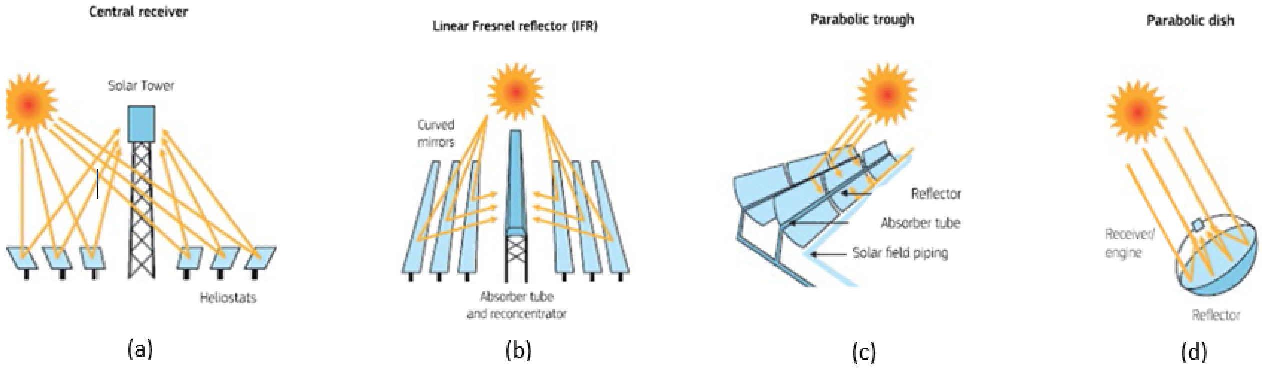

Figure 1.2: Layout of different Concentrated Solar Power configurations [4]

1.2.1 Parabolic Trough

In this system, being it the earliest to be used, the sun's energy is concentrated 70 to 100 times [4] by parabolic trough-shaped reflectors onto a receiver pipe running along the inside of the curved surface. The working fluid, usually diathermic oil because of its high boiling point, warms up as it flows inside of the absorber tube. The fluid is then pumped into a heat exchanger that transfers heat to water to produce steam.
A collector field comprises many troughs in parallel rows aligned on a north-south axis. This configuration enables the single-axis troughs to track the sun from east to west during the day to ensure that the sun is continuously focused on the receiver pipes [1].
A layout example of this system is shown in Figure 1.2 (c).

1.2.2 Linear Fresnel

This system produces a linear focus on a downward facing fixed receiver called absorber tube. Long rows of flat or slightly curved mirrors move independently on one axis to reflect the sun's rays onto the stationary receiver. The fixed receiver not only avoids the need for rotary joints for the heat transfer fluid, but can also help to reduce heat losses from the thermal receiver because it has a permanently down-facing cavity [5].
The attraction of the Linear Fresnel option is that the installation cost on a m^2 basis is low, however, other solutions have a higher annual optical performance [1].
A layout example of this system is shown in Figure 1.2 (b).

1.2.3 Parabolic Dish

Parabolic dish systems consist of a parabolic-shaped point focus concentrator that has a dish form and reflects solar radiation onto a receiver mounted at the focal point and connected to the rest of the structure. These reflectors have a two-axis tracking system to follow the sun throughout the day of the year and the hour of the day.
The collected heat is typically utilized directly by a heat engine mounted on the receiver moving with the dish structure. Stirling and Brayton cycle engines are currently favored for power conversion [5].
A layout example of this system is shown in Figure 1.2 (d).

1.2.4 Solar Tower

Power tower systems use a central receiver system, which allows reaching higher operating temperatures and thus a greater efficiency of the thermodynamic cycle downstream the receiver. Computer-controlled mirrors, called heliostats, track the sun along two axes and focus solar energy onto a receiver mounted at the top of a high tower. The focused energy is used to heat a working fluid (over 600°C [1]) to produce steam and run a central power generator.
Energy storage can be easily and efficiently incorporated into these projects, allowing for 24 hours power generation. This solution, however, requires a huge amount of area which is the real drawback of this technology that is still the one growing fastest [6].
A layout example of this system is shown in Figure 1.2 (a).
Several receiver designs have been proposed during the years for Solar Towers; among these the tubular receivers are probably the most mature technology, which have been deeply investigated from the early 80s with the Solar One and Solar Two projects at Sandia National Laboratory, USA.

1.3 CSP Global Potential

The project "Risk of Energy Availability: Common Corridors for European Supply Security" (REACCESS), under the European Commission Grant Agreement No.212011 evaluates technical, economical and environmental characteristics of present and future energy corridors within and among Europe and the supplying regions of the world, taking into account the different types of infrastructures and technologies like railways, pipelines, cables, terminals, ships and other carriers, the flows and the distances involved for oil, natural gas, coal, electricity, uranium, biomass and hydrogen. Within the REACCESS project an analysis of the technical potential of concentrating solar power (CSP) on a global scale was carried out [7].
The analysis is based on the annual direct normal irradiation data (DNI) provided by NASA Surface Meteorology and Solar Energy program (SSE) Version 6.0. It is based on 22 years of data and has a spatial resolution of about 100 km, which is considered sufficient to assess the potential of CSP plants on a global scale. The accuracy of the data is described on the SSE website [7] [8].
The result of the DNI assessment is shown in Figure 1.3.
The solar resource data has, then, been uploaded to a geographic information system and processed

together with spatial data on land use, topography, hydrology, geomorphology, infrastructure, protected areas etc. excluding sites that are not technically feasible for the construction of concentrating solar power plants.

The result yields a global map of DNI on land area that is potentially suited for the placement of CSP plants. Site exclusion criteria for CSP plants were applied world wide yielding a global exclusion map shown in Figure 1.4. Exclusion criteria comprise: slope > 2.1 %, land cover like permanent or non-permanent water, forests, swamps, agricultural areas, shifting sands including a security margin of 10 km, salt pans, glaciers, settlements, airports, oil or gas fields, mines, quarries, desalination plants, protected areas, restricted areas and already existing plants. Spatial resolution of the data was 1 km^2 [7].

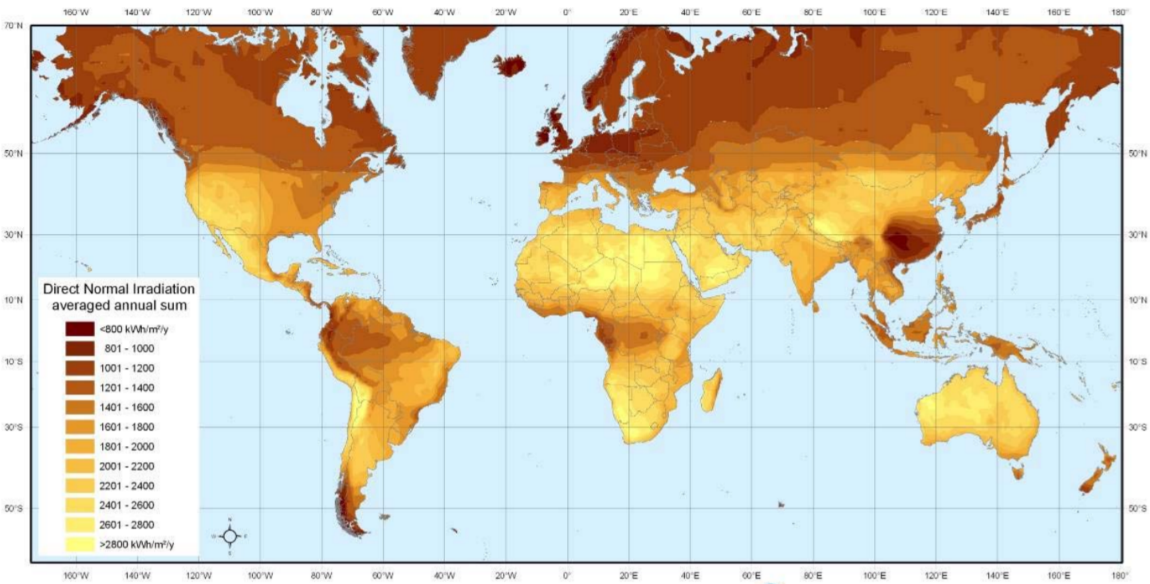

Figure 1.3: World wide annual direct normal irradiation in $kWh/m^2/y$ [7]

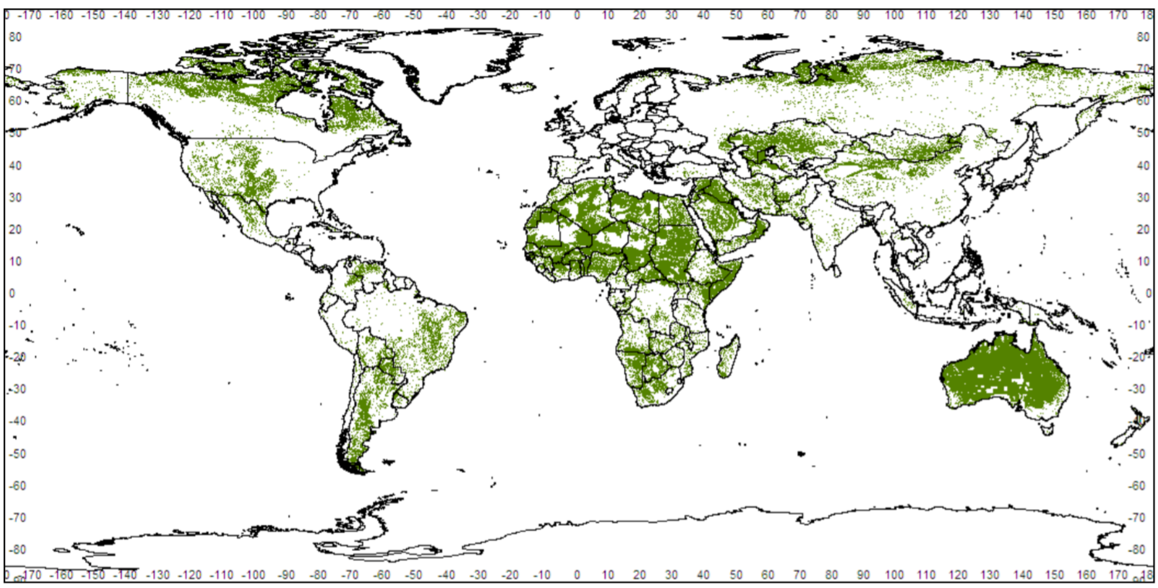

Figure 1.4: World wide exclusion of sites for CSP plant construction. Dark areas indicate suitable sites from the point of view of land suitability [7]

Both maps have, finally, been combined to yield a global map of annual direct normal irradiance for potential CSP sites, as shown in Figure 1.5. This map is subdivided according to the world regions defined within the REACESS project, considering only DNI intensity with values higher than 2000 $kWh/m^2/y$ [7].
The analysis shows that most world regions except Canada, Japan, Russia and South Korea have significant potential areas for CSP at an annual solar irradiance higher than 2000 $kWh/m^2/y$, while Africa, Australia and the Middle East have the largest potential areas, subsequently followed by China and Central and South America [7].

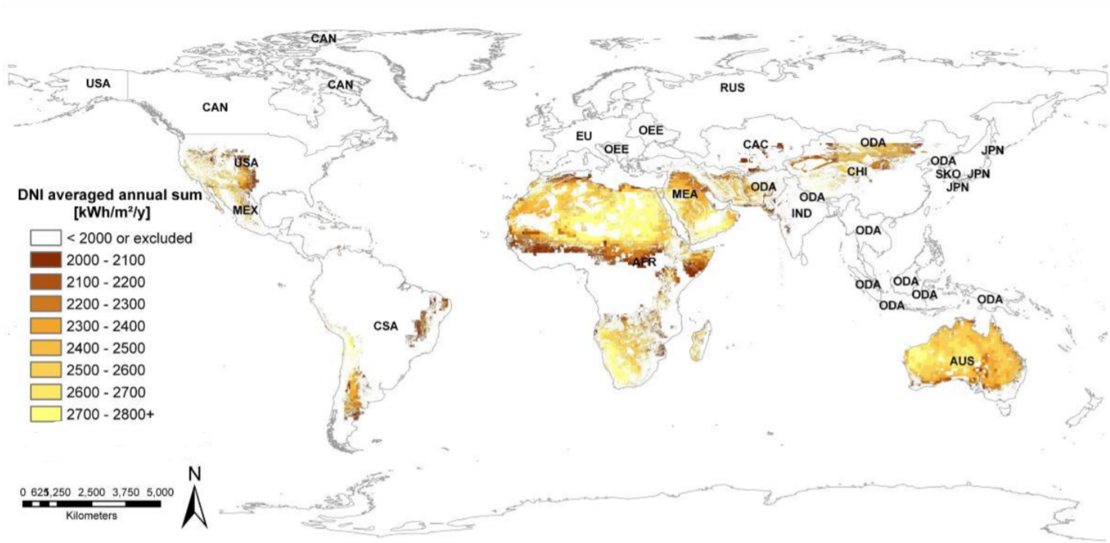

Figure 1.5: Resulting map of the annual sum of direct normal irradiation for potential global CSP sites [7]

1.4 CSP Global Capacity and Perspective

The commercial deployment of CSP plants initially started on 1984 in the USA. From 1991 to 2005, no CSP plant was built anywhere in the world. Global installed CSP capacity increased nearly tenfold between 2005 and 2013 and grew at an average of 50 percent per year during the last five of those years [9].
In 2013, the worldwide installed capacity increased by 49% or nearly 1.3 GW to a total value of more than 3.8 GW. Spain and United States remained the global leaders as can be seen in Figure 1.6. While the number of countries with installed CSP were growing the rapid decrease in price of PV solar, policy changes and the global financial crisis stopped most development in these countries.
Another productive year for CSP was 2014 but it was followed by a rapid decline with only one major plant completed in the world, specifically in South Africa, in 2016.
In 2018 CSP capacity increased by 11% led by China and Morocco, South Africa and Saudi Arabia. This annual increase represents the largest gain since 2013, and it occurred despite delays in several projects that had been scheduled to begin their operations in 2018 [10].
The cumulative CSP global capacity over the last decade is shown in general in Figure 1.6, while by

countries in Table 1.1.

By comparing the trend of the CSP development with other renewable sources, it is clear that CSP is now at a turning point. The mass-manufacture of PV systems and government subsidy schemes have resulted in the development of low cost high-efficiency multifunction cells. For CSP systems, the costs of mirrors, vacuum receiver, lenses, support structure, high-efficiency heat transfer fluid and turbine have affected the initial and operational costs of the CSP project significantly and result not competitive in most scenarios. In the most optimistic scenarios, CSP systems could supply around 10% of global electricity. However most of the scenarios are pointing out that deployment of CSP plants would remain slow in the next 10 to 15 years compared with previous expectations [11].

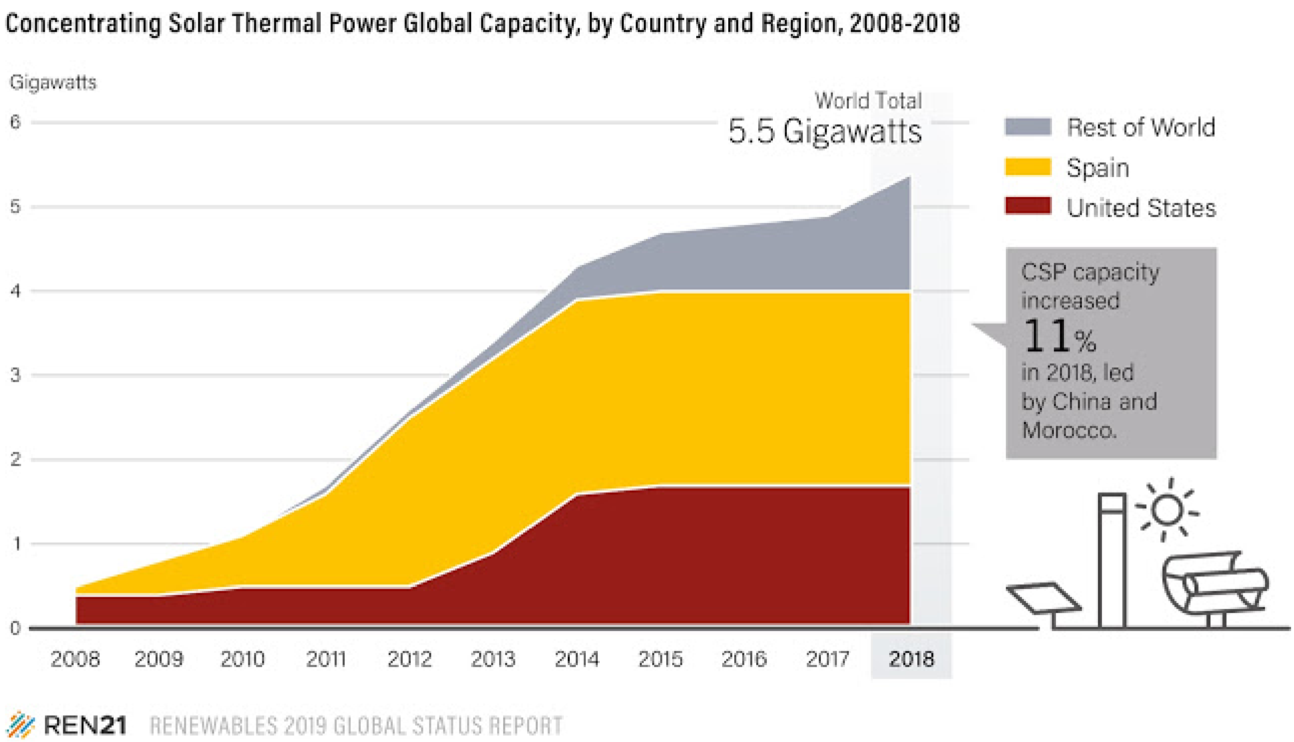

Figure 1.6: Concentrating Solar Thermal Power Global Capacity, by Country and Region, 2008 - 2018 [10]

Table 1.1: CSP Capacity [MW] by countries [12].

	Country	2008	2009	2010	2011	2012	2013	2014	2015	2016	2017
Africa		-	-	45	65	65	65	165	325	425	525
	Algeria	-	-	25	25	25	25	25	25	25	25
	Egypt	-	-	-	20	20	20	20	20	20	20
	Morocco	-	-	20	20	20	20	20	180	180	180
	S. Africa	-	-	-	-	-	-	100	100	200	300
Asia		-	-	3	8	16	73	248	248	248	248
	China	-	-	3	5	8	14	14	14	14	14
	India	-	-	-	3	4	54	229	229	229	229
	Thailand	-	-	-	-	5	5	5	5	5	5
Eurasia		-	-	-	-	-	1	1	1	1	1
	Turkey	-	-	-	-	-	1	1	1	1	1
Europe		61	284	739	1156	2007	2307	2308	2308	2308	2308
	Germany	-	2	2	2	2	2	2	2	2	2
	Italy	-	-	5	5	5	5	6	6	6	6
	Spain	61	282	732	1149	2000	2300	2300	2300	2300	2300
Middle East		6	6	6	6	6	106	106	106	106	106
	Israel	6	6	6	6	6	6	6	6	6	6
	Arab Em.	-	-	-	-	-	100	100	100	100	100
N. America		465	472	473	472	476	1286	1667	1758	1758	1758
	USA	465	472	473	472	476	1286	1667	1758	1758	1758
Oceania		3	3	3	3	3	3	3	3	6	6
	Australia	3	3	3	3	3	3	3	3	6	6
World		535	765	1269	1710	2573	3841	4498	4749	4851	4951

1.5 Air Tubular Receivers

In the contest of Solar Towers tubular receivers are probably the most appealing absorber solution. In particular, this technology absorbs the solar radiation from the outer surface of the tubes allowing to warm up a working fluid that flows inside the absorber.
At the commercial level, tubular receivers adopt liquid heat transfer fluid, like water and molten salts; however, they can easily work also with pressurized gases, as demonstrated for example in the SOLHYCO project [13].
An example of the SOLHYCO tubular receiver is shown in Figure 1.7.
The use of a gaseous working fluid (typically pressurized air) is a promising solution to improve effectively the tubular receiver performance, since the gas has no upper temperature limits by itself, whereas the limits will obviously be set by the thermo-mechanics of the pipes. In addition to this, a gas turbine can be directly driven by the solar field, allowing the implementation of a solar-driven combined cycle.
The use of air as a cooling working fluid surely has several advantages, however, on the other hand, pressurized gases have a lower heat transfer coefficient with respects to liquids, which leads to higher temperatures of the tube wall and consequently higher thermal stresses. This limits the applicable solar incident heat flux on the absorber surface.
A way to reduce the peak temperature is to enhance the convective heat transfer between the tube wall

and the coolant. This option was explored in the aforementioned SOLHYCO project [13], where a wire coil was inserted inside the tubes to improve the heat transfer towards the coolant.

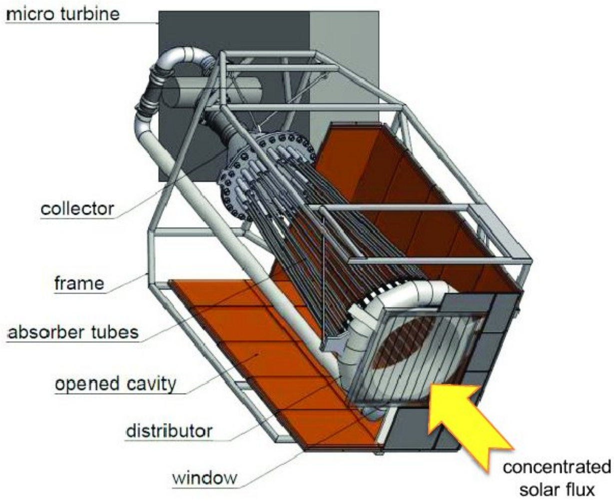

Figure 1.7: Example of solar cavity tubular receiver, SOLHYCO project [14]

1.5.1 Porous Media and Enhanced Heat Transfer

An alternative way of enhancing the convective heat transfer, with respect to the case studied by the SOLHYCO project, is to insert a porous medium under the irradiated surface [15]. This allows to increase the useful heat transfer surface and to enhance the turbulence of the coolant, resulting in an improved convective heat transfer between the tube and the coolant. An improved heat removal allows to lower the temperature of the outer wall surface leading to a reduction of both convective and radiative heat losses as well as the thermal stresses of the tube. Additionally, this allows to increase the aforementioned maximum applicable solar incident heat flux on the absorber surface or to reduce the absorber area at equal incident solar power.

The drawback of filling the absorber tube with a porous medium is the increased pressure drop across the tube. This issue was also numerically analysed by Zheng et al in [16] for a tubular receiver cooled with molten salts; In his study it was proposed to partially fill the tube with the porous medium according to the non-uniform heat flux distribution. The optimized design resulted from a trade-off between improved heat transfer and increased pressure drop.

It is worth mentioning that the literature contains a large number of numerical investigations and a very small number of experimental studies on the use of porous materials for both natural and forced flow applications.

Al-Nimr and Alkam [17] numerically investigated the problem of transient forced convection flow in a concentric annuli partially filled with porous substrates located either on the inner or the outer cylinder. An increase of up to 12 times in the Nusselt number was reported in comparison with the clear annuli case and the superiority in thermal performance of the case when the porous substrate was emplaced to the inner cylinder was outlined. Based on the results obtained, Alkam and Al-Nimr [18] further investigated the thermal performance of a conventional concentric tube heat exchanger by emplacing porous substrates on both sides of the inner cylinder. Numerical results obtained showed

that porous substrates of optimum thicknesses yield the maximum improvement in the heat exchanger performance with moderate increase in the pumping power. Recently, Mohamad [19] numerically investigated the heat transfer augmentation for flow in a pipe or a channel partially or fully filled with porous material emplaced at the core of the channel. It was shown that partially filling the channel with porous substrates can reduce the thermal entrance length by 50% and increase the rate of heat transfer from the walls.
The following lines briefly present the results obtained by authors who carried out experimental tests on porous media.
Ichimiya [20] proposed a new method for evaluation of the volumetric heat transfer coefficient between the solid material and fluid in a porous medium by conducting both experimental and numerical work. Fu et al. [21] experimentally demonstrated that a channel filled with large-conductivity porous material subjected to oscillating flow is a new and effective method for cooling electronic devices. Angirasa [22] performed experiments that proved the augmentation of heat transfer by using metallic fibrous materials with two different porosities, namely 97% and 93%. The experiments were carried out for different Reynolds numbers (17,000–29,000) and power inputs (3.7 and 9.2 W) and showed an increase in the value of the Nusselt number of about 3–6 times in comparison with the case when no porous material was used. Finally, Pavel and Mohamad [23] experimental and numerical work investigated the effect of metallic porous materials, inserted in a pipe, on the rate of heat transfer. The results obtained, which were compared with the clear flow case where no porous material was used, lead to the conclusion that a heat transfer enhancement can be achieved using porous inserts whose diameters approach the diameter of the pipe. Additionally, for a constant diameter of the porous medium, further improvement can be attained by using a porous insert with a smaller porosity and higher thermal conductivity, while care should be exercised since both R_p (i.e. the porous material radius radio: radius of the porous material over the internal radius of the pipe) and the porosity have a positive influence upon heat transfer and a negative impact on pressure drop, consequently on the pumping power.

1.5.2 Raschig Rings Porous Media

In order to use a tubular receiver that operates with air as cooling working fluid, a heat transfer enhancement is definitely needed to avoid high wall temperatures and excessive thermal stresses. As presented in 1.5.1, a valid solution to achieve that enhancement is to place a porous media inside of the absorber tube, below its surface exposed to the sun.
Thanks to the cross fertilization from the nuclear field, see 1.6, this study proposes a porous media made out of Raschig Rings (RRs) to be located under the irradiated surface.
Raschig Rings are pieces of tube, approximately equal in length and diameter, used in large numbers often as a packed bed within columns for distillations and other chemical engineering processes. They are usually made of a ceramic material or metal and provide a large surface area within the given volume. In the following particular case of interest, see 1.7.1, the RRs are made of copper and they are brazed together in order to held and freeze them in the right position. However, this procedure might modify some RRs thermal properties such as their thermal conductivity.

The geometrical properties of the used RRs are shown in Table 1.2 while a geometrical scheme of a single RR is shown in Figure 1.8.

Table 1.2: RRs geometrical properties

	Dext	Thickness	Height	Volume
RRs Properties	2 $[mm]$	0.2 $[mm]$	2 $[mm]$	2.26 $[mm^3]$

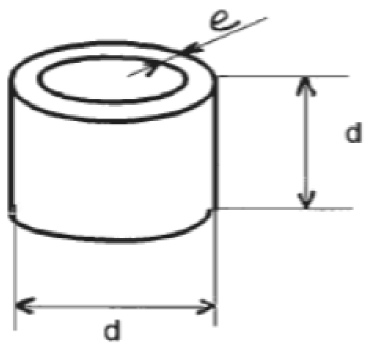

Figure 1.8: Schematic view of a single RR: d = Dext = Height, e = thickness

In Figure 1.9 below is represented an example of what a CSP air cavity tubular receiver should look like with the Raschig Rings heat transfer enhancement solution.

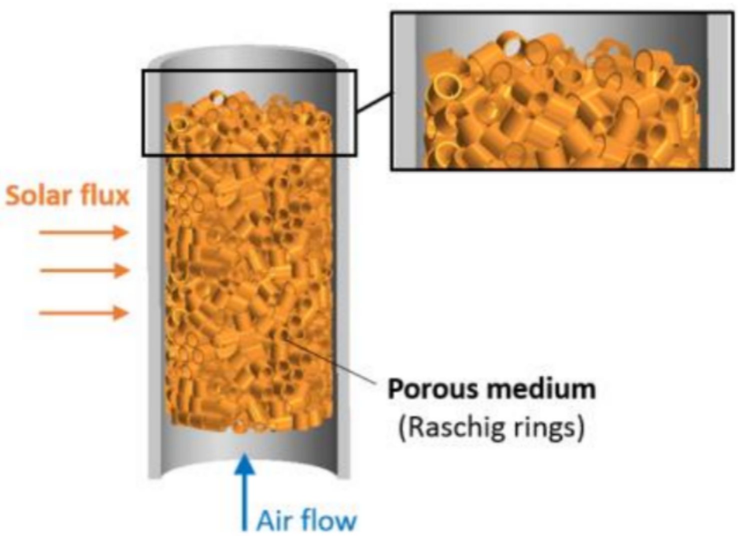

Figure 1.9: Raschig Rings Enhanced Receiver Scheme

1.6 Technology Cross Fertilization

The Cross Fertilization is a mutual exchange of both information, experience and, generally speaking, knowledge that takes place between different concepts, cultures or disciplines that enhances the understanding or produces something beneficial.
As a matter of fact, this entire study, as was previously anticipated in 1.5.2, is based on a technology

cross fertilization between two, only apparently, different sectors: Nuclear Fusion Field and Concentrated Solar Power (CSP) Field.
The cooling of surfaces exposed to very high heat fluxes is, in fact, also common in the nuclear fusion field. In particular, the cavity of the gyrotron, a device used for the radio-frequency heating of the plasma in a Tokamak, experiences a local heat load deposition up to 20 MW/m^2. Therefore, to adequately cool the gyrotron, a solution based on a porous media aiming at enhancing the heat transfer coefficient between the working cooling fluid and the gyrotron iteself was proposed and analyzed. Thanks to aforementioned cross-fertilization said solution might be applied to a CSP technology such as a tabular cavity absorber tube.

1.6.1 RRs Mock-up with water as cooling fluid

A solution based on a porous medium located under an irradiated surface has already been proposed and investigated numerically at the Politecnico of Turin [24].
Precisely, a mock-up of the gyrotron cavity with a porous media inside was manufactured by Thales Electron Devices (TED), tested at the Areva NP technical Centre in 2015 and 2016 to assess the hydraulic and thermal performances of such a device using water and entrusted to the Politecnico of Turin for further and possible tests. The porous given volume located under the irradiated area was filled with many Raschig Rings which were then brazed together to be held in place and to create a solid structure. Said structure grants a porosity of approximately 35%.
An example of such tested device is shown below in Figure 1.10, where almost all of the geometrical dimensions are represented (see 2.1.1 for the remaining dimensions concerning the RRs block).
The external envelopment of the mock-up is made of copper just like the RRs, as said in 1.5.2, the part of the structure just below the RRs block, the one that is directly heated, is instead made of Glidcop® (a family of copper-based metal matrix composite alloys mixed primarily with small amounts of aluminum oxide ceramic particles).
A safe maximum temperature of 400 °C was thus chosen in order to avoid any type of damage onto the mock-up [24] or its complete (or partial) melting.

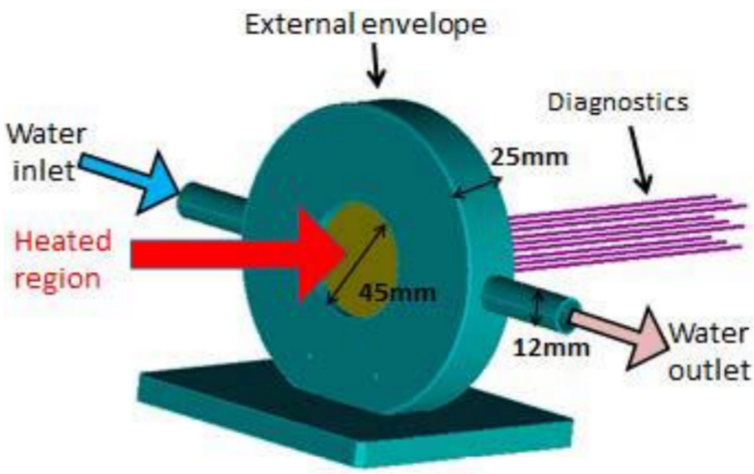

Figure 1.10: Raschig Rings Enhanced Mock-up with water as cooling fluid [25].

The target region of the mock-ups has been heated by means of an electron beam with a power density up to $30\ MW/m^2$. The temperature of the heated surface was measured by a pyrometer and the temperatures inside the mock-up were measured by a set of 11 thermocouples installed in proximity of the target region (9 out of 11), inlet (1 out of 11) and outlet (1 out of 11) of the mock-up itself.

1.7 Aim of the Thesis

Today most of the commercial solar receivers are based on the cavity tubular technology which mainly use liquid heat transfer fluids like water or molten salts. To improve effectively the tubular receiver performance the use of a gaseous working fluid like air is a promising solution having several advantages despite its few disadvantages as discussed in Section 1.5. In order to utilize such gaseous operating fluid a solution to enhanced the heat transfer between the absorber and the cooling fluid is necessary.
Thanks to the cross-fertilization with the nuclear field, said solution might be found into a Raschig Rings porous media to be located below the irradiated surface.
The aim of this thesis investigation is to make a complete study of such technology and to assess, both numerically and experimentally, the pure hydraulic and thermo-hydraulic performances of aforementioned mock-up when using air as cooling fluid. As a matter of fact, a test campaign at the Plataforma Solar de Alméria (PSA) has been authorized and supported by the European Union's Horizon 2020 research and innovation programm: Solar Facilities for the European Research Area - Third Phase (SFERA III) under grant agreement N. 823802.
Specifically, the maximum temperature reached on the heated surface (measured using an IR camera) of the mock-up during the test campaign could, then, be compared with its air outlet temperature. The smaller the difference between the two, the better the cooling performance provided by the technology and therefore its enhancement of the heat transfer coefficient. As final goal, if a good efficiency is proven, this technology could be applied to absorbers of the tubular kind resulting into the design of a new, thermally enhanced, concentrated solar power receiver.
Additionally, the outcomes of this analysis will also make possible to compare the Raschig Rings technology with the standard (smooth) absorber tube in terms of thermal performances.
This Master Thesis aims to achieve a complete definition of the CFD model to numerically describe above-said technology and to collect sufficient and suitable pure hydraulic and thermo-hydraulic experimental data. Furthermore, a comparison between the pure hydraulic computed and experimental data is made to validate the model and to determine the hydraulic characteristic of the RRs mock-up. With further investigations a validation of the thermo-hydraulic model could be obtained by means of the thermo-hydraulic experimental results collected at the PSA and a first porous tubular receiver manufactured.

1.7.1 RRs Mock-up with air as cooling fluid

The thermal-hydraulic qualification of the mock-up adopting pressurized air as working fluid, targeted at its applications in a solar cavity tubular receiver, is proposed and investigated in this manuscript to

assess the cooling performance of the Raschig Rings technology.
The followed logical procedure adopted in each of the following chapters is briefly presented below.
The thermal-hydraulic performance of the mock-up (sample) will, firstly, be analyzed numerically by means of suitable computational-fluid-dynamic (CFD) simulations based on the Discrete Element Method (DEM). A mesh independence study will be done to fully assess the relative error associated to each simulation. Computed results will be collected using both a pure-hydraulic and, subsequently, a thermo-hydraulic model.
The two weeks experimental campaign at the Plataforma Solar de Almeria (PSA), Solar Furnace 60 (SF60) with the SFERA III Horizon 2020 Project will, then, be presented. The sample will be tested at the spanish solar furnace facility where it will be cooled by means of a pressurized air flow. Pure hydraulic and thermo-hydraulic experimental data will be collected. A full analysis of the results will be included.
Finally, a comparison between computed and experimental data will follow, together with a validation of the pure-hydraulic computational model. The mock-up hydraulic characteristic will be reported including the previously taken (see [24]) water experimental results.
More generally, the first step mentioned above is fundamental in order to check that no dangerous temperatures (close to the mock-up melting temperature) will be reached during the experimental campaign at the PSA.
A safe maximum temperature of 400 °C was chosen consistently with what said in 1.6.1.
The temperature measured by the different thermocouples (9 inserted right into the RRs block and 2 to evaluate the air temperature at the inlet and outlet, respectively) inserted in the porous structure will provide additional data for the CFD model validation and could be used to numerically optimize the receiver layout evaluating the best trade-off between pressure losses/pumping power and efficient heat transfer.

2. CFD model of the mock-up

The simulations on the mock-up model are performed with the commercial software STAR-CCM+ v. 10 and STAR-CCM+ v.13 [26];

2.1 Structure of the Mock-up CFD Model

During the two weeks experimental campaign at the Plataforma Solar de Almeria, alongside thermal hydraulic tests also pure hydraulic ones will be performed. In fact, while the former type is fundamental to investigate the exploitability of the Raschig Rings as heat transfer matrix and to have a first idea of its thermal behaviour before the actual testing phase, the latter type is needed to extrapolate a hydraulic characteristic of the mock-up being its pressure loss the main, and therefore most important, drawback of this technology.
As a matter of fact, both complete Pure Hydraulic and Thermo-Hydraulic versions of the CFD Model are made so that simulated results can be compared with the experimental ones and thus validate the model if a match is found.
Hereby are presented both a schematic and realistic views of the RRs mock-up working with air as cooling fluid in Figure 2.1 and Figure 2.2, respectively. Subsequently follows an explanation of how the entire structure of these two CFD models is built.

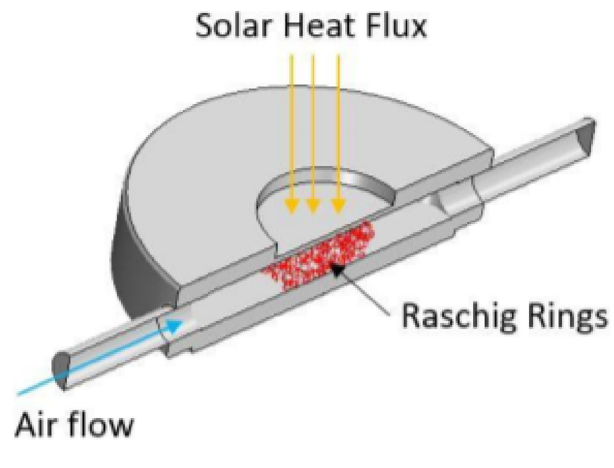

Figure 2.1: Schematic view of the RRs air mock-up.

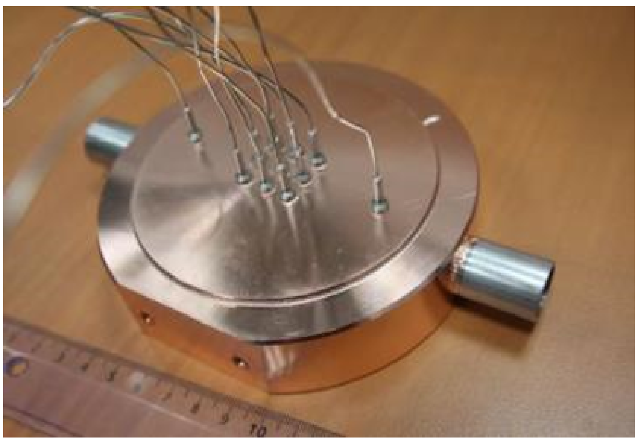

Figure 2.2: View of the RRs air mock-up.

2.1.1 Geometry

The geometry used in the simulations is shown in Figure 2.3 where also the dimensions of the RRs block are presented. The dimensions of the target area, inlet and outlet tube are instead already shown in Figure 1.10. The hereby presented geometry will be used for both pure hydraulic and thermo-hydraulic simulations. The only difference between the real mock-up and the simulated geometry, however, are the 11 thermocouples that are not represented in the simulations.
Symmetry of the geometry, boundary conditions for the solid domain and drivers allow the simulation of just half of the mock-up, this allows to reduce the computational cost of each simulation, resulting in a much more time efficient solution [27].

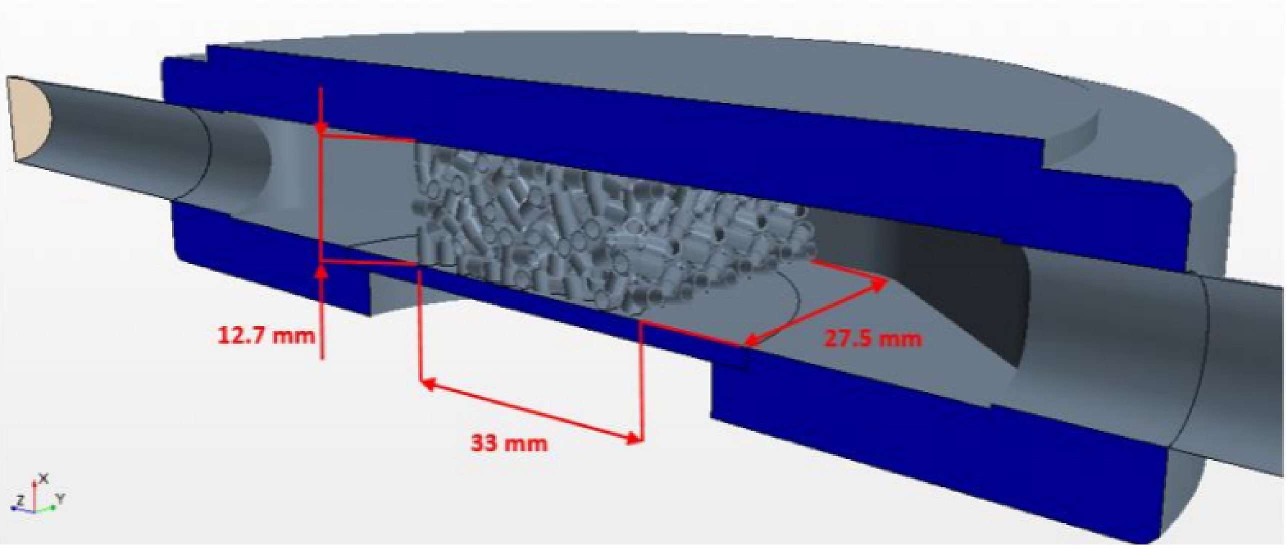

Figure 2.3: Scheme of the simulated Mock-up Geometry [28].

The computational domain of the RRs region inside the mock-up has been built according to the procedure described in [24] using the commercial software STAR-CCM+ v. 10 and is briefly recapped below:

1. The geometrical model of a single RR is created;
2. An empty injection module is defined, (corresponding to 1/3 of the total volume occupied by the RRs to save computational time), see Figure 2.4 a;
3. The module is progressively filled with RRs, until no room is left to inject further RRs, see Figure 2.4 b;
4. The module with the RRs is replicated to cover the entire relevant volume, see Figure 2.4 c;
5. The RR region is assembled with the rest of the cooling structure; see the cavity mock-up in Figure 2.3.

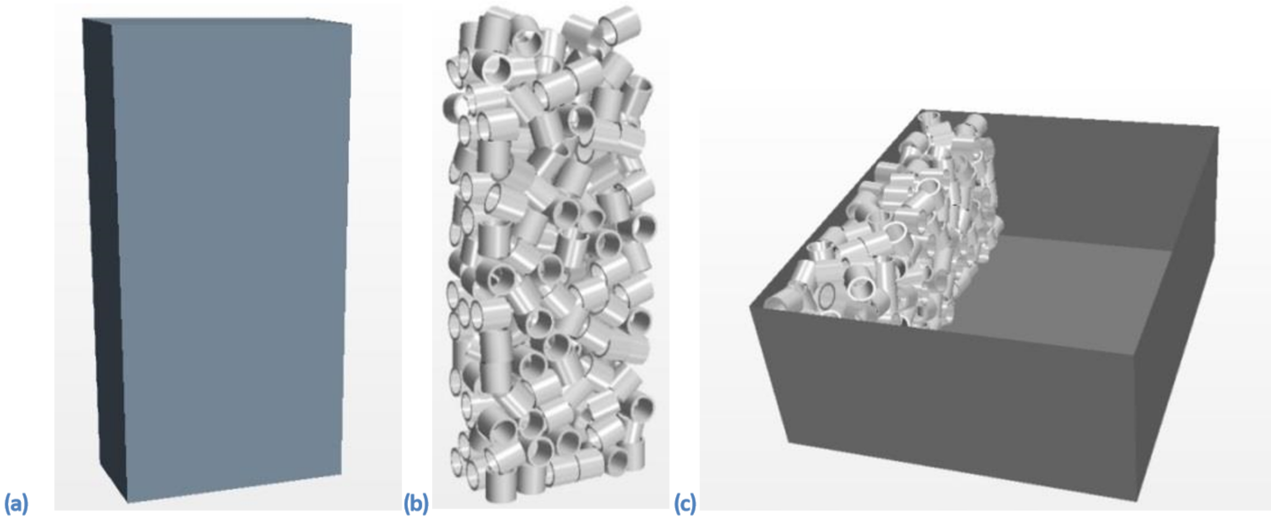

Figure 2.4: Cavity mock-up RRs blockp: empty injection module (a), filling with RRs (b), RR module ready for replication (c).

2.1.2 Model and Simulation Setup

It is clear that, being the pure hydraulic model less complex than the thermo-hydraulic one since there is no heat flux of any kind applied to any of the former model surfaces, the computation models used here have to differ a little from the latter. Specifically, the easiest and fastest thing to do was to still include into the pure hydraulic simulations all the same models of the thermo-hydraulic simulations, but pausing the Energy Solver so that the entire problem would be treated as pure hydraulic. Additionally, this will also help to make the former model much lighter and faster from a computation cost point of view.
All the models used for the setup of the different simulations are hereby listed.

Glidcop® (material properties as from Appendix A):

- Three Dimentional;
- Steady State;
- Segregated Solid Energy;
- Gradients, Hybrid Gauss-LSQ;

Air (material properties as from Appendix A):

- Three Dimentional;
- Steady State;
- Segregated Flow;
- Segregated Fluid Temperature;

- Gradients, Hybrig Gauss-LSQ;
- Ideal Gas;
- Turbulent, $k - \omega$ SST (Menter) [1];
- All y+ wall treatment;

2.2 Mesh Generation

The meshing process is an important step of any CFD analysis, therefore its study is, hereby, carefully carried out.
In general, a Mesh or Grid can be either created in 3 or 2 dimensions. The 2-dimensional mesh usually includes simple polygons of different shapes, while in 3-dimentions the simple polygons become polyhedrons [29]. A finer discretization of the domain means having more polygons (or polyhedrons), leading to more precise results; on the other hand, having a finer mesh also increases the computational cost of the simulation, which usually means that more time is needed.
To generate the mesh the software STAR-CCM+ v.13 includes a function called Prism Layer mesher which allows to generate different layers of prisms of a selected thickness on the domain surfaces where this option is chosen. This usually improves the near-wall results where many of the most important phenomena happen, without increasing too much the computational cost of the entire simulation. Unfortunately, because of the complex RRs geometrical domain, this option was not included inside of the simulations since the software itself has problems creating such a mesh in the RRs block section and it would have just caused some errors leading, in the end, to less precise results.
In the end, the utilized grid uses a normal polyhedral mesh function. This chosen mesher allows to select different parameters such as the mesh base size and the surface growth rate.
An automated surface repair function is also included to automatically correct errors made by the software while generating the mesh.
All of the equations and models previously described in 2.1.2 are then applied to each of the polyhedron in which the domain is divided into.
A common procedure is to adjust the mesh just in specific areas, making it finer in order to have more precise results in spots of interest without increasing too much the computational time. This is the case, in fact, of the RRs mock-up simulations where the mesh was made finer just in specific volumes. Specifically, to get a better grid, the base size of the mesh cells was reduced in such volumes. In particular, in two volume regions located before and after the RRs block a cell base-size which is smaller than the nominal one has been selected, while in the volume region containing the RRs block an even smaller cell base-size has been selected instead (see Table B.1).
These different volume regions are shown in Figure 2.5 and Figure 2.6 respectively.

[1] The $k - \omega$ SST model was preferred because of its largely demonstrated validity and for its higher near wall precision which is considered to be fundamental thoughout this study work

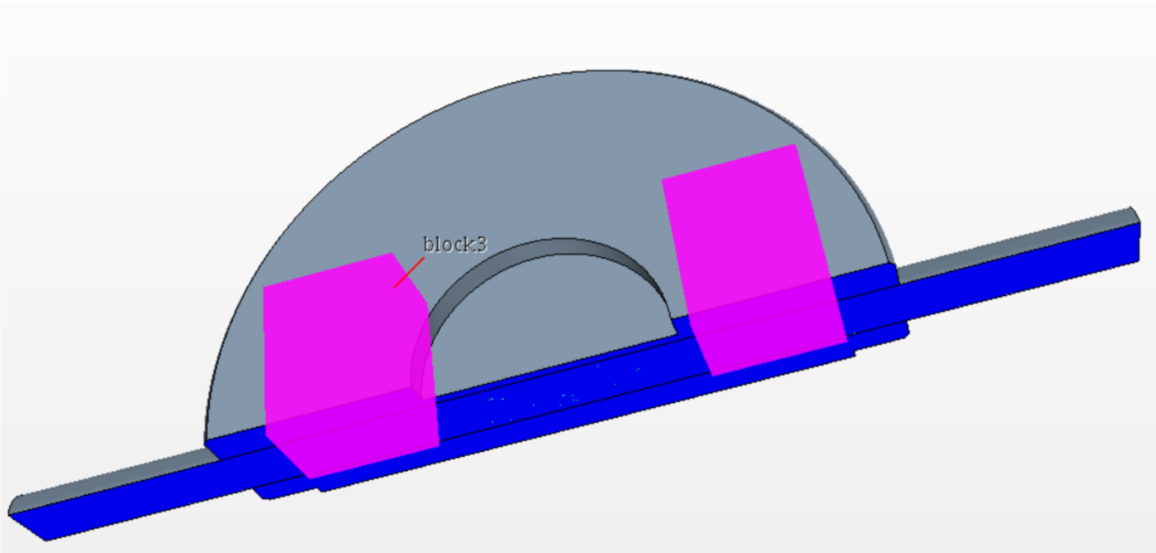

Figure 2.5: Volume regions before and after the RRs block with a smaller cell base size.

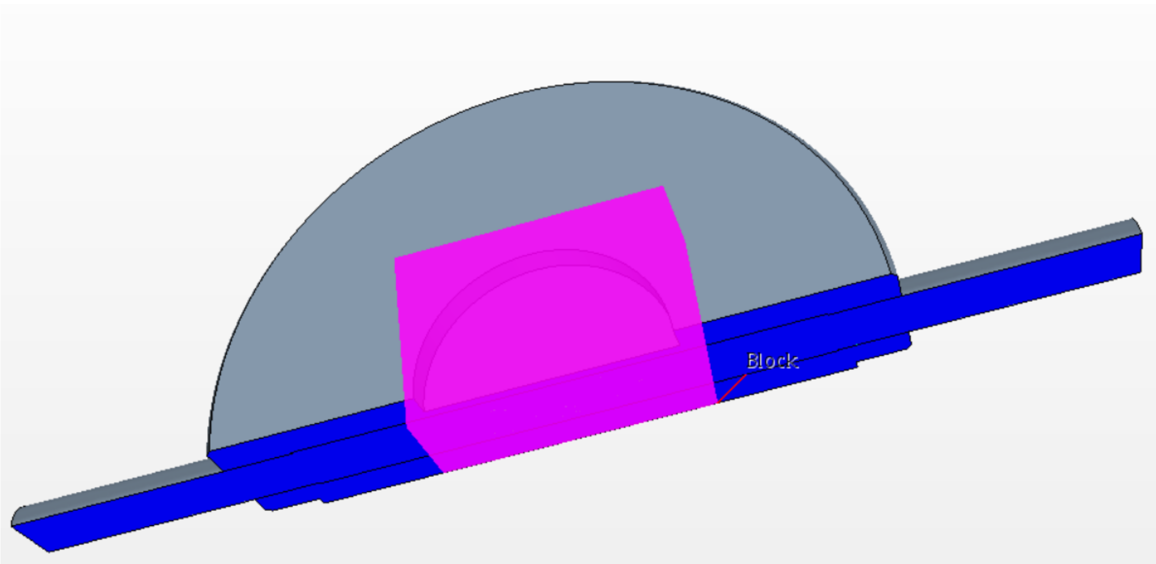

Figure 2.6: Volume region containing the RRs block with the smallest cell base size.

2.2.1 Mesh Independence

As mentioned in the previous Section 2.2, the finer the mesh the more precise the results are.
The finest possible mesh does not imply to be the best possible grid for a specific simulation. As a matter of fact, there is a limit after which is not worth anymore to make the mesh finer as the results will then be more precise of a negligible small amount costing a huge increase of computation cost and therefore of the time needed.
In order to avoid such waste of time and to save computational cost is crucial to perform a mesh independence: an analysis that shows what is the best number of cells and the best mesh to have the most precise results at the lowest possible computational cost. Thus, this analysis is a trade-off between trustable results and low run-time per simulation.
The detailed Mesh Independence study is reported in Appendix B.
The geometry of the simulation is quite complex because of the RRs block, in fact, it is not trivial

to make a good CAD representation of the real mock-up. The procedure used to create the RRs block is explained in 2.1.1 (see also Figure 2.4), this method includes a step where a certain volume is completely filled with RRs until a certain porosity is achieved. This filling step is based on a random algorithm which collocates every RR randomly inside the selected fixed volume. The use of a random algorithm might, sometimes, be a risky choice since is then fundamental to asses how much every value (Temperature, Velocity, etc.) depends on that specific random pattern.
A sensitivity analysis on the RRs mesh has also been performed as reported in Appendix C.
Finally, the chosen mesh to be used for further investigations is a 2.4 million cells mesh. In fact, even if the relative error pattern of each variable starts to become flat (see Figure B.5 to Figure B.12) from the 3.5 million cells mesh, the relative error is already low enough in the 2.4 million one; a relative error of around 1% in almost every value is, indeed, a very good achievement. The only two values that have a higher error are the Pressure Drop (slightly below 2%) and the Maximum Air Velocity (around 5%, being it less meaningful considering that the values might be located in only one of the 2.4 million cells). The determining factor is, however, not the relative error but the time needed to converge. The 2.4 million cells takes around 4 full days per simulation to converge, whereas the 3.5 million cells takes around 7 full days per simulation. Having to run dozens of simulations to make a first computed test matrix scheme, saving 3 days per simulation losing just less than 1% of results precision seems a very good trade-off and compromise.
Surely, the 3.5 million cells mesh is more precise than the 2.4 million one, but choosing the latter over the former certainly allows to save almost up to two entire month of simulation time maintaining all the results on a sufficient and satisfying level.
An example of the chosen mesh is shown in Figure 2.7, 2.8 and 2.9.

Figure 2.7: Side view of the air RRs mock-up with the chosen 2.4 million cells Mesh.

Figure 2.8: Frontal view of the air RRs mock-up with the chosen 2.4 million cells Mesh.

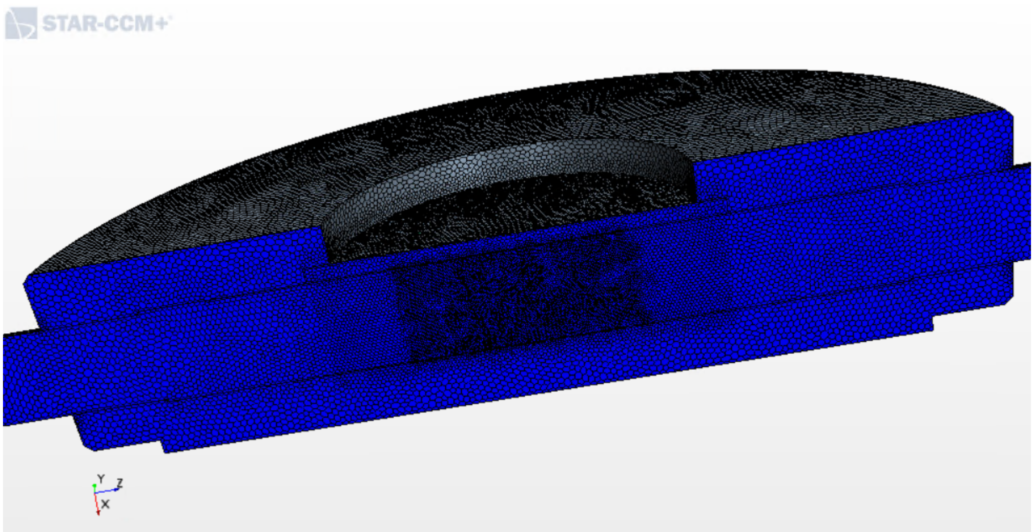

Figure 2.9: View of the air RRs mock-up with the chosen 2.4 million cells Mesh, RRs Block particular.

2.2.2 Boundary Conditions and Drivers

Different but still similar boundary conditions were applied on both pure hydraulic and thermo-hydraulic simulations depending on their physics.

Pure Hydraulic Boundary Conditions:

- Inlet Mass Flow Rate, applied on the inlet area, depending on the simulation;
- Outlet Pressure $p_{out} = 0$ bar, applied on the outlet area;
- Reference Pressure $p_{ref} = 10$ bar, applied on the entire geometry;
- Flow Rate Inlet Temperature $T_{in} = 290K$;
- No incident heat flux on any mock-up surface;

Thermo-Hydraulic Boundary Conditions;

- Inlet Mass Flow Rate, applied on the inlet area, ranging from $5.375 \cdot 10^{-4} kg/s$ up to $10.75 \cdot 10^{-3} kg/s$ depending on the simulation;
- Outlet Pressure $p_{out} = 0$ bar, applied on the outlet area;
- Reference Pressure $p_{ref} = 10$ bar, applied on the entire geometry;
- Flow Rate Inlet Temperature $T_{in} = 300K$;
- Gaussian Solar Heat Flux applied on the circular target area (see Figure 1.10) of the mock-up. The adopted Gaussian function is shown in Figure 2.10, the peak flux ranged from 100 kW/m^2 up to 700 kW/m^2 depending on the simulation ;
- Convective Heat losses with a convective heat transfer coefficient $h = 10W/m^2/K$, applied on every dispersing surface (M. Cagnoli private communication 2019);
- Radiative Heat losses with an emissivity $\epsilon = 0.9$, applied on every dispersing surface (A. Bertinetti private communication 2019);

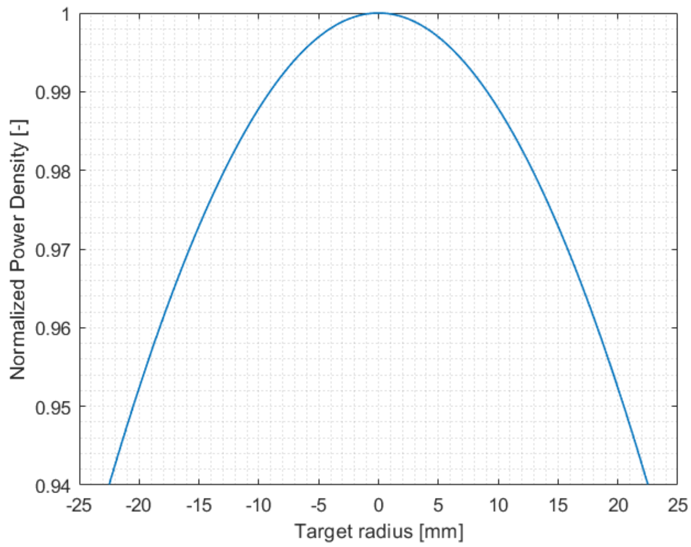

Figure 2.10: Normalized Gaussian Flux Function applied on the mock-up target.

The gaussian function is applied in such a way that the peak of the flux corresponds to the centre of the target area, while the minimum value corresponds to the border of the same area, accordingly to what is shown in Figure 2.10.
The standard deviation adopted here is $\sigma = 0.064$, since it has shown to be the one that fits the best with the concentrated solar irradiation that will be applied on the same area during the experimental campaign.
The convective heat transfer coefficient $h = 10W/m^2/K$ was chosen since the convective loss is only due to still air natural convection, whereas the emissivity $\epsilon = 0.9$ was chosen because of a special coating treatment done on the mock-up by the manufacturer (M. Cagnoli and A. Bertinetti private

communication, 2019).

A sensitivity analysis check was performed on both the convective heat transfer coefficient and emissivity as shown in 3.0.1 and 3.0.2, respectively.

3. Simulation results: The Thermo-hydraulic Test Matrix

The Grid Independence analysis assessed what the best mesh to describe the mock-up is (obtained by a trade off between computational time and results precision). Consequently, to generate and compute a preliminary Thermo-Hydraulic Test Matrix Map the hereby presented study is needed.
This investigation is an additional fundamental step in which different parameters are changed, one at a time, into the simulations in order to fully assess the thermofluid-mechanic behavior of the CFD air mock-up model. The two main parameters that are hereby changed are the air flow-rate (ranging from 25 lt/min up to 400 lt/min) and the peak of the solar heat flux (ranging from 100 kW/m^2 up to 700 kW/m^2). Mapping the thermofluid-mechanic properties of the mock-up is useful for more than just one reason. In fact, first and more importantly, it gives an initial idea of what conditions might be dangerous for the mock-up since, as said in 1.7.1, a safe maximum temperature of 400 °C has been chosen for the prototype and encompassing that temperature might provoke its partial melting, second it also gives results that can be, later on, used a a base starting line to modify the thermo-hydraulic computational model and validate is against the thermal outcome of the experimental campaign. The final result of this study will, therefore, be a Test Matrix Map to follow during the two weeks experimental campaign at the Plataforma Solar de Almeria.
The boundary conditions applied to every simulation have already been listed in 2.2.2, while the monitored variables are the same of the ones observed during the Mesh Independence analysis which have also already been listen in 2.2.1. In addition to these, convective and radiative losses are also included into the monitored variables since the simulations now include both aforementioned heat losses. In particular, they are both presented as a % of the total incoming heat flux (see Equation 3.1) and as a net kW/m^2 dispersion (see Equation 3.2.

$$\text{Heat Loss} = \frac{\text{Total Heat Power Lost } [kW]}{\text{Total Incoming Heat Power } [kW]} \cdot 100 \quad [\%] \tag{3.1}$$

$$\text{Heat Loss} = \text{Surface Average of the Total Heat Flux Lost } [kW/m^2] \tag{3.2}$$

Simulation results of the thermo-hydraulic computational model analysis, used as a base for the final Test Matrix, are shown below from Figure 3.1 to Figure 3.16 and resumed, in a more compact solution, from Table 3.1 to Table 3.4.
The final Computed Thermo-hydraulic Test Matrix is shown in Figure 3.27 where its relative uncertainties are also presented by means of siutable error bars. A simple linear dependency has been chosen between the Mesh Independence (see Appendix B), RRs block geometry Independence (see

Appendix C), Convective Heat Losses (see 3.0.1) and Radiative Heat losses (see 3.0.2) errors, which together give the final illustrated bar uncertainty .

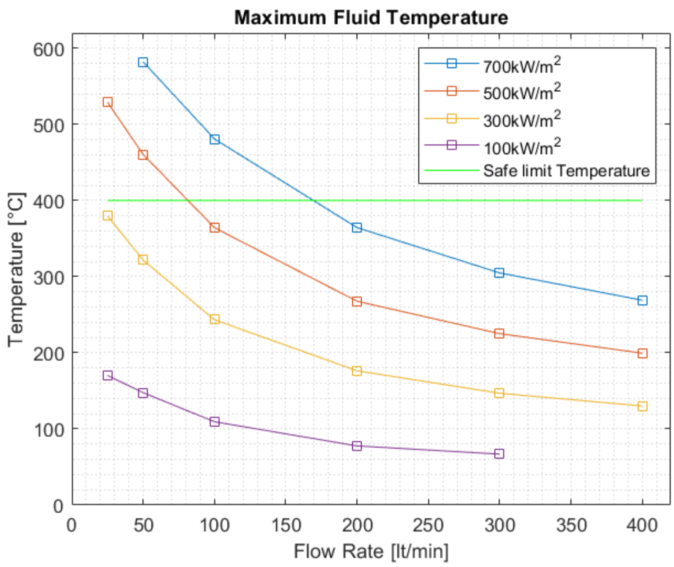

Figure 3.1: Simulation Results, Fluid Maximum Temperature with several flow-rates and heat fluxes.

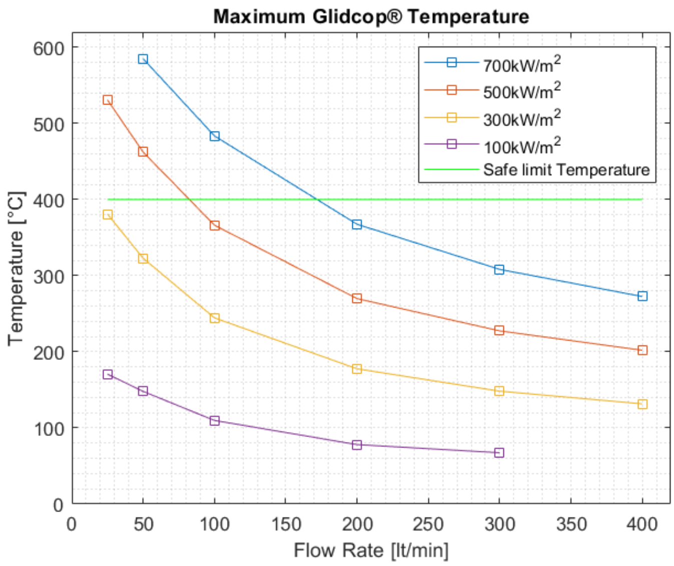

Figure 3.2: Simulation Results, Glidcop® Max. Temperature with several flowrates and heat fluxes.

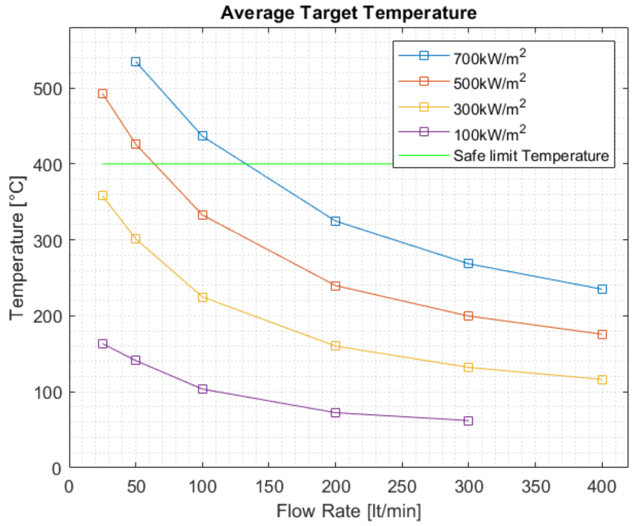

Figure 3.3: Simulation Results, Target Average Temperature with several flow-rates and heat fluxes.

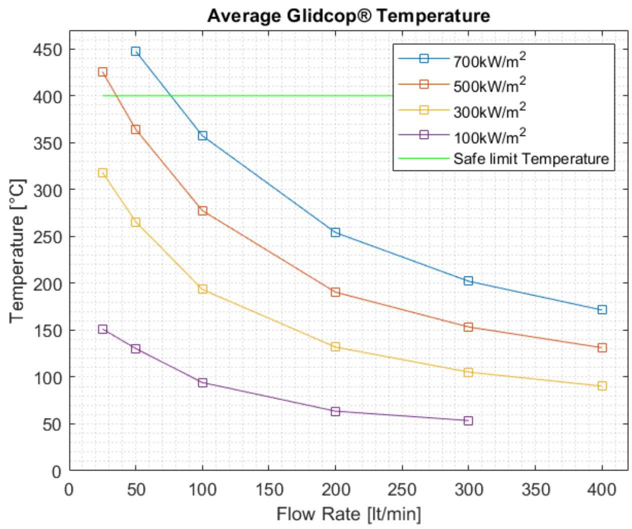

Figure 3.4: Simulation Results, Glidcop® Avg. Temperature with several flow-rates and heat fluxes.

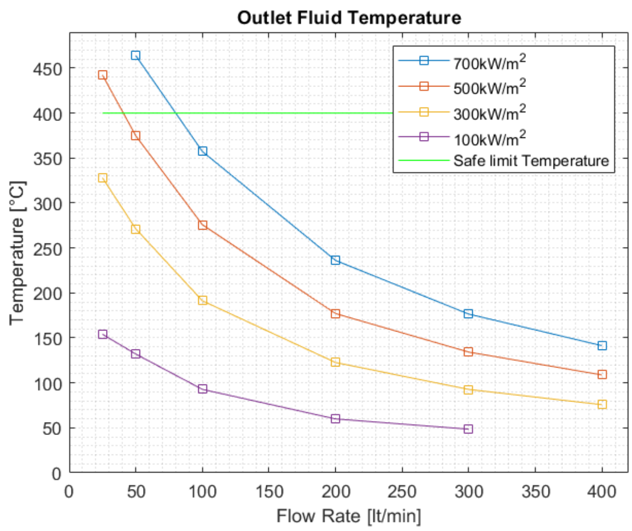

Figure 3.5: Simulation Results, Outlet Fluid Temperature with several flow-rates and heat fluxes.

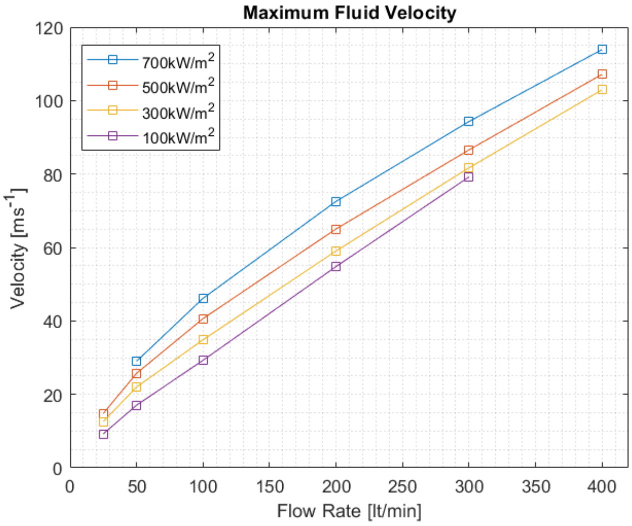

Figure 3.6: Simulation Results, Maximum Fluid Velocity with several flow-rates and heat fluxes.

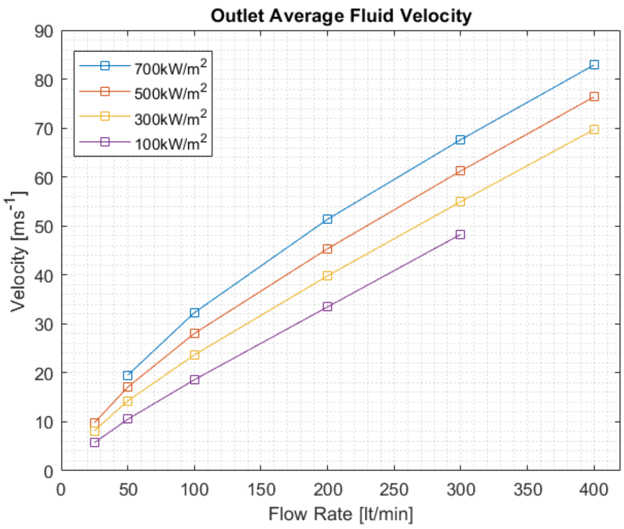

Figure 3.7: Simulation results, Average Outlet Fluid Velocity with several flow-rates and heat fluxes.

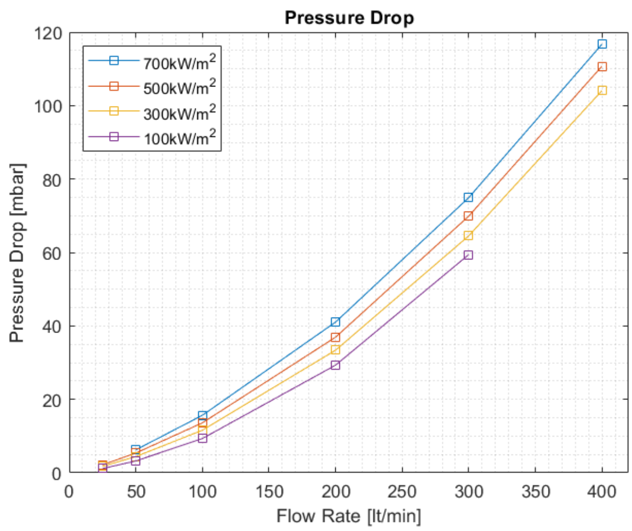

Figure 3.8: Simulation results, Fluid Pressure Drop with several flow-rates and heat fluxes.

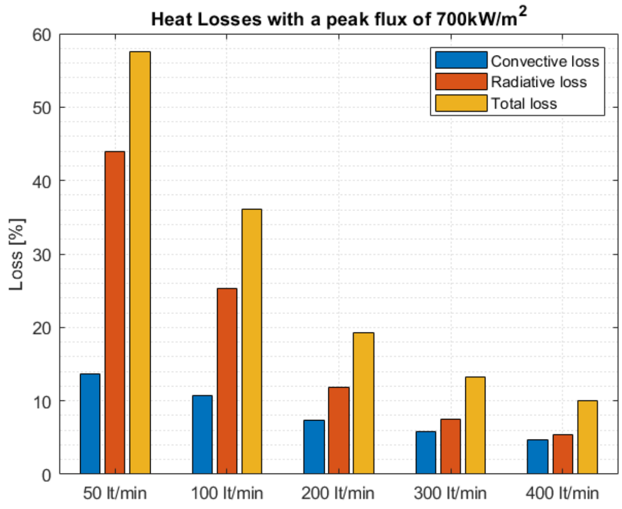

Figure 3.9: Simulation results, Percentage Heat Loss with several flow-rates. Peak flux $700kW/m^2$.

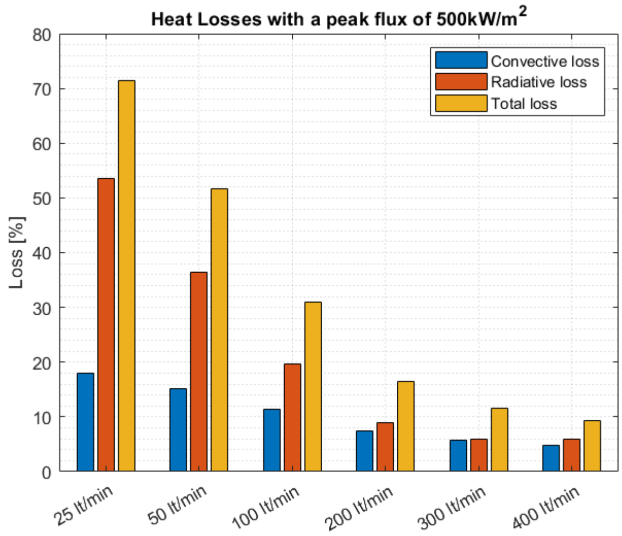

Figure 3.10: Simulation results, Percentage Heat Loss with several flow-rates. Peak flux $500kW/m^2$.

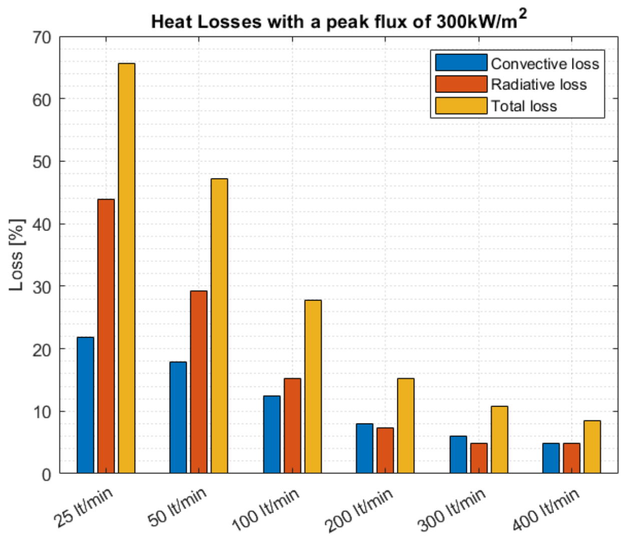

Figure 3.11: Simulation results, Percentage Heat Loss with several flow-rates. Peak flux $300kW/m^2$.

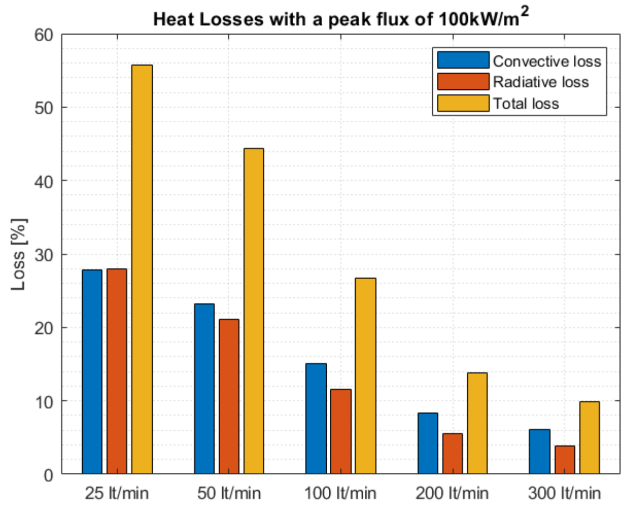

Figure 3.12: Simulation results, Percentage Heat Loss with several flow-rates. Peak flux $100kW/m^2$.

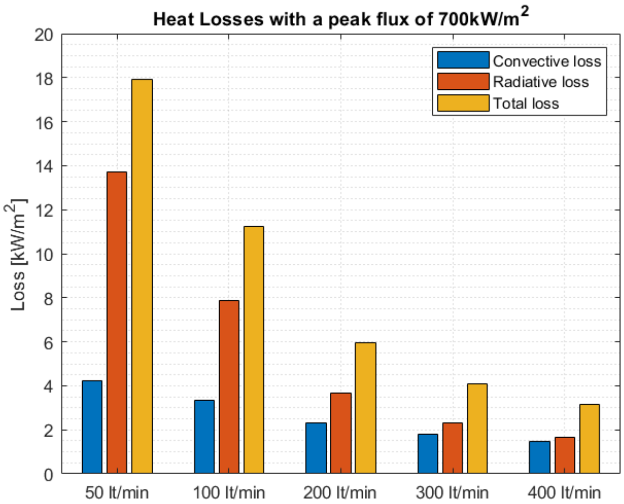

Figure 3.13: Simulation results, Heat Loss in kW/m^2 with several flow-rates. Peak flux $700kW/m^2$.

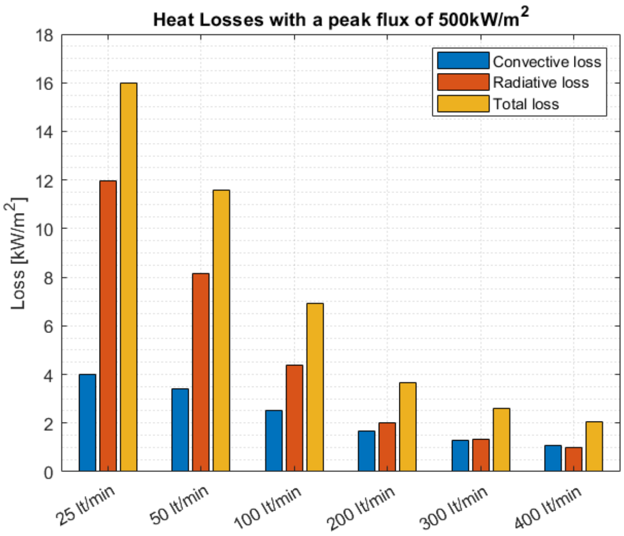

Figure 3.14: Simulation results, Heat Loss in kW/m^2 with several flow-rates. Peak flux $500kW/m^2$.

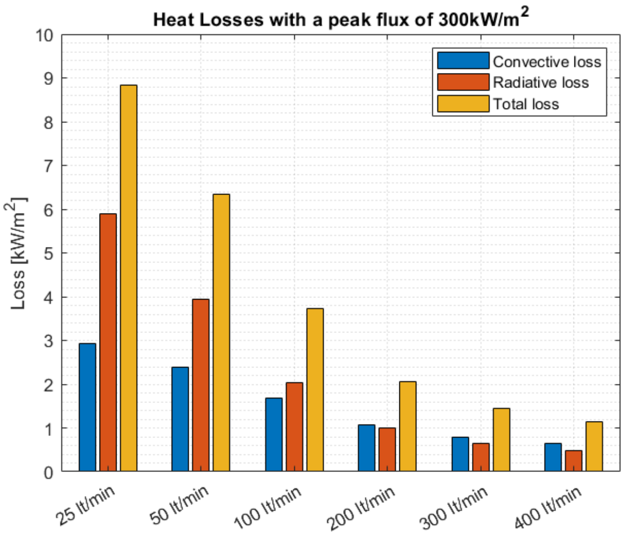

Figure 3.15: Simulation results, Heat Loss in kW/m^2 with several flow-rates. Peak flux $300kW/m^2$.

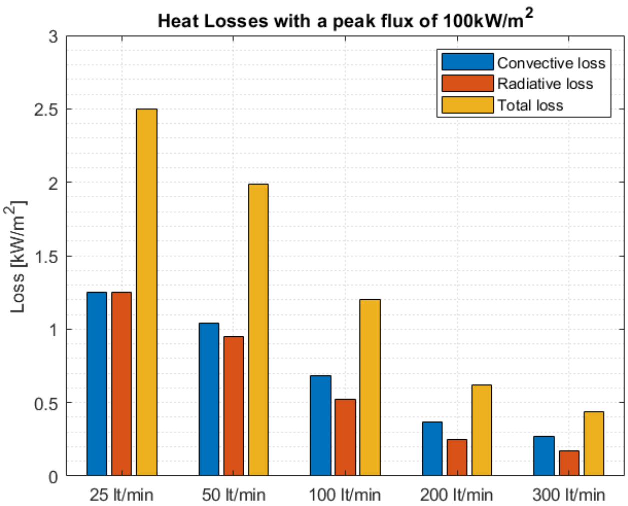

Figure 3.16: Simulation results, Heat Loss in kW/m^2 with several flow-rates. Peak flux $100kW/m^2$.

Table 3.1: Thermo-hydraulic simulation results at different flowrates for a heat flux of 700 kW/m^2.

Simulation Results	**Flowrate [l/min]**				
	50	**100**	**200**	**300**	**400**
Maximum Air Temperature [$°C$]	582.2	480.8	364.4	304.9	269.0
Maximum Glidcop Temperature [$°C$]	584.9	483.5	367.5	308.2	272.6
Average Target Temperature [$°C$]	534.7	436.5	324.7	268.5	235.1
Average Glidcop Temperature [$°C$]	447.4	357.3	254.1	202.2	171.5
Average Outlet Air Temperature [$°C$]	463.9	357.3	236.1	176.5	141.4
Maximum Air Velocity [m/s]	29.01	46.16	72.56	94.30	113.9
Average Outlet Air Velocity [m/s]	19.53	32.20	51.37	67.63	82.87
Pressure Drop [$mbar$]	6.240	15.66	41.04	74.94	116.7
Convective Loss [$\%$]	13.6	10.7	7.42	5.75	4.76
Convective Loss [kW/m^2]	4.24	3.34	2.31	1.79	1.48
Radiative Loss [$\%$]	44.0	25.4	11.8	7.45	5.33
Radiative Loss [kW/m^2]	13.7	7.89	3.67	2.29	1.66
Total Loss [$\%$]	57.6	36.1	19.2	13.2	10.1
Total Loss [kW/m^2]	17.9	11.2	5.98	4.08	3.14

Table 3.2: Thermo-hydraulic simulation results at different flowrates for a heat flux of 500 kW/m^2.

Simulation Results	**Flowrate [l/min]**					
	25	**50**	**100**	**200**	**300**	**400**
Maximum Air Temperature [$°C$]	529.1	460.5	364.3	267.7	225.1	119.5
Maximum Glidcop Temperature [$°C$]	530.8	462.2	366.3	269.8	227.5	202.0
Average Target Temperature [$°C$]	492.8	425.9	332.7	239.8	199.7	175.9
Average Glidcop Temperature [$°C$]	425.7	364.1	277.4	190.5	153.4	131.3
Average Outlet Air Temperature [$°C$]	442.2	374.7	275.9	177.0	134.2	108.8
Maximum Air Velocity [m/s]	14.80	25.73	40.64	65.04	86.57	107.1
Average Outlet Air Velocity [m/s]	9.820	17.10	28.05	45.35	61.23	76.35
Pressure Drop [$mbar$]	2.170	5.380	13.64	36.93	69.90	110.7
Convective Loss [$\%$]	17.9	15.2	11.3	7.43	5.77	4.84
Convective Loss [kW/m^2]	4.01	3.40	2.53	1.66	1.29	1.07
Radiative Loss [$\%$]	53.5	36.5	19.6	8.98	5.90	4.43
Radiative Loss [kW/m^2]	12.0	8.17	4.39	2.01	1.32	0.99
Total Loss [$\%$]	71.4	51.7	30.9	16.4	11.7	9.30
Total Loss [kW/m^2]	16.0	11.6	6.92	3.67	2.61	2.06

Table 3.3: Thermo-hydraulic simulation results at different flowrates for a heat flux of 300 kW/m^2.

Simulation Results	**Flowrate [l/min]**					
	25	**50**	**100**	**200**	**300**	**400**
Maximum Air Temperature [$°C$]	379.8	321.7	243.4	176.3	146.9	130.1
Maximum Glidcop Temperature [$°C$]	380.8	322.8	244.5	177.6	148.3	131.6
Average Target Temperature [$°C$]	357.9	301.2	224.9	160.2	132.1	116.3
Average Glidcop Temperature [$°C$]	318.3	265.5	193.4	131.9	105.3	90.31
Average Outlet Air Temperature [$°C$]	328.0	271.2	191.3	122.6	92.68	75.72
Maximum Air Velocity [m/s]	12.60	22.00	34.86	59.06	81.70	102.9
Average Outlet Air Velocity [m/s]	8.200	14.28	23.67	39.82	54.96	69.68
Pressure Drop [$mbar$]	1.740	4.420	11.59	33.38	64.53	104.1
Convective Loss [%]	21.8	17.9	12.5	7.93	5.94	4.82
Convective Loss [kW/m^2]	2.93	2.40	1.68	1.07	0.80	0.65
Radiative Loss [%]	43.9	29.3	15.2	7.32	4.85	3.66
Radiative Loss [kW/m^2]	5.90	3.94	2.04	0.99	0.65	0.49
Total Loss [%]	65.7	47.2	27.7	15.3	10.8	8.49
Total Loss [kW/m^2]	8.83	6.34	3.72	2.06	1.45	1.14

Table 3.4: Thermo-hydraulic simulation results at different flowrates for a heat flux of 100 kW/m^2.

Simulation Results	**Flowrate [l/min]**				
	25	**50**	**100**	**200**	**300**
Maximum Air Temperature [$°C$]	170.2	147.6	109.4	77.63	66.89
Maximum Glidcop Temperature [$°C$]	170.6	147.9	109.8	78.05	67.37
Average Target Temperature [$°C$]	163.3	141.1	103.6	72.51	62.18
Average Glidcop Temperature [$°C$]	151.2	130.4	94.12	63.59	53.57
Average Outlet Air Temperature [$°C$]	154.0	132.0	92.74	59.88	48.51
Maximum Air Velocity [m/s]	9.240	17.05	29.38	54.80	79.23
Average Outlet Air Velocity [m/s]	5.750	10.53	18.59	33.47	48.29
Pressure Drop [$mbar$]	1.150	3.230	9.330	29.31	59.42
Convective Loss [%]	27.8	23.2	15.1	8.30	6.07
Convective Loss [kW/m^2]	1.25	1.04	0.68	0.37	0.27
Radiative Loss [%]	27.9	21.1	11.6	5.51	3.83
Radiative Loss [kW/m^2]	1.25	0.95	0.52	0.25	0.17
Total Loss [%]	55.7	44.3	26.7	13.8	9.90
Total Loss [kW/m^2]	2.50	1.99	1.20	0.62	0.44

As previously said, the several simulations use different peak heat fluxes and flow-rates. In particular, two cases were not simulated because too distant from a case of interest: peak heat flux of 700 kW/m^2 with a flow-rate of 25 lt/min and peak heat flux of 100 kW/m^2 with a flow-rate of 400 lt/min. The former was not run since the temperatures would have been too much higher than the limit safe temperature of 400 °C (the case with 50 lt/min already has much higher temperatures than the limit), while the latter was not run for the opposite reason, in fact, the temperatures would have been too low (the mock-up would have not heated at all).
The limit safe temperature of 400 °C is only reached by the 500 kW/m^2 and 700 kW/m^2 simulations with a flow-rate of 25-50 lt/min and 50-100 lt/min respectively. The simulation with 300 kW/m^2 peak heat flux and 25 lt/min flow-rate only gets close to the limit but does not reach it.

All temperatures, at any solar peak heat flux, increase when the flow-rate decreases, this seems very reasonable respecting the first principle of thermodynamics. In fact, when the air mass to be heated is lower, its temperature is higher when keeping the incoming heat source fixed.
As shown in Tables 3.1, 3.2, 3.3 and 3.4 the maximum fluid and Glidcop® temperatures are almost the same values, while the average target and outlet air temperatures are also quite close enough between each other. In particular the latter is always bigger than the average Glidcop® temperature.
Temperatures-wise the results seem very promising since the proximity of all these temperatures is probably related to the enhancement of the heat transfer coefficient.
From a fluid-dynamic point of view the simulations show how both the maximum and outlet air velocities increase when the flow-rate increases, as shown in Tables 3.1, 3.2, 3.3 and 3.4. This does make sense since the cross section area of the pipe always remain constant while only the density and the velocity can change when changing the flow-rate. Accordingly a cross check between tables reveals that both velocities also increase, at the same flow-rate, when the solar peak heat flux increases. This is due to the higher temperatures of higher heat flux simulations that make the density of the air lower and therefore the velocities higher.
Velocities-wise the results seem consistent with the physics of the simulations phenomena. In particular, the higher velocity values might seem a bit worrying (the ones around 100 m/s) considering that these values might be related to a compressible flow. However, keeping in mind that the sound speed also does depend on the temperature, increasing with its increase, the Mach number is always below 0.3, being it the limit within which a flow can be considered uncompressible. The Mach number is only being close to 0.3 for flow-rates of 400 lt/min and it is much lower than the limit for lower flow-rates. Additionally, as listed in 2.1.2, the simulations could have dealt with compressible flows anyways thanks to the Ideal Gas model that can also simulate compressible flows.
The high pressure drop is certainly the biggest drawback of the solution of the porous material. The different tables show how much this pressure drop is in every case when changing the peak heat flux and the flow-rate. As known, the pressure drop has a quadratic dependence on the velocity, therefore the higher the velocity the higher the pressure drop. Values are consistent with the results since the pressure drop does increase with the increase of the velocity (both for the increase of the flow-rate and peak heat flux, as already explained above).
Pressure drop-wise results are also promising since the absolute values are quite low and certainly not too high, although higher than what would have been obtained from a regular smooth tube.
Heat loss results are surely the most interesting and important ones. In fact, a low heat loss is sign of an enhanced heat transfer coefficient, while on the other hand a high thermal heat loss is sign of a poor heat transfer coefficient. In general, both convective and radiative thermal heat losses are consistent with the other results, increasing with the increase of the temperature and therefore of the incoming solar heat flux or the decreasing flow-rates. At high temperatures convective loss is lower than the radiative one since the former only has a liner dependence on the first power of the temperature while the latter has a dependence on the forth power of the temperature. This can be seen in Tables 3.1, 3.2, 3.3 and 3.4, in particular the case with 100 kW/m^2 solar peak flux and 25 lt/min flowrate shows an equilibrium where convective losses are equal to radiative ones.
Heat losses appear, from a percentage of the incoming solar heat flux point of view, to be incredibly high and not very promising since they easily reach 50% to 70% of the heat source, mainly because of

the radiative loss. In reality these numbers, presented as a percentage, have to be considered carefully since they are related only to the mock-up and not to the technology itself. Indeed, such values cannot be compared with other technologies as they are since they do not take into account the diversity of the dispersing and receiving areas. As a matter of fact, a more meaningful representation of the heat losses is given in terms of kW/m^2 that can be found in the same Tables 3.1, 3.2, 3.3 and 3.4. In this case in particular, heat dispersions, both convective and radiative, are much lower compared to the incoming solar peak flux (around 3% of it in the worst case) because they now consider the fact that the receiving area is much lower than the dispersing one.
These results presented in this form are now more promising and can also be compared with other technologies and models such as a tubular receiver.

3.0.1 Convective Heat Loss Parametric Analysis

Changing only the solar peak heat flux and the flow-rate, as done in the previous Section 3, might not be sufficient to make a a complete test matrix. In fact, it is very useful to change some other parameters in order to have the biggest as possible amount of data so that, when experimental data on the mock-up are collected, it is easier to compare them with the simulation results and to understand what has to be changed and what has to be kept the same to validate the model. Additionally, this study could also be used to take into account the uncertainty related to the choice of the input parameters when modifying the thermo-hydraulic computational model to validate it against the experimental data.
Among the boundary conditions applied to the air mock-up simulations there is one that describes the convective heat losses, see 2.2.2. The convective heat transfer coefficient was imposed equal to 10 $W/m^2/K$, however the literature states that common convective heat transfer coefficients range from 5 to 20 $W/m^2/K$ when the dispersion happens in still air, depending on its velocity [30].
This section study is to determine what happens to the observed mock-up values when changing the convective heat transfer coefficient, however, since making a small sensitivity analysis for each of the previously calculated simulation requires a lot of time and has a big computational cost, only an example case is chosen, instead, for further investigations. The selected case is the one with a solar peak heat flux of 300 kW/m^2 and a flow-rate of 50 lt/min which is picked because of its conditions that have high chances to happen during the experimental campaign.
Results of the convective heat loss sensitivity analysis are shown below from Figure 3.17 to 3.21 and resumed, in a more compact solution, in Table 3.5.

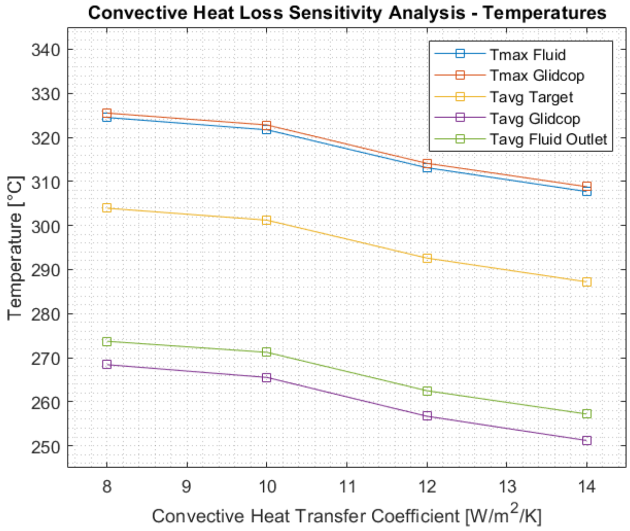

Figure 3.17: Convective Heat Losses Sensitivity Analysis, Temperatures.

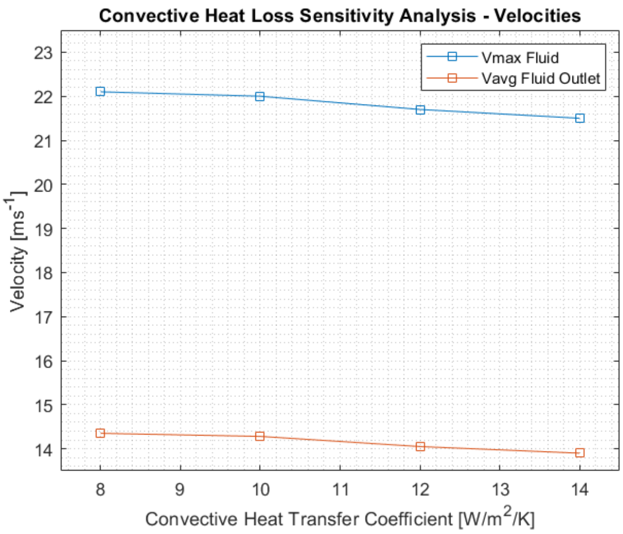

Figure 3.18: Convective Heat Losses Sensitivity Analysis, Velocities.

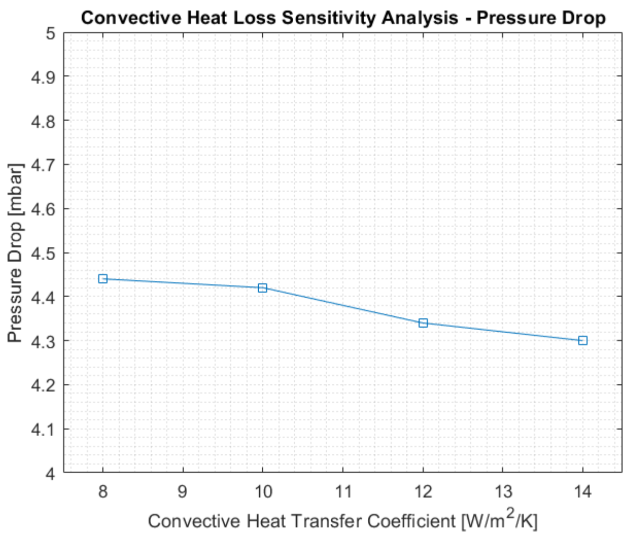

Figure 3.19: Convective Heat Losses Sensitivity Analysis, Pressure Drop.

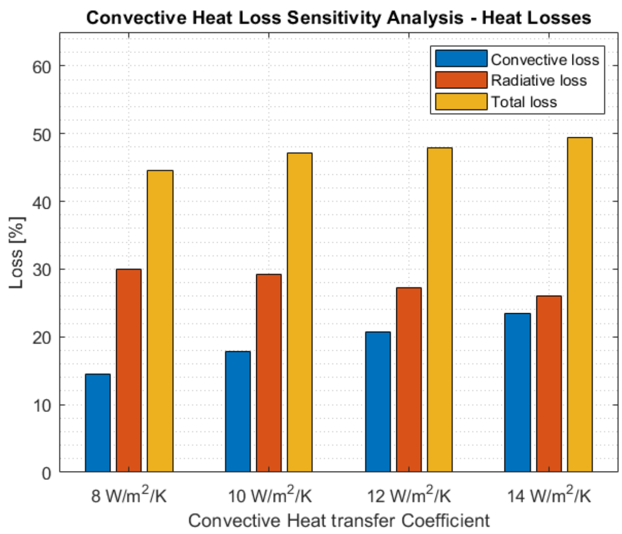

Figure 3.20: Convective Heat Losses Sensitivity Analysis, Heat Losses [%].

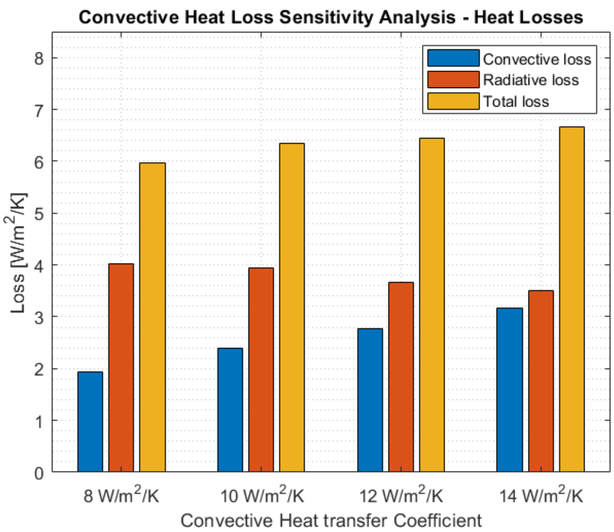

Figure 3.21: Convective Heat Losses Sensitivity Analysis, Heat losses $[kW/m^2]$.

Table 3.5: Convective Heat Losses sensitivity analysis - simulation results.

Simulation Results	**HT Coefficient** [$W/m^2/K$]			
	8	**10**	**12**	**14**
Maximum Air Temperature [$°C$]	324.5	321.7	313.1	307.7
Maximum Glidcop Temperature [$°C$]	325.5	322.8	314.1	308.9
Average Target Temperature [$°C$]	303.9	301.2	292.6	287.2
Average Glidcop Temperature [$°C$]	268.4	265.5	256.7	251.2
Average Outlet Air Temperature [$°C$]	273.7	271.2	262.5	257.2
Maximum Air Velocity [m/s]	22.10	22.00	21.70	21.50
Average Outlet Air Velocity [m/s]	14.35	14.28	14.05	13.90
Pressure Drop [$mbar$]	4.440	4.420	4.340	4.300
Convective Loss [$\%$]	14.5	17.9	20.7	23.5
Convective Loss [kW/m^2]	1.94	2.40	2.78	3.16
Radiative Loss [$\%$]	30.0	29.3	27.2	26.0
Radiative Loss [kW/m^2]	4.03	3.94	3.66	3.50
Total Loss [$\%$]	44.4	47.2	47.9	49.5
Total Loss [kW/m^2]	5.97	6.34	6.44	6.66

Results show that all the observed values change accordingly to the variations of the convective heat transfer coefficient.
Temperatures, which vary consistently, increase when the convective dispersion decreases and decrease when the same dispersion increases, see Table 3.5. In particular every temperature changes of a relatively small amount, from 1% to 5%, with respect to the reference case of $h_{conv} = 10W/m^2/K$.
Velocities change consistently with the dispersion variations as well. Specifically with the increase of the temperature that leads to a decrease of the density, velocities increase to keep the flow-rate constant, see 3.5. Velocities changes are, here, quite small, from <1% to 2% with respect to the reference case of $h_{conv} = 10W/m^2/K$.
Pressure drop is consistent too. It increases when the velocity increases as it has a quadratic dependence on it and decreases vice versa, see Table 3.5. The relative variation here goes from <1% up to 3% with respect to the reference case of $h_{conv} = 10W/m^2/K$.
Heat losses are always one of the most interesting results. They are consistent with the convective heat transfer coefficient variations, increasing with its increase and decreasing with its decrease, see Table 3.5. The convective losses are the ones that demonstrate the biggest variations, relatively speaking from 15% up to 31% with respect to the reference case of $h_{conv} = 10W/m^2/K$, while the radiative losses change too since, as explained, the former losses affect all temperatures on which the latter losses depend as well, in particular the relative variations of the radiative losses go from 2% up to 11% with respect to the reference case of $h_{conv} = 10W/m^2/K$. Interesting is also to see how the equilibrium temperature, a temperature on which convective losses and radiative ones are the same, changes as well. In particular the equilibrium temperature increases with the increase of the convective heat transfer coefficient and decreases vice versa.

3.0.2 Radiative Heat Loss Parametric Analysis

Among the boundary conditions applied to the air mock-up simulations there is one that describes the radiative heat losses, see 2.2.2. The emissivity was imposed equal to 0.9 since the mock-up has a coating treatment, however for the same reasons already presented in 3.0.1 it is wise and useful to make a sensitivity analysis of the radiative losses.
This section study is to determine what happens to the observed mock-up values when changing the emissivity, however, since making a small sensitivity analysis for each of the previously calculated simulation requires a lot of time and has a big computational cost, only an example case is chosen, instead, for further investigations. The selected case is the one with a solar peak heat flux of 300 kW/m^2 and a flow-rate of 50 lt/min which is picked because of its conditions that have high chances to happen during the experimental campaign.
Results of the convective heat loss sensitivity analysis are shown below from Figure 3.22 to Figure 3.26 and resumed, in a more compact solution, from Table 3.6 to Table **??**.

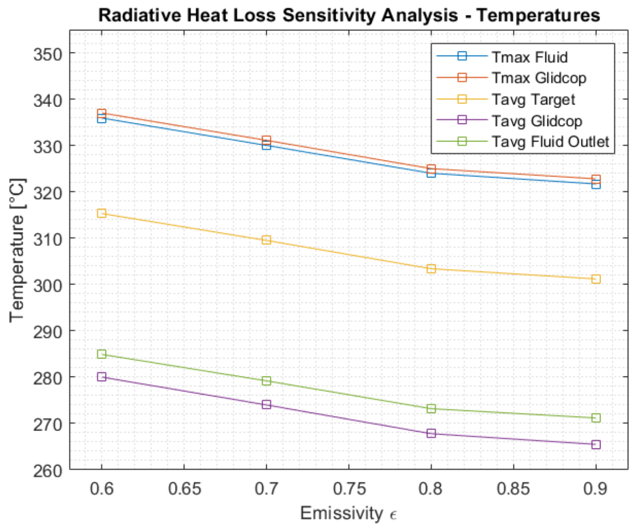

Figure 3.22: Radiative Heat Losses Sensitivity Analysis, Temperatures.

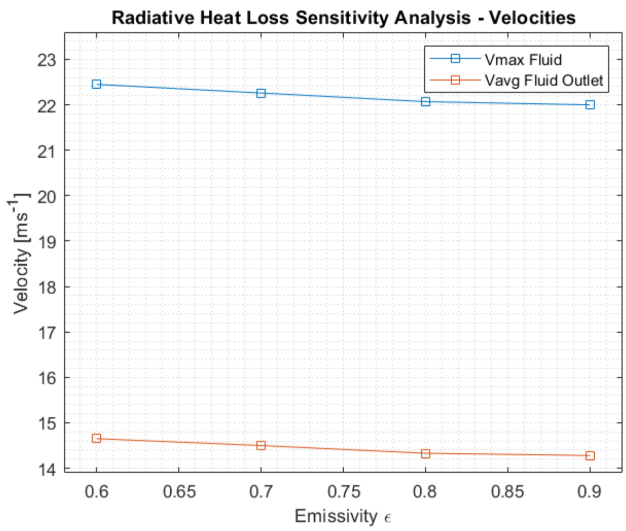

Figure 3.23: Radiative Heat Losses Sensitivity Analysis, Velocities.

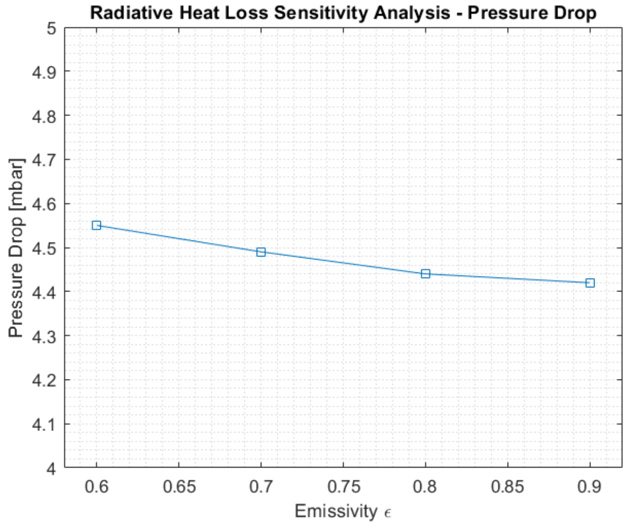

Figure 3.24: Radiative Heat Losses Sensitivity Analysis, Pressure Drop.

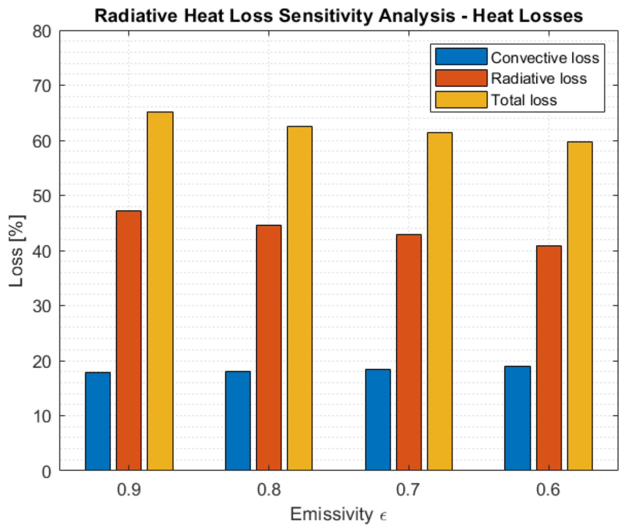

Figure 3.25: Radiative Heat Losses Sensitivity Analysis, Heat Losses [%].

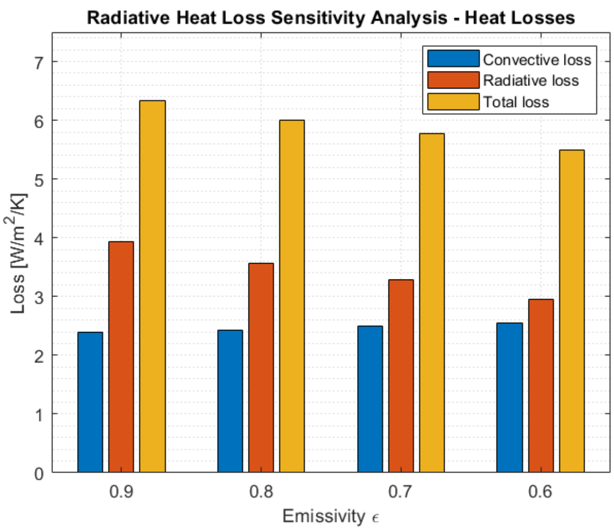

Figure 3.26: Radiative Heat Losses Sensitivity Analysis, Heat Losses [kW/m^2].

Table 3.6: Radiative Heat Losses sensitivity analysis - simulation results.

Simulation Results	Emissivity $\epsilon[-]$			
	0.6	**0.7**	**0.8**	**0.9**
Maximum Air Temperature $[°C]$	335.9	330.0	324.0	321.7
Maximum Glidcop Temperature $[°C]$	337.0	331.1	325.0	322.8
Average Target Temperature $[°C]$	315.3	309.5	303.4	301.2
Average Glidcop Temperature $[°C]$	280.0	274.0	267.8	265.5
Average Outlet Air Temperature $[°C]$	284.9	279.2	273.2	271.2
Maximum Air Velocity $[m/s]$	22.45	22.26	22.07	22.00
Average Outlet Air Velocity $[m/s]$	14.65	14.50	14.33	14.28
Pressure Drop $[mbar]$	4.550	4.490	4.440	4.420
Convective Loss $[\%]$	18.9	18.5	18.0	17.9
Convective Loss $[kW/m^2]$	2.55	2.49	2.43	2.40
Radiative Loss $[\%]$	22.0	24.4	26.5	29.3
Radiative Loss $[kW/m^2]$	2.95	3.28	3.57	3.94
Total Loss $[\%]$	40.9	42.9	44.6	47.2
Total Loss $[kW/m^2]$	5.50	5.77	6.00	6.34

Results show that all the observed values change accordingly to the variations of the convective heat transfer coefficient.

Temperatures, which vary consistently, increase when the radiative dispersion decreases and decrease when the same dispersion increases, see Tables 3.6. In particular every temperature changes of a relatively small amount, from <1% up to 5%, with respect to the reference case of $\epsilon = 0.9$.

Velocities change consistently with the dispersion variations as well. Specifically with the increase of the temperature that leads to a decrease of the density, velocities increase to keep the flow-rate constant, see Table 3.6. Velocities changes are, here, quite small, from <1% to 2% with respect to the reference case of $\epsilon = 0.9$.

Pressure drop is consistent too. It increases when the velocity increases as it has a quadratic dependence on it and decreases vice versa, see Table 3.6. The relative variation here goes from <1% up to 2.5% with respect to the reference case of $\epsilon = 0.9$.

Heat losses are always one of the most interesting results. They are consistent with the emissivity variations, increasing with its increase and decreasing with its decrease, see Table 3.6. The radiative losses are the ones that demonstrate the biggest variations, relatively speaking from 9.5% up to 25% with respect to the reference case of $\epsilon = 0.9$, while the convective losses change too since, as explained, the former losses affect all temperatures on which the latter losses depend as well, in particular the relative variation of the convective losses goes from <1% up to 5.5% with respect to the reference case of $\epsilon = 0.9$. Interesting is also to see how the equilibrium temperature, a temperature on which convective losses and radiative ones are the same, changes as well. In particular the equilibrium temperature increases with the decrease of the emissivity and decreases vice versa.

As previously anticipeted in 3, hereby in Figure 3.27 is shown the final computed Test Matrix together with the uncertainty related to each estimation.

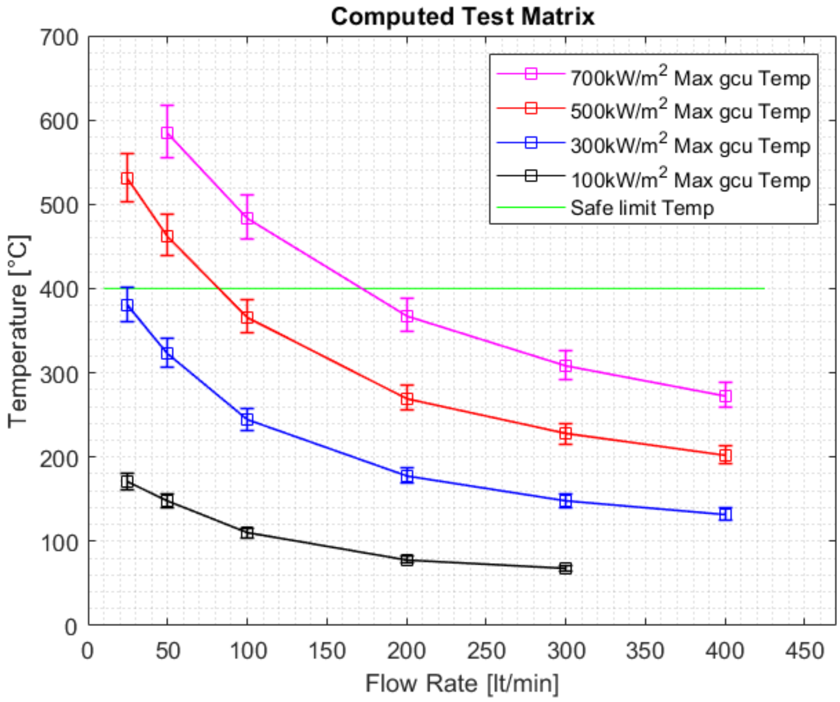

Figure 3.27: Computed Test Matrix with error bars.

3.1 Pure hydraulic CFD Model Results

The pure hydraulic model simulations are entirely devoted to the estimation of the pressure drop across the mock-up. Several flowrates are used and pressure drop checked in order to extrapolate the hydraulic characteristic of the mock-up. The pressure drop calculated by the pure hydraulic CFD model is estimated by means of a difference between the mock-up inlet high pressure and its outlet low pressure, both pressures are expressed as an average over the aforementioned inlet and outlet areas, respectively.

The results of the pure hydraulic simulation, concerning the mock-up pressure drop, is shown in Figure 3.28 and resumed, in a more compact solution, in Table 3.7.

The simulated results can, indeed, be related between each other with a trend curve which is also shown in Figure 3.28. Specifically, the equation of that trend curve, which is reported below (see Equation 3.3), follows a quadratic behaviour which corresponds to the physics of the problem.

$$Y = 0.1357 \cdot X^2 \quad R^2 = 91.5\% \tag{3.3}$$

The fit curve (Equation 3.3) has a error number associated to it which is called coefficient of deviation R^2, this value which is often expressed as a percentage, gives an idea of how much the computed CFD points are represented by the trend curve. An R^2 value of 100% would mean a perfect fit between the trend curve and the data points, while a value of 0% would mean that the fitting points are not justified at all by the trend curve. The higher the value of R^2 the better.

Hereby follows the adopted mathematical definition of the coefficient of deviation R^2:

$$R^2 = 1 - \frac{(E_{tot})^2}{(E_{mean,tot})^2} \tag{3.4}$$

In Equation 3.4 the R^2 term is not expressed in terms of percentage. The E_{tot} is the total error distance, that is the sum of the total distance between the data points and the trend curve values. The $E_{mean,tot}$ is instead the total mean error distance, that is the sum of the total distance between the data points and their mean value. Since the coefficient of deviation is calculated using data points that have an error bar (3.67% in this case), said uncertainty has to be considered and therefore is subtracted twice from the R^2 value (the double subtraction is due to the $\pm$ nature of the uncertainty).
In the Figure 3.28 both the error bar of the computed CFD values due to the grid choice and RRs block independence (see 2.2.1 and C) and the error related to the R coefficient of the trend curve are shown with an error or 3.67% and 8.5% respectively. The grid and RRs block 3.67% error is also shown in Table 3.7 in form of an absolute pressure error.

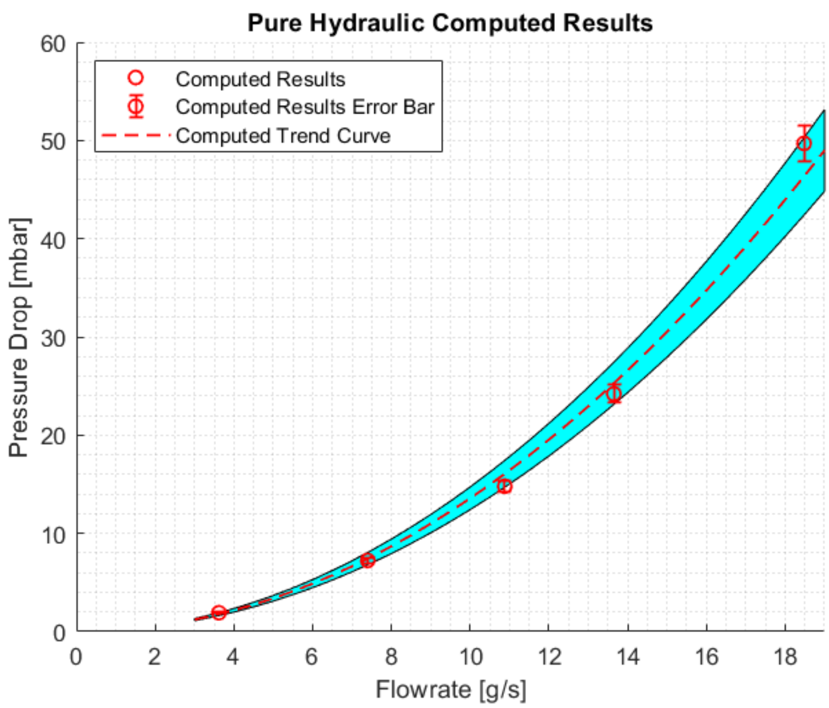

Figure 3.28: Pure Hydraulic Simulation Results: the R^2 Trend Curve uncertainty error area is represented above in cyan.

Table 3.7: Pure Hydraulic Simulated Results

Flow rate		**Outlet Velocity**	**Max. Velocity**	**Pressure Drop**	**Pdrop Error**
168 $[l/min]$	3.62 $[g/s]$	2.30 $[m/s]$	4.19 $[m/s]$	1.98 $[mbar]$	$\pm$ 0.07 $[mbar]$
344 $[l/min]$	7.40 $[g/s]$	4.51 $[m/s]$	8.31 $[m/s]$	7.24 $[mbar]$	$\pm$ 0.27 $[mbar]$
506 $[l/min]$	10.9 $[g/s]$	6.35 $[m/s]$	11.7 $[m/s]$	14.8 $[mbar]$	$\pm$ 0.54 $[mbar]$
635 $[l/min]$	13.7 $[g/s]$	8.48 $[m/s]$	15.7 $[m/s]$	24.2 $[mbar]$	$\pm$ 0.89 $[mbar]$
860 $[l/min]$	14.5 $[g/s]$	12.6 $[m/s]$	23.1 $[m/s]$	49.7 $[mbar]$	$\pm$ 1.82 $[mbar]$

The results of this analysis will be, at the end of the experimental campaign, be compared with the experimental results collected at the PSA. A hydraulic validation of the model can be done if a match between experimental and simulated results is found. Additionally, as a cross check, the hydraulic characteristic of the mock-up using air as working fluid could be also compared with the characteristic of the sample when water was used as cooling fluid.

4. Experimental Campaign

4.1 Plataforma Solar de Almeria

The Plataforma Solar de Almeria (PSA) belongs to the Department of Energy of the Centro de Investigaciones Energéticas, Medioambientales y Tecnologicas (CIEMAT), a public research organization under the Spanish Ministry of Economy and Competitiveness. The PSA is without doubt the largest research, development and test centre in the world, with its more than 100 hectars [31], dedicated to the technologies of concentrated solar radiation. This fact makes Spain and, in particular, the PSA, the centre of excellence for visitors and researchers related with these systems from all around the world [32].
An aerial view of the PSA is shown in Figure 4.1 below.

Figure 4.1: Aerial view of the Plataforma Solar de Almeria.

The PSA took root in the late 70' with the construction in the desert of Tabernas (Almeria) of two projects (i.e., SSPS and CESA-I promoted by the Internation Energy Agency and by the spanish government, respectively) to demonstrate the technical feasibility of producing electricity by concentrating solar thermal systems. These systems are considered as a first generation solar thermal power plants. Evaluation of both project was completed in 1984. Additionally, from 1985 to 1987 the CESA-I project served as a test bed for an ambitious program called GAST, a spanish-german project aimed at the design, construction and testing of components for a second generation air-cooled plant.

During the same period, the Internation Energy Agency (IEA) transferred to SPain the ownership of all the SSPS project assets and Germanu signed a bilateral cooperation agreement for the joint use of the PSA as a centre of concentrating solar thermal technology research, developmente and demonstration. The two centres which accepted that agreement were CIEMAT for Spain and DLR (German Aerospace Agency) for Germany. Nevertheless, from January 1999 the scientific management of the PSA is now wholly responsibility of CIEMAT as owener of the PSA facilities and the collaboration with DLR is now set in the context of specific projects only. [32]
Research activity at the Plataforma Solar de Almeria has been structured around three RD Units:

- Solar Concentrating Systems - This unit is devoted to promote and contribute to the development of solar concentrating systems, both for power generation and for industrial processes heat applications requiring solar concentration, whether for medium/high concentrations or high photon fluxes.
- Solar Desalination - It has the objective of new scientific and technological knowledge development in the field of brackish and seawater solar desalination.
- Solar Treatment of Water - Exploring the photochemical possibolities of solar energy, especially regarding its potential for water detoxification and disinfection.

Maintainance, operation and technical services, which are grouped together in the PSA Managment Unit, are supporting the RD Units mentioned above [32].
Today the PSA is formally constituted by 28 large experimental facilities and 10 laboratories. The facilities are those listed below [33]:

1. Installations based on Cylinder-Parabolic technology
    - 1.8 MW_{th} DISS test loop, an excellent experimental system for the investigation of two-phase flow and the direct generation of steam for electricity production. It consists of two rows of parabolic trough collectors of 550 m in length and 2750 m^2 and 115 m in length 1088 m^2 of solar gain area, respectively;
    - The HTF test loop, formed by 3 parabolic cylinder collectors of 75 m in length and equipped with a complete oil circuit that allows the evaluation and qualification of new components under real operating conditions;
    - PROMETEO. Installation based on the IBERTROUGH prototype for the testing of new components and thermal transfer fluids for large parabolic trough collectors;
    - PTTL. Installation that allows the testing in real conditions of new complete prototypes (loops) of parabolic trough collectors up to 180 m long;
    - NEP. Field consisting of 8 Polytrough 1200 parabolic trough collectors (1.2 m opening and 125 kW_{th}) for polygeneration applications up to 220 °C;
    - ILF. Parabolic trough collectors system called "Test Loop for Innovative Fluids", for tests up to 400 °C and 100 bar;
    - TCP-100, a field formed by 3 loops of parabolic trough collectors of 2.3 MWt with a thermocline tank for thermal storage (115 m^3);

2. Other facilities related to parabolic trough technology

   - KONTAS. Rotatory test bench for parabolic cylinder collector components up to 20 m long;
   - REPA. System for conducting accelerated life cycle tests (rotation and expansion) of mobile elements in parabolic trough collectors;

3. Facilities based on Fresnel technology

   - FRESDEMO loop, consisting of 25 lines of mirrors with a total surface area of approximately 1400 m^2;

4. Thermal Storage Facilities

   - MOSA installation. Formed by a molten salt storage system (40 tons), heating and dissipation of the thermal energy of salts (290-380°C) system, thermal oil system and interconnection systems;

5. Central receiver installations (tower technology)

   - CESA-1 installation of 6 MW_{th}, 80 m high tower and 4 trial platforms;
   - Installation SSPS-CRS of 2.5 MW_{th}, with a 43 m. high tower and 3 test platforms;

6. Solar Furnaces

   - SF-60, of 60 kW_{th} and horizontal axis, associated with a 120 m^2 heliostat;
   - SF-40, of 40 kW_{th} and horizontal axis, associated with a 100 m^2 heliostat;
   - SF-5, of 5 kW_{th} and vertical axis, associated with a 25 m^2 heliostat;

7. Parabolic Discs

   - EURODISH, composed of 2 large diameter parabolic discs with an external combustion engine type Stirling located in its focal area;
   - Aging Test Bed. Installation consisting of 4 parabolic units (3 DISTAL-II type with 50 kW_{th} and 1 DISTAL-I type with 40 kW_{th}), where the original Stirling engines have been replaced by different platforms for the performance of aging tests at high concentration of materials or prototypes of small-scale solar receivers;

8. Solar Desalination

   - MED. Multi-effect plant of 14 stages (3 m^3/h of nominal production) coupled to a field of static solar collectors (606 m^2), a thermal storage system in water (40 m^3), a double effect heat pump ($LiBr - H_2O$) and a gas boiler;
   - CSP + D. Integration of the MED plant in solar power cycles. The system has 2 steam generators (250 and 500 kW_{tj}) for the simulation of different power thermodynamic cycles (up to 400°C) using the 14-stage MED plant as the cooling element of the cycle;

- MDTF. Test bench of different systems of distillation by membranes at pilot scale;

9. Water Treatment

  - DETOX. Complex installation for solar detoxification applications, composed of a loop of parabolic trough collectors with tracking on two axes and three loops of CPC photoreactors type, for the realization of different types of tests;
  - DISINF. Installation consisting of several pilot plants of CPC geometry and anodized aluminum and non-solar plants for experimental solar water disinfection applications, complemented by an experimental greenhouse designed as a 30 m^2 cultivation chamber;
  - HYWATOX. Experimental plant for the photocatalytic production of hydrogen associated with a solar CPC collector;
  - WETOX Experimental system for supercritical wet oxidation (up to 300°C and 200 bar);

10. Meteorological Facilities

  - METAS. Meteorological station integrated in the Baseline Surface Radiation Network (BSRN);

11. Energy Efficiency Installations

  - Energy Testing of Building Components Laboratory (LECE), consisting of a set of test cells and experimental buildings for the monitoring of innovations in the energy efficiency of buildings;

4.2 Solar Furnace

Solar furnaces can be defined as optical systems that concentrate solar radiation in a small area called focus where high temperatures and thermal fluxes can be reached. They can read concentrations of over 10000 suns, the highest energy levels achievable in a solar concentrating system so far. Their main field of application are testing materials, either at room conditions, controlled atmosphere or vacuum, and solar chemistry experiments using chemical reactors associated with receivers.
Essentially a solar furnace consists of [34]:

- A continuously solar-tracking;
- Flat heliostat;
- A parabolic-dish concentrator;
- An attenuator or shutter;
- A test-best located under the focus point;

The flat heliostat reflects the incoming solar beams on the parabolic-dish concentrator, which in turn reflects them on its focus (the test area). The amount of incident light is regulated by the attenuator located between the concentrator and the heliostat. Under the focus, a test table movable in three directions (East-West, North-South and Up-Down) places the test samples in the focus with precision [34].
An example scheme of a Solar Furnace is shown in Figure 4.2.
The experimental campaign to run the field tests on the air RRs mock-up is carried out at the Solar Furnace 60 (SF60) Facility.

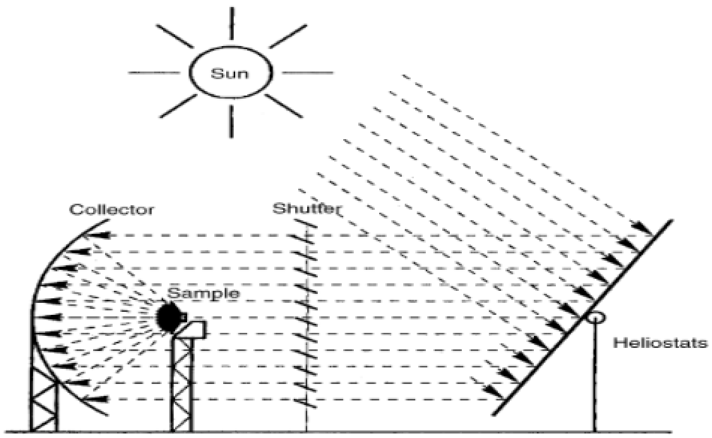

Figure 4.2: Solar Furnace working principle scheme [35].

4.2.1 SF-60 Facility

The SF60 constists in a 120 m^2 flat heliostat that reflects the solar beam onto a 100 m^2 parabolic concentrator which is turn concentrates the incoming rays on the focus of the parabola, where the tested specimens are placed. The incoming light is regulated by a louvered shutter places between the heliostat and the concentrator. Finally a test table movable on three axes is used to place the specimens in the focus [34].
In this furnace, the heliostat collects the solar radiation and redirects it to the concentrator. The heliostat's reflective surface is made up of flat, non concentrating facets, which reflect the sun's rays horizontally and parallel to the optical axis of the parabolic-dish concentrator, continuously tracking the sun [34].
The only heliostat associated with the SF-60 is made of 120 flat facets, with 1 m^2 reflecting surface each. These facets have been designed, manufactured, assembled and aligned by PSA technicians. Every facet is composed of a 1 m^2 reflecting surface and 3 mm thick Rioglass flat mirror silvered on its back [34].
The SF-60 heliostat is shown in Figure 4.3.
The shutter or attenuator consists of a set of horizontal louvers which turn on their axis to control the amount of sunlight incident on the concentrator. The total energy in the focus is proportional to the radiation that goes through the shutter [34].
The SF-60 shutter is shown in Figure 4.4.

Figure 4.3: View of the new heliostat [34].

Figure 4.4: View of the shutters and heliostat [34].

The parabolic concentrator is the main feature of this solar furnace. It is made of spherically curved facets distributed along five radii with different curvatures depending on their distance from the focus. It concentrates the incident sunlight from the heliostat, multiplying the radiant energy in the focus [34].
The SF-60 parabolic concentrator is shown in Figure 4.5.
The test table is a mobile support for the test pieces or prototypes to be tested that is located under the focus of the concentrator. It moves on three axes perpendicular to each other and locate the test samples with great precision in the focal area [34].
The SF-60 mobile test table is shown in Figure 4.6.

Figure 4.5: View of the Parabolic Concentrator.

Figure 4.6: View of the moving Test Table.

The combination of all the compenents described leads to the flux density distribution in the focus which is what characterizes a solar furnace. This distribution usually has a Gaussian geometry and is characterized by a CCD camera hooked up to an image processor and a lambertian target. The characteristics of the focus with 100% aperture and solar radiation of 1 kW/m^2 are:

- concentrated peak flux = 3000 kW/m^2;

- total power = 69 kW;
- focal diameter = 26 cm;

4.3 Test Circuit Setup

The Experimental Campaign was carried out from September 7^{th} to September 20^{th} 2019. The first day of the two testing weeks was entirely dedicated on the assembling of the mock-up into the hydraulic testing circuit and on its setup.
The steps followed to set everything up are resumed and documented below:

- Welding of the RRs Mock-up:

In order to connect the mock-up to the hydraulic testing circuit a weld was required since both the inlet and outlet tubes of the RRs mock-up had no thread on their extremities.
An additional piece of pipe having a thread on one side was added on both extremities of the mock-up. Particular attention was spent on choosing additional pipes of a diameter matching the one of the mock-up tubes.
In Figure 4.7 is shown the mock-up before and after the welding to the additional connection pipes (on the left side), as well as a view of the inside of the two connected pipes as a check of the quality of the welding (on the right size).
Another option, in order to connect the mock-up to the test circuit, was to make a thread directly into the mock-up extremities but this choice was discarded since it would have lead to an irreversible modification of the mock-up (the two welded connection pipes can be cut right after the experimental campaign) and to a bigger pressure drop caused by the different diameter that the connection pipes would have had in that case.

Figure 4.7: Particulars of the RRs Mock-up welding to the connection pipes.

- Positioning of the two additional Thermocouples:

The RRs mock-up has a total of 11 thermocouples (TCs) of the K-type, see 4.4.1 for further information, welded inside of its structure. Specifically, it has one TC positioned at the inlet, before the RRs section, one TC located at the outlet into the mixing chamber after the RRs section, as well as the others 9 TCs which are inserted into the RRs block. The readings of these last nine thermocouples contain some uncertainty as it is not known exactly if each thermocouple only touches the copper RRs, the air or both.
Figure 4.8 shows a general sketch of the mock-up and its TCs. In particular all the central thermocouples, the ones below the 2 mm thick target area, are located at the same depth with only a gap positioning uncertainty of 0.6 mm as it shown in Figure 4.9 and Figure 4.10.
Unfortunately, after the previous experimental campaign mentioned in 1.6.1, two TCs broke: TC#4 and TC#11. While the RRs block still has other 8 TCs that can monitor its temperature, the inlet area has none, therefore some additional thermocouples were very much needed to measure the missing information.
The PSA staff provided two additional thermocouples of the K-type, one to be placed at the inlet and one to be located at the outlet of the mock-up. In particular the latter additional thermocouple is redundant but, apart from being always a good choice to have more measurements and less, it would be useful to have another value that could be compared with the other outlet TC of the mock-up as a quality cross check.
To provide better measurements the two aforementioned additional thermocouples are inserted after a temperature stibilizing chamber (see Figure 4.11) located both before and after the mock-up inlet and outlet, respectively. This will help to mix the air and therefore collect a more realistic bulk temperature of the air.
The distance between the two additional TCs and the original mock-up outlet and inlet TCs is of about 13 cm. This distance is, however, not shown in the following TCs logic scheme in Figure 4.12 where all TCs are numbered.

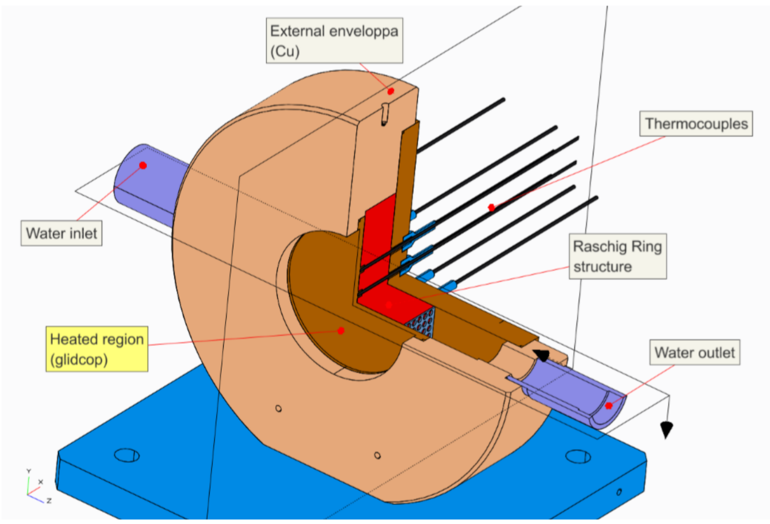

Figure 4.8: CAD view of the Mock-up Thermocouples from previous experimental campaign in 2016.

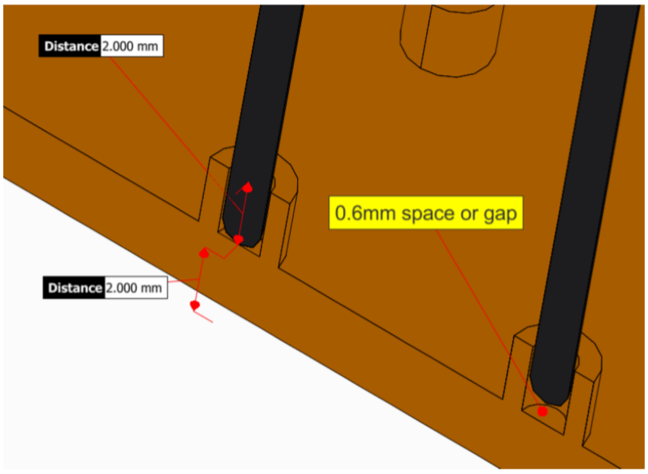

Figure 4.9: TCs Detail and 0.6 mm gap uncertainty.

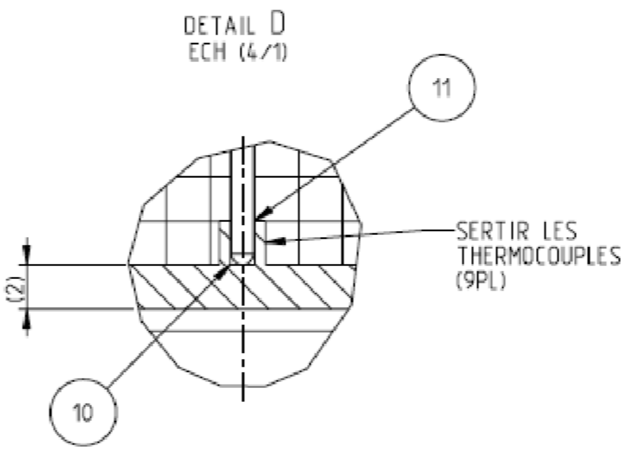

Figure 4.10: CAD Detail of TCs below the target.

Figure 4.11: Temperature Stabilizing Chamber located at the inlet and outlet of the RRs Mock-up.

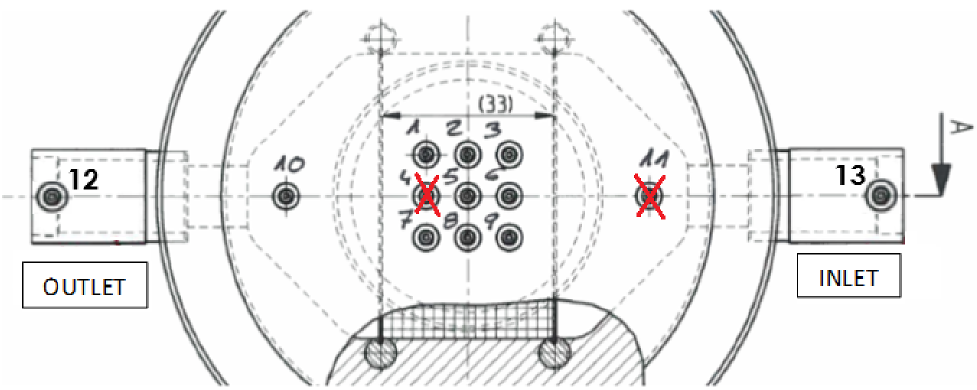

Figure 4.12: Scheme illustrating the position of all the RRs mock-up thermocouples.

- Positioning of an Alumina Shield:

The SF-60 parabolic concentrator has a focus of around 25 cm, while the total external diameter of the target of the RRs mock-up is only 4.5 cm. Since the Raschig Rings block is located only below the target area of the sample, as it was originally manufactured for nuclear application (see Section 1.6), this difference between the two diameters is indeed a problem. The mock-up is not designed to receive a heat flux on surfaces which are not the target area, in fact the temperature would rise faster and higher in those surfaces since the enhancement of the heat transfer coefficient would not be great there.

A solution to this practical inconvenient is to place an Alumina sheet to act as a shield for the sample and block part of the concentrated flux reflected by the parabolic concentrator. The hole into the Alumina sheet was made smaller than the target diameter, 38 mm and 45 mm respectively, as otherwise part of the solar rays coming from the extremities of the concentrator, the ones with a higher solid angle with respect to the target area, would have reached the circular crown of the mock-up instead.

Another possible solution was to make the hole of the the Alumina sheet of the same size of the target area but in this case the protective shield should have, then, been placed completely attached to the mock-up leading to an alteration of both convective and radiative heat losses. Therefore this option was discarded as the former was considered to be the better one.

Finally, the distance between the Alumina shield and the sample is of around 1.5 cm which should be sufficient to not affect too much the thermal losses.

A view of the mounted mock-up before and after the placement of the Alumina shield is shown in Figure 4.13 and Figure 4.15, respectively. Figure 4.14 shows instead a close view of the distance left between the mock-up and the aforementioned Alumina sheet.

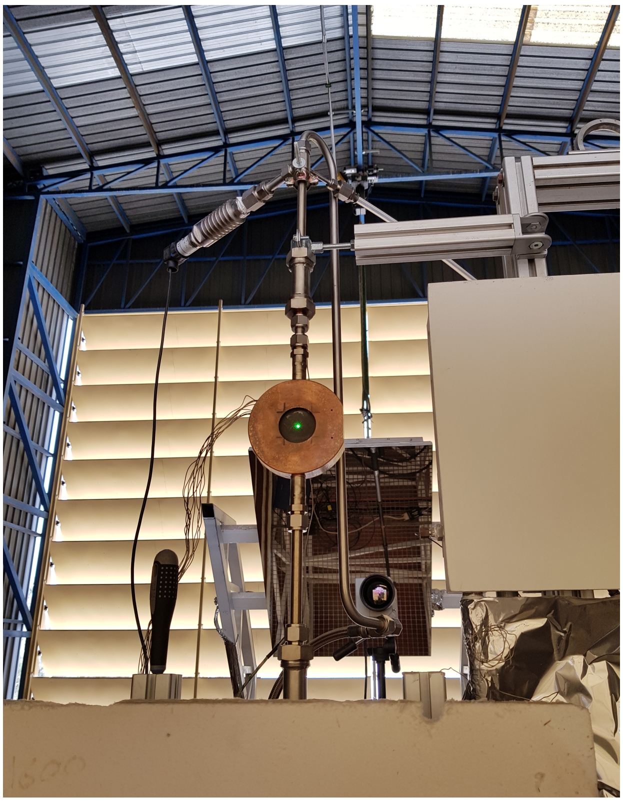

Figure 4.13: Mock-up without Alumina Shield.

Figure 4.14: Mock-up and Alumina Shield distance.

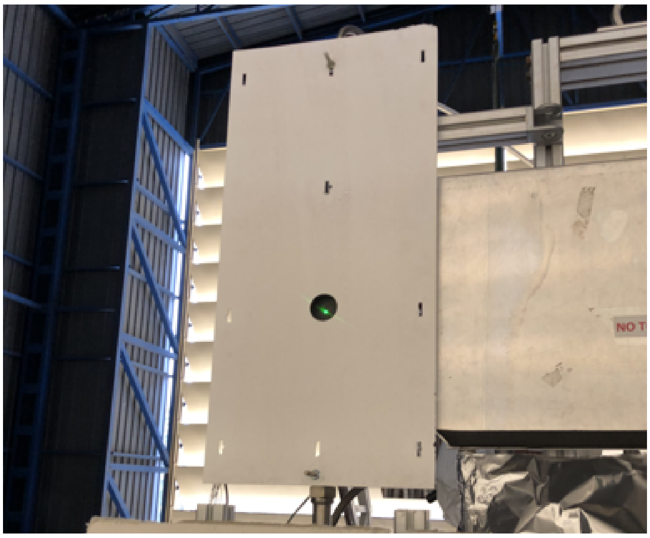

Figure 4.15: Mock-up with the Alumina Shield.

4.3.1 Final Test Circuit Description

The final test circuit was mounted by the end of the first day of the experimental campaign at the PSA. A scheme of the final circuit is shown below in Figure 4.16.
The testing circuit includes:

- A compressor, needed to increase the air pressure of the entire circuit to the value of 10 bar. The circuit is of the open type as it sucks air from the ambient;
- A pump, needed to pump the water into the secondary circuit. The pumped water goes into the cooler and into some pipes placed underneath the white table where the radiometer is located in order to refrigerate it;
- A radiometer, needed to measure the amplitude of the solar peak flux. This measurement is taken every time before each test;
- A cooler, needed to cool down the hot air coming from the primary mock-up test circuit. The cooling working fluid is the water pumped by the pump from the secondary circuit;
- A flow-meter, needed in order to check that the air flow-rate during each test remains constant and close enough to the target value;
- A Differential Pressure Drop Sensor, needed to measure and estimate the pressure drop across the RRs Mock-up;
- Control valves, many of these are needed to adjust and control the flow of both air and water into the different pipes;
- Alumina Shield, already described in 4.3;
- RRs Mock-up, largely described in 1.7;

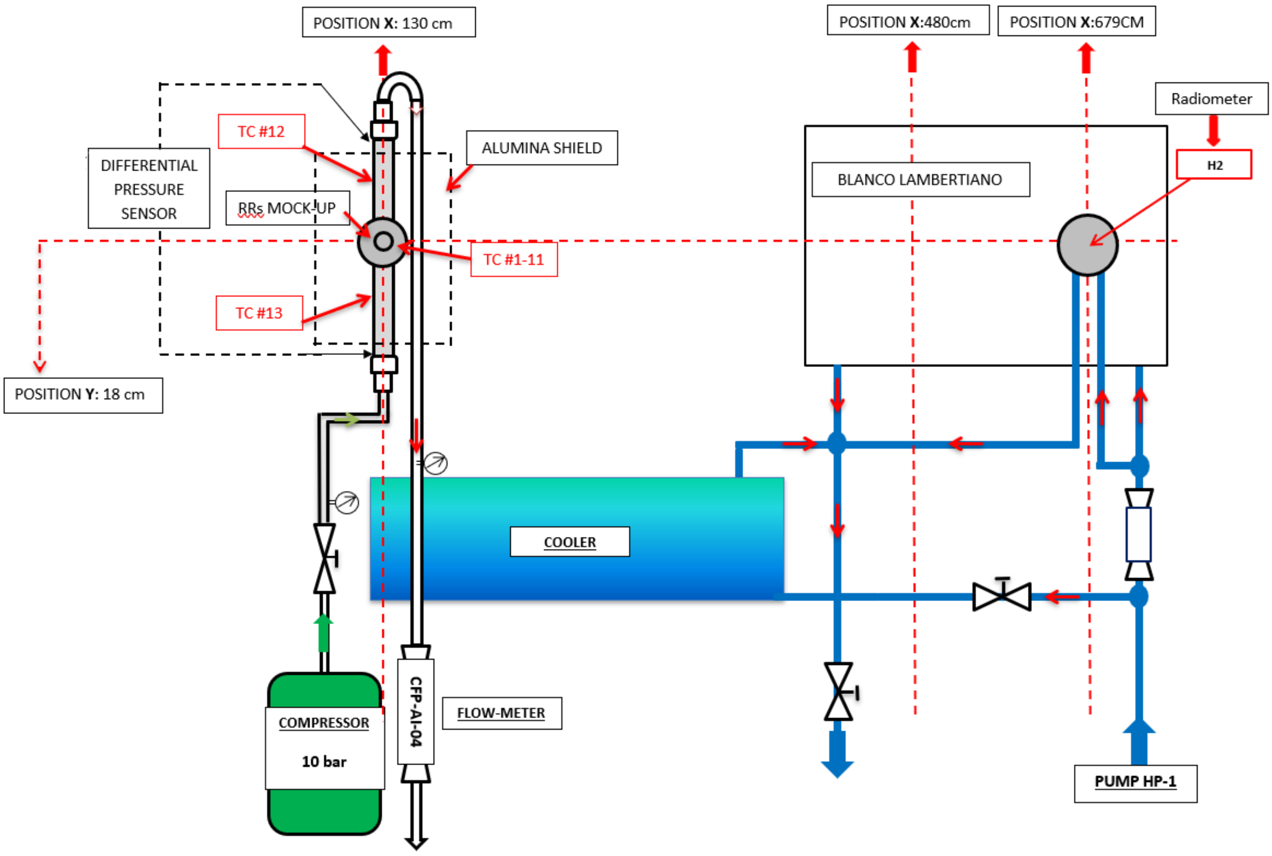

Figure 4.16: Scheme of the final testing circuit.

4.4 Measurement Instrumentation

During an experimental campaign the measurement instrumentation is surely fundamental and particular attention has to be paid on it in order to understand the error related to each reading.
Hereby follows a detailed description of all the utilized measuring instruments.

4.4.1 Thermocouples

Certainly thermocouples played a decisive and delicate role throughout the entire experimental campaign. As explained in 4.3, the mock-up is equipped with 11 thermocouples of which 3 are, unfortunately, not working. Additionally, other 2 supplementary termocouples have been installed as well into the testing circuit at the sample inlet and outlet. All 10 functioning thermocouples are of the K-type. Thermocouples are one of the commonly used thermometers that can be used to quantify temperature. As shown in Figure 4.17, a thermocouple consists of a circuit made of two dissimilar and mostly homogeneous wires. When the temperature of the two junctions is different, a small current flows through the circuit, as first discovered by Seebeck in 1823.

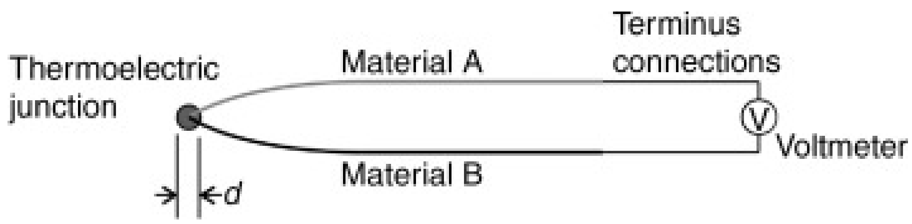

Figure 4.17: Logic scheme of a Thermocouple [36].

This current, often called the “Seebeck effect", is proportional to the temperature difference between the two junctions, the hot one or thermoelectric junction which is the measuring one and the cold one or Terminus connection which is the reference one extremity [36].
Different types of thermocouples are classify with alphabetic letters according to the couple of metals of which the thermocouple circuit is composed of (EN IEC 60584-1). Different metal combinations correspond to different Seebeck coefficients and therefore different characteristics in terms of temperature range, durability, vibration resistance, chemical resistance and application compatibility.
Type J, K, T and E are “Base Metal” thermocouples, the most common types of thermocouples while type R, S, and B thermocouples are “Noble Metal” thermocouples, which are used in high temperature and specific applications [37].
In Table 4.1 below is shown an example of operating ranges and tolerance, depending on the class, for each aforementioned typology of thermocouples. The thermocouples used in SF-60 test sessions

Table 4.1: Thermocouples Types Tolerance Chart [38].

Thermocouple Type	Alloy Combination	Operating Range	Class 1 Tolerance	Class 2 Tolerance
K	+ve Nickel Chromium (NiCr) -ve Nickel Aluminium (NiAl) (also called Chromel/Alumel)	0 to 1100°C Continuous -180 to 1300°C Intermittent	±1.5°C in range –40 to 375°C 0.004.|t| in range 375 to 1000°C	±2.5°C in range –40 to 333°C 0.0075.|t| in range 333 to 1200°C
J	+ve Iron (Fe) -ve Constantan (CuNi)	0 to 750°C Continuous -180 to 800°C Intermittent	±1.5°C in range –40 to 375°C 0.004.|t| in range 375 to 750°C	±2.5°C in range –40 to 333°C 0.0075.|t| in range 333 to 750°C
T	+ve Copper (Cu) -ve Constantan (CuNi)	-185 to 300°C Continuous -250 to 400°C Intermittent	±0.5°C in range –40 to 125°C 0.004.|t| in range 125 to 350°C	±1.0°C in range –40 to 133°C 0.0075.|t| in range 133 to 350°C
N	+ve Nicrosil -ve Nisil	0 to 1100°C Continuous -270 to 1300°C Intermittent	±1.5°C in range –40 to 375°C 0.004.|t| in range 375 to 1000°C	±2.5°C in range –40 to 333°C 0.0075.|t| in range 333 to 1200°C
E	+ve Nickel Chromium (NiCr) -ve Constantan	0 to 800°C Continuous -40 to 900°C Intermittent	±1.5°C in range –40 to 375°C 0.004.|t| in range 375 to 800°C	±2.5°C in range –40 to 333°C 0.0075.|t| in range 333 to 900°C
KCA/KCB Compensating for Type K	+ve Nickel Chromium -ve Constantan	0 to 100°C (Measuring Junction to 900°C)	N/A	±2.5°C
RCA/SCA Compensating for Type R and S	+ve Copper -ve Copper Nickel	0 to 100°C (Measuring Junction to 1000°C)	N/A	RCA ±2.5°C RCB ±5.0°C

are K-type thermocouples, as already said above, of Tolerance Class-1 specifically. Therefore they have a calibration uncertainty of ± 1.5 C in the range between -40 °C and +375 °C with a correction equal to 0.4% times the actual temperature in the case of the range between +375 °C and +1000 °C accordingly to what is shown in Figure 4.1.

The wires of the thermocouples are protected from the surrounding ambient by a sealed sheath. The sheath is usually made of stainless steel or Inconel®. In particular, the latter works better at high temperatures while the former is often preferred because of its wide chemical compatibility.

The measuring junction of the thermocouples can have several configurations as it is shown below in Figure 4.18.

In the case of isolated-from-sheath configuration the two wires are immersed in an electrical insulated material and the active sensitive sheath surface region extends over a 2 mm length from the end of the sensor. This explains why, being the used thermocouples of this types, the readings between TC #1 and TC #9 might vary a lot between each other as the 2 mm sensitive tip might touch the RRs material, air flow or even both.

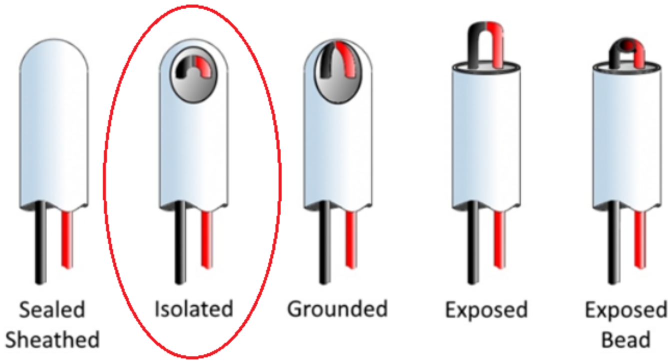

Figure 4.18: Different Thermocouples Shealth Configurations, the utilized one is circled in red [39].

4.4.2 Heat Flux Meter

The concentrated solar radiation distribution obtained in the Solar Furnace SF-60 can be approximated with a gaussian shape function [40]. The solar flux distribution in question is mapped every year by means of a CCD camera, a lambertian target and a radiometer.

The solar radiation is focused on the lambertian target which constists of an aluminium plate sprayed with alumina in order to reflect, isotropically, the solar rays onto the CCD-camera. The CCD camera views the reflected light and converts it in an iso-flux grey-scaled levels map. In order to avoid self-heating errors, the target is constantly water cooled (see Figure 4.16). On the surface of the lambertian plate a radiometer is installed. The radiometer allows to measure the incident concentrated solar heat flux in several points, calibrating in this way the whole measurement system [35, 41]. Specifically, the radiometer is a Vattel circular foil calorimeter, also called thermogage. It is composed by a thin foil disk surrounded by a cylindrical heat sink. Both the foil disk and the top surface of the cylinder are irradiated. These two components are made of constantan and copper, respectively, that are two complimentary T-type thermocouples metals. The thermogage, like thermocouples do, takes advantage of the Seebeck effect, thus it is possible to measure the temperature difference between the center of the circular disk and the heat sink cylinder, starting from the electrical voltage arisen between these two points, as is shown in Figure 4.19. This temperature difference is directly proportional to the incident heat flux however, in order to obtain the correct transfer function between input (incident heat flux) and output (measured voltage), a calibration is strictly needed [42, 43, 44].

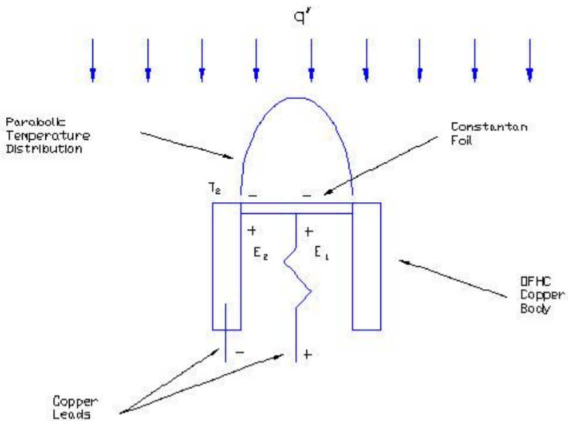

Figure 4.19: Thermogauge Working Principle [43]

The entire procedure is repeated for different planes at different distances from the parabolic concentrator in order to collect more data and, successively, find the best fitting curve. The reference plane is the focal one [35].
In order to reproduce the real solar radiation distribution the gaussian function represented by the following equation can be used [41]:

$$G = G_{peak} \cdot exp(-\frac{1}{2} \cdot (\frac{x^2}{s_x^2} + \frac{y^2}{s_y^2})) \quad [kW/m^2] \tag{4.1}$$

In the equation above G_{peak} is the concentrated solar radiation estimated at the focus point (i.e. the peak value) and both s_x and s_y are the gaussian deviation factors. These last two parameters have been evaluated considering the best fitting gaussian curve between the two given experimental points, both in x and z direction, see Figure 4.20.

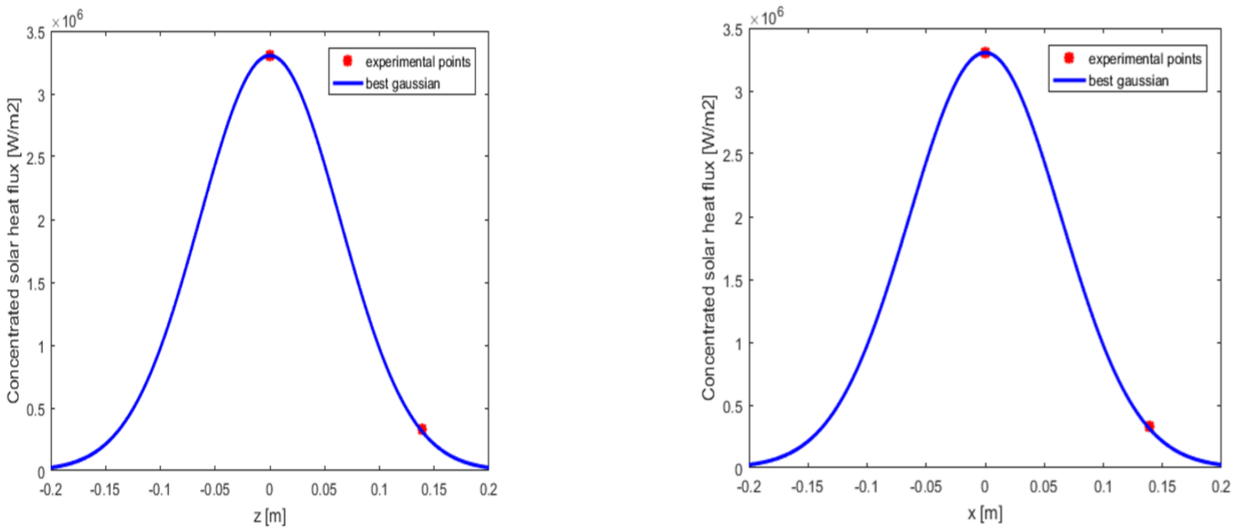

(a) (b)

Figure 4.20: (a) Best fit gaussian in x direction; (b) Best fit gaussian in z direction [42]

The resulting standard deviation factors are s_x = 0.064 and s_y = 0.064, therefore a symmetrical distribution is considered. These results are also comparable with the previous values find in literature with the old heliostat installed, s_x = 0.064 and s_y = 0.061 or also s_x = s_y = 0.0625 (symmetrical distribution) [41, 42].
During the years, a systematic error made by these sensors when applied to concentrated solar radiation measurement has been detected [44]. This error is due to the fact that the sensor calibration is made using a black-body at 850 °C [43, 35, 42]. In fact, the irradiated surface of the sensor is covered by a black coating, in order to improve its absorptance and increase the output signal intensity. At a commercial level different types of coatings are available, however Zynolite® is the preferred one according to literature [44], while for high heat flux measurement (such as the Solar Furnace application) only colloidal graphite is recommended [42, 44, 35].
Indeed, the spectral absorptivity of the black coating varies with the wavelength and a black body radiation spectrum is different from the solar spectrum, therefore the total absorbed power in the two cases is different as shown in Figure 4.21 [44].
This systematic error has already been considered by the PSA technicians and therefore their solar heat flux output value is considered to be quite reliable with only an error of ± 3%, as they affirm.

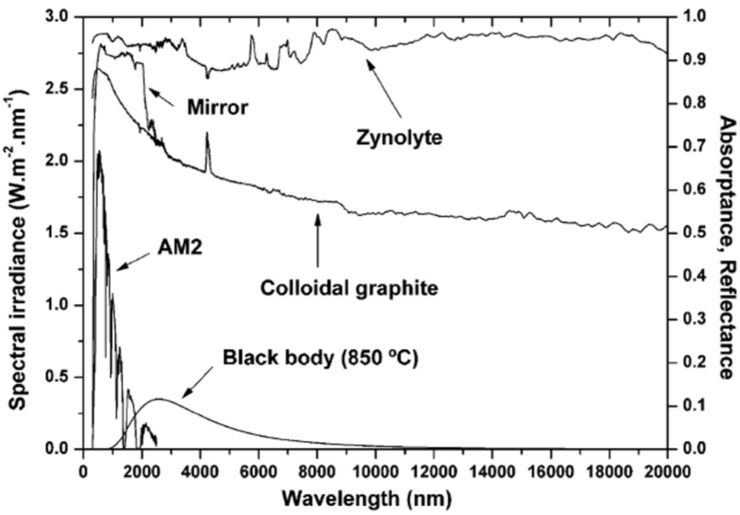

Figure 4.21: Spectral Irradiance of different material vs Wavelength [44]

4.4.3 Flow-meter

The flowrate is one of the variable parameter of the already investigated sensitivity analysis, see 3, and therefore this value also plays a fundamental role into the experimental campaign analysis. In fact, a low accuracy and a non suitable calibration of the measuring instrument would lead to more inaccurate experimental results of the thermocouples inside the RRs mock-up.
In the SF-60 the air flowrate passing though the sample circuit is measured and controlled by means of a flow-meter with an integrated control system. Specifically the utilized model is the Bronkhorst High-Tech model F-203AV Mass Flow Controllers (MFCs).
F-203AV MFCs are suited for precise control of virtually all conventional process gases. In particular, the MFC consists of a thermal mass flow sensor, a precise control valve and a microprocessor based on a PID controller with signal and field-bus conversion. As a function of a setpoint value, the flow

controller swiftly adjusts the desired flow rate. The mass flow, expressed in normal litres per minute or normal cubic metres per hour, is provided as analog signal or digitally via RS232 or field-bus. The flow range, wet materials and orifice size for the control valve are determined depending of the type of gas and the process conditions of the application, therefore this implies that a calibration is needed [45].

The heart of the thermal mass flow meter/controller is the sensor, that consists of a stainless steel capillary tube with resistance thermometer elements [45]. The entire measuring principle, which scheme is shown in Figure 4.22 below, is based on this sensor.

A part of the gas flows through this bypass sensor, and is warmed up heating elements. Consequently the measured temperatures T_1 and T_2 drift apart. The temperature difference is directly proportional to mass flow through the sensor.

In the main channel Bronkhorst High-Tech applies a patented laminar flow element consisting of a stack of stainless steel discs with precisionetched flow channels. Thanks to the perfect flow-split the sensor output is proportional to the total mass flow rate [45].

The accuracy of the flow meter depends on the type of gaseous fluid and on the calibration of the instrument itself, however in its data sheet, see [45], are described some degrees of accuracy concerning air.

The stated accuracy of the sensor, see [45], is of $\pm$ 0.5% of the actual flowrate reading plus a $\pm$ 0.1% of the full scale (F.S.) of the instrument (1650 l/min in this specific case), additionally another $\pm$ 0.1% of the F.S. error has still to be added due to some uncertainty related to the control stability. In case of quick uses of about 2 minutes the uncertainty related to the F.S. increases up to 2% while the most accurate precision comes with a warm-up time of, at least, 30 minutes.

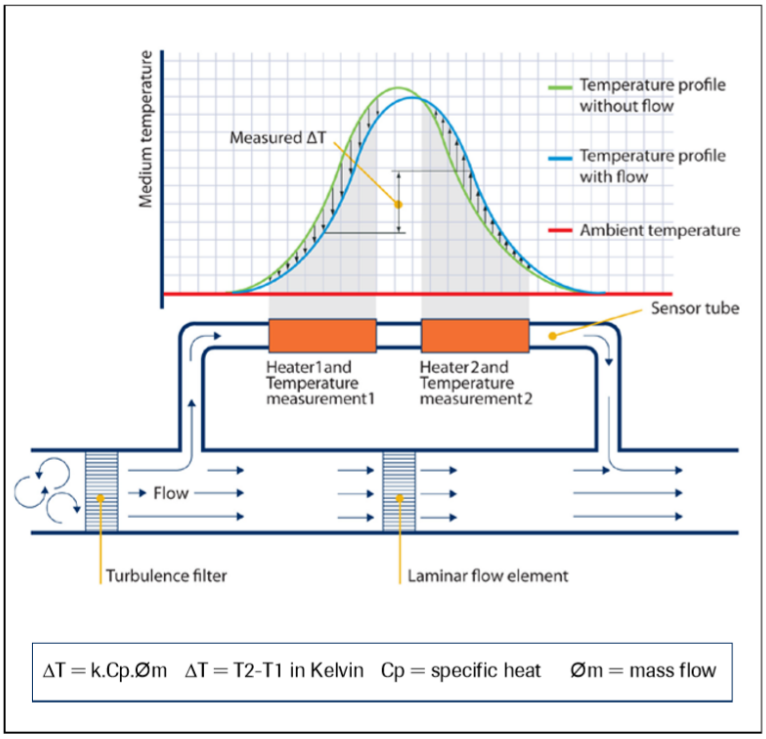

Figure 4.22: Scheme of the Flow-meter measuring principle [45]

4.4.4 Differential Pressure Drop Sensor

As not only thermal but also pure hydraulic tests are performed at the SF-60 in the Plataforma Solar de Almeria, an instrument to measure the pressure drop (or loss) across the tested sample is needed in order to validate the pure hydraulic CFD simulation results and to extrapolate an hydraulic characteristic of the mock-up.

Differential pressure sensors are at the heart of various instruments that measure flow, pressure and liquid level of many industrial processes. Specifically, the differential pressure sensors are larger and more robust than the semiconductor variety (pressure sensors only) but the concept is the same: they measure the difference in pressure across a diaphragm using a strain gauge thin-film resistor network or differential capacitance sensors [46].

A scheme of the Differential Pressure Sensor measuring area is shown in Figure 4.23.

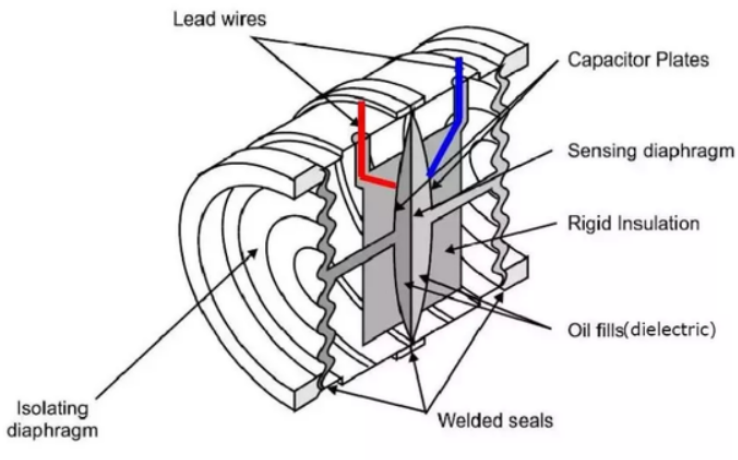

Figure 4.23: Functioning Scheme of a Differential Pressure Sensor [46].

One side of the diaphragm is connected to the low pressure port and the other side of the diaphragm to the high pressure port. The diaphragm flexes and is sensed as an electrical signal that is proportional to the difference in the two pressures [46]. Important is to highlight that differential pressure measurement is not concerned whether the lower of the two pressures is at a vacuum, atmospheric or some other pressure, as it happens with absolute pressure sensors instead. It is only interested in the difference between the two.

To withstand harsh industrial environments such as factories, refineries or water treatment plants the sensors are housed in stainless steel or other exotic materials and the electrical signal is run through a built-in microprocessor that outputs a high resolution “4 to 20” milliamp signal or digital HART signal and are called transmitters.

The utilized Differential Pressure Sensor is of the PRE-28 typology with a P-type connection. Its active element is a piezoresistance silicon sensor separated from the medium by separating diaphragm and a specially selected type of manometric fluid (air in this case). The measuring range goes up to 4 bar for this specific instrument with an accuracy of ± 0.40% on the actual reading, at this value has to be added another ± 0.2%/year instability error which goes up to ± 1.4% as the instrument has been operating for 7 years at the PSA. In addition to this another last ± 0.3%/10°C is added to the

total error bringing the total value to the number of $\pm$ 2.40% of inaccuracy for this specific instrument which has to be considered whenever data connected to this instrument are analized [47].
An image of the testing circuit seen from behind, illustrating the location of the two pressure taps (high and low pressure ports highlighted in red), is shown in Figure 4.24.

Figure 4.24: View of the two taps of the differential pressure sensor.

4.5 Test Matrix

During the two weeks test campaign, unfortunately, bad weather conditions have occurred, comprehending strong wind gusts, many clouds and even some rainy days. An example of two days, one full of wind gusts and the other one with a poor DNI due to many clouds and rain, are shown in Figure 4.25 and Figure 4.26, respectively.
However, in spite of the adverse climatic conditions, there were some sunny days that allowed to perform several tests in order to cover the widest possible range of operating conditions. In particular, the RRs Mock-up sample has been tested by using different flow-rates and several concentrated solar heat fluxes to resemble the operating cases simulated in Section 3.

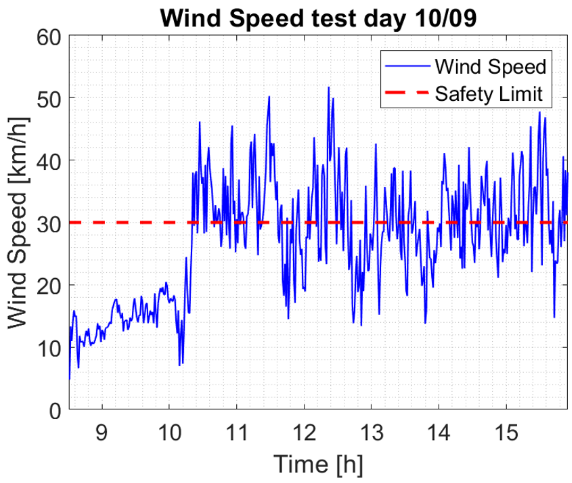

Figure 4.25: Example of a day with wind gusts.

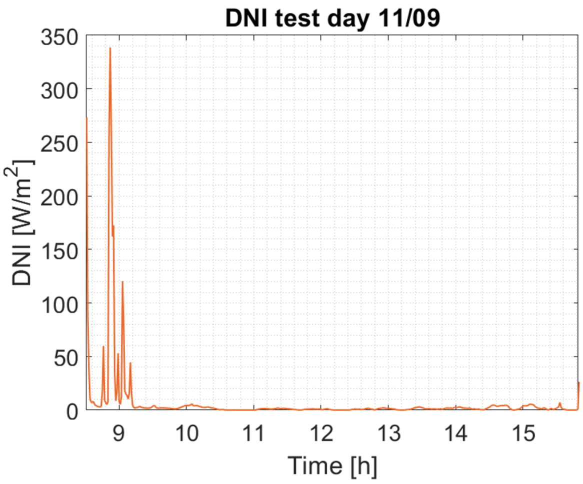

Figure 4.26: Example of a cloudy and rainy day.

Throughout the two experimental test weeks different tests sessions were made. Generally speaking they can be subdivided in pure hydraulic tests and thermal and fluid dynamic tests which are reported below.

4.5.1 Pure Hydraulic Tests

In these Test Sessions the only one variable parameter was the flow-rate as no concentrated solar heat flux was applied on the mock-up target since this is a Pure Hydraulic Tests. Specifically, the flowrate was changed by means of a control on the compressor checked by the flow-meter located at the end of the air circuit as it was done on the previous thermo-hydraulic tests, see 4.5.2.
Bad weather conditions occurred during the two weeks experimental campaign, therefore these tests were usually made when the DNI was not suitable to make any thermal tests.

- Test Session 1

This first test session was performed on September 13^{th} since weather conditions were not great (see 4.5.2, Figure 4.28). Specifically, the value of the flowrate was changed and the total raw pressure drop between the high and low pressure taps of the differential pressure transmitter collected.
Table 4.2 lists all the pure hydraulic tests made on the first session together with the ones collected on the second session. Tests are listed by their number, followed by an H that stands for Hydraulic and then the number of the test session.

- Test Session 2

This second and last test session was performed on September 17^{th} since weather conditions were not great (see 4.5.2, Figure 4.30). Specifically, as the flowrate was changed the total raw pressure drop between the high and low pressure taps of the differential pressure transmitter was collected. These tests are exactly like the ones of the previous test session, however it is still a good idea to run them more than just once as this would result in more accurate and reliable data if the measured values remain almost constant between the two different sessions. This second session results are, indeed, very close to the previous one.

Table 4.2 lists all the pure hydraulic tests made on the second session together with the ones collected on the first session. Tests are listed by their number, followed by an H that stands for Hydraulic and then the number of the test session.

Table 4.2: Pure Hydraulic Test Sessions Operating Conditions.

#Test -H Test Session	**Flowrate** $[l/min]$	**Inlet Pressure** $[bar]$	**Ambient Temperature** **[°C]**	**Outcome**
#1-H1	200	9.5	19.3	OK
#2-H1	300	9.6	19.6	OK
#3-H1	400	9.6	20.1	OK
#4-H1	500	9.7	20.3	OK
#5-H1	600	9.7	20.8	OK
#6-H1	700	9.8	21.2	OK
#7-H1	800	9.8	21.3	OK
#1-H2	200	9.5	18.2	OK
#2-H2	300	9.6	18.3	OK
#3-H2	400	9.6	19.1	OK
#4-H2	500	9.7	19.5	OK
#5-H2	600	9.7	19.9	OK
#6-H2	700	9.8	20.3	OK
#7-H2	800	9.8	21.0	OK

4.5.2 Thermal and Fluid Dynamic Test Sessions

In these Test Sessions the two variable parameters were the flow-rate and the concentrated solar heat flux. Specifically, the former was changed by means of a control on the compressor checked by the flow-meter located at the end of the air circuit, while the latter was modified by varying the shutter aperture (depending on the actual solar irradiation of that moment) checked by the radiometer located on the lambertian target.
Figure 4.27 below shows an example of what the operating circuit looks like during a test session.

Figure 4.27: Example of the operating circuit during a test session.

- Test Session 1

This first test session was performed on September 13^{th}, unfortunately as the weather conditions were not excellent only few operating conditions were tested, see the day's DNI shown in Figure 4.28. Specifically, an attempt to test another operating condition was done, however this last test (see Table **??**) was invalidated due to the presence of many clouds that prevented to keep the concentrated heat flux constant.
Table 4.3 and Table 4.4 below list all the tests made on the first session together with the ones collected on the other sessions. Tests are listed by their number, followed by a TH that stands for Thermo-Hydraulic and then the number of the test session.

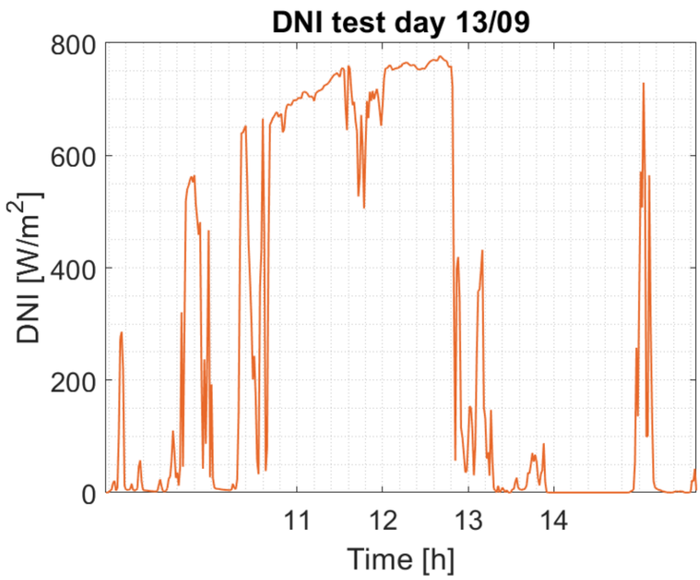

Figure 4.28: Test Session 1 DNI.

- Test Session 2

This second test session was performed on September 16^{th}, which was the most productive day of the entire experimental campaign as the weather conditions were suitable and quite constant which allowed to test several operating conditions, see the day's DNI shown in Figure 4.29. However, even thought the DNI was good and the sky clear, test #4 was still invalidated due to some random clouds passing by (see Table **??**). Test #5 is a successful second attempt to collect the data on the invalidated test #4. Additionally test #1 has a slight higher heat flux peak since it was performed during the early morning when the sun was still rising and the DNI increasing steadily, while the shutter aperture was set at the beginning of that test.
Table 4.3 and Table 4.4 below list all the tests made on the second session together with the ones collected on the other sessions. Tests are listed by their number, followed by a TH that stands for Thermo-Hydraulic and then the number of the test session.

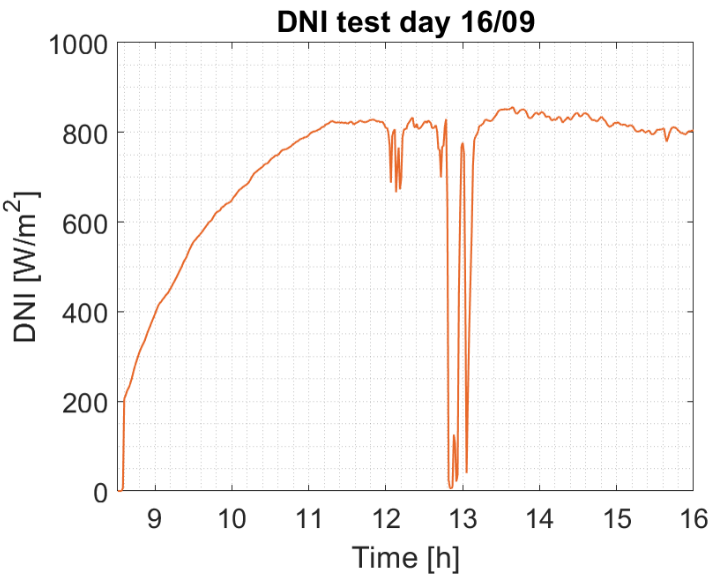

Figure 4.29: Test Session 2 DNI.

- Test Session 3

This third test session was performed on September 17^{th}, which was a pretty cloudy day with a very variable DNI, see Figure 4.30. The outcome of this test session is, unfortunately, poor. In fact, only one type of operating conditions could be tested as the test #2 was invalidated due to the presence of clouds passing by. No more tests could be run as there was no stable and suitable DNI.
Table 4.3 and Table 4.4 below list all the tests made on the third session together with the ones collected on the other sessions. Tests are listed by their number, followed by a TH that stands for Thermo-Hydraulic and then the number of the test session.

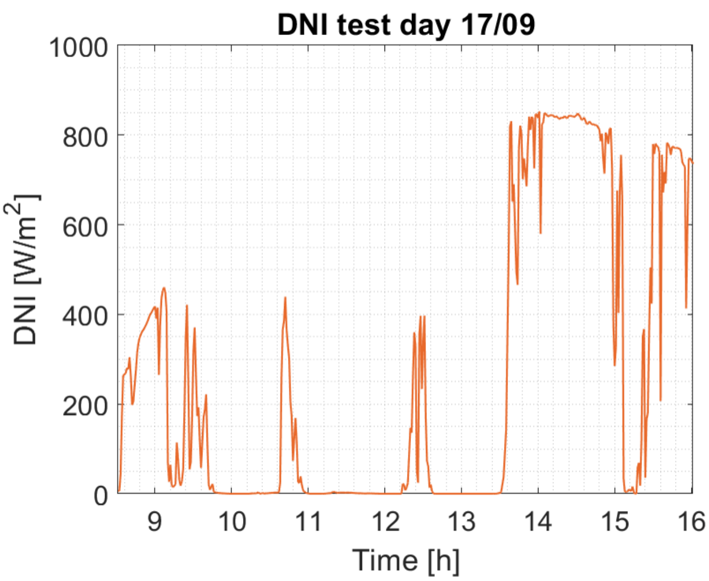

Figure 4.30: Test Session 3 DNI.

- Test Session 4

This fourth test session was performed on September 18^{th}, which was a quite cloudy day with a very variable DNI only during the central hours of the day as it is also shown in Figure 4.31. Also the outcome of this test session is, unfortunately, poor. In fact, only one type of operating conditions could be tested as the test #1 was invalidated due to the continuosly growing DNI which resulted to a final heat flux which was completely different (much higher) than the initial one, leading to operating conditions that were far from the ones at which the sample was supposed to work at. Test #3 was simply invalidated due to the presence of clouds passing by which made the DNI unstable. Finally test #4 was valid as it was performed during a DNI stable period, however the PSA instrumentation had some problems and reset shutting down. This cancelled the data of this last test which was, then, repeated the day after.

Table 4.3 and Table 4.4 below list all the tests made on the fourth session together with the ones collected on the other sessions. Tests are listed by their number, followed by a TH that stands for Thermo-Hydraulic and then the number of the test session.

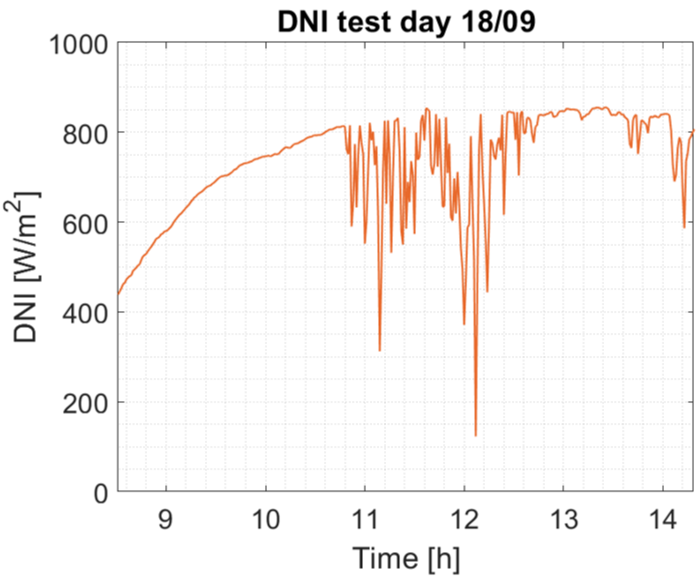

Figure 4.31: Test Session 4 DNI.

- Test Session 5

This last test session was performed on September 19^{th}, which was a decent sunny day with just some clouds that were passing by from time to time. The day's DNI is shown in Figure 4.31. During this last experimental session a total of three tests were performed and their data collected. Test #1 was a second attempt to collect data on the last test of the previous test session which was lost due to technical problems at the PSA. Test #4, unfortunately, is invalid because at the end of the day several clouds appeared in the sky obscuring the target of the SF-60.

Table 4.3 and Table 4.4 below list all the tests made on the last session together with the ones collected on the other sessions. Tests are listed by their number, followed by a TH that stands for Thermo-Hydraulic and then the number of the test session.

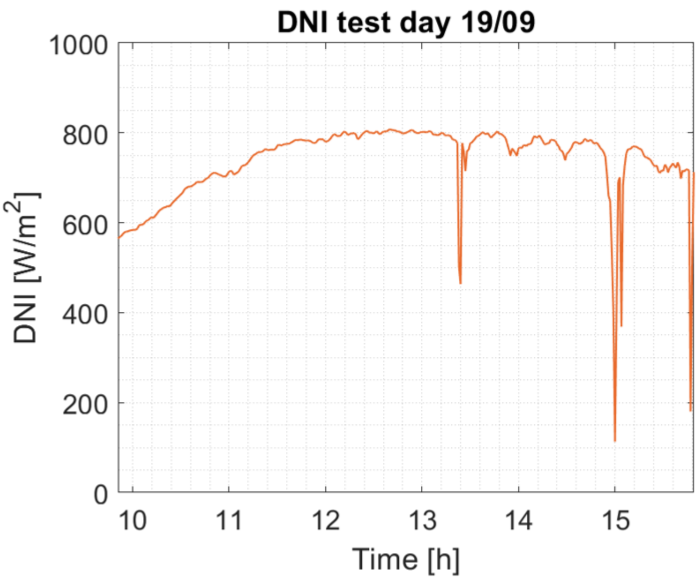

Figure 4.32: Test Session 5 DNI.

Table 4.3: Thermo-Hydraulic Test Sessions Operating Conditions - 1.

#Test -TH Test Session	**Flowrate** $[l/min]$	**Pressure In** $[bar]$	**Heat Flux Peak** $[kW/m^2]$
#1-TH1	300	9.7	107
#2-TH1	200	9.7	112
#3-TH1	100	9.6	-
#1-TH2	100	9.6	131
#2-TH2	100	9.6	308
#3-TH2	200	9.7	502
#4-TH2	100	9.6	-
#5-TH2	100	9.6	500
#6-TH2	300	9.7	702
#1-TH3	300	9.7	500
#2-TH3	300	9.7	-
#1-TH4	300	9.7	-
#2-TH4	300	9.7	298
#3-TH4	200	9.6	-
#4-TH4	200	9.6	295
#1-TH5	200	9.6	299
#2-TH5	200	9.6	727
#3-TH5	200	9.6	102
#4-TH5	100	9.5	-

Table 4.4: Thermo-Hydraulic Test Sessions Operating Conditions - 2.

#Test -TH Test Session	Shutter Aperture [%]	Ambient Temp. [°C]	Outcome
#1-TH1	11.5	20.1	OK
#2-TH1	11.5	21.0	OK
#3-TH1	9.50	25.9	INVALID
#1-TH2	16.0	22.3	OK
#2-TH2	26.0	27.5	OK
#3-TH2	32.5	27.6	OK
#4-TH2	31.2	31.2	INVALID
#5-TH2	31.0	29.1	OK
#6-TH2	40.0	29.4	OK
#1-TH3	25.5	25.0	OK
#2-TH3	18.70	27.4	INVALID
#1-TH4	32.0	21.8	INVALID
#2-TH4	21.5	27.0	OK
#3-TH4	20.7	29.2	INVALID
#4-TH4	18.9	31.1	LOST
#1-TH5	24.2	23.6	OK
#2-TH5	39.4	31.1	OK
#3-TH5	7.00	33.2	OK
#4-TH5	7.4	28.2	INVALID

4.6 Analysis of the Test Results

The raw tests data collected from the two weeks experimental campaign at the Sf-60, Plataforma Solar de Almeria, have been successively post-processed. The results are shown in the two sections below.

4.6.1 Pure Hydraulic Results

Pure hydraulic data have been collected throughout two experimental test sessions. To process the aforementioned data, an average between the results has been made. The final outcome, including the total raw pressure drop between the high and low pressure taps of the differential pressure transmitter, is presented below in Table 4.5.

Table 4.5: Pure Hydraulic Raw Results.

Flowrate		Reynolds	Raw Pressure Drop	Flowmeter Error		Diff. Pressure Error
$[l/min]$	$[g/s]$		$[mbar]$	$[l/min]$	$[g/s]$	$[mbar]$
200	4.30	$1.99 \cdot 10^4$	10	$\pm$ 4.3	$\pm$ 0.09	$\pm$ 0.24
300	6.45	$2.99 \cdot 10^4$	20	$\pm$ 4.8	$\pm$ 0.10	$\pm$ 0.48
400	8.60	$3.99 \cdot 10^4$	40	$\pm$ 5.3	$\pm$ 0.11	$\pm$ 0.96
500	10.8	$4.99 \cdot 10^4$	60	$\pm$ 5.8	$\pm$ 0.13	$\pm$ 1.44
600	12.9	$5.98 \cdot 10^4$	90	$\pm$ 6.3	$\pm$ 0.14	$\pm$ 2.16
700	15.1	$6.98 \cdot 10^4$	130	$\pm$ 6.8	$\pm$ 0.15	$\pm$ 3.12
800	17.2	$7.98 \cdot 10^4$	180	$\pm$ 7.3	$\pm$ 0.16	$\pm$ 4.32

Table 4.5 contains the measurement errors since the values above have some uncertainty due to the instrumentation. In fact, the flow-meter has some unreliability which depends both on the actual reading and on its Full Scale limit (see 4.4.3), while also the differential pressure transmitter has an error which depends only on the measured value (see 4.4.4).
Indeed, every measuring error is important and has to be taken into account during the post-processing of the raw data to provide a suitable error bar. A linear sum dependency between the two aforementioned instruments has been adopted to estimate the total error uncertainty on the raw collected data. Raw Pressure Drop results with their relative vertical and horizontal error bars given by the differential pressure transmitter and flow-meter errors, respectively, are shown in Figure 4.33 below.

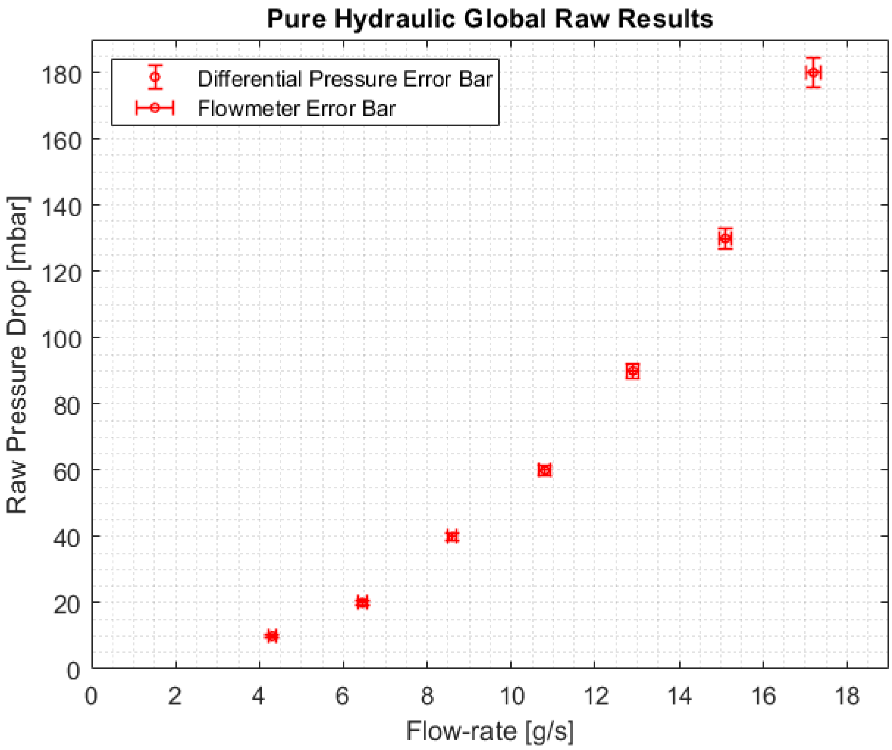

Figure 4.33: Pure Hydraulic Results - Global Raw Pressure Drop.

Raw results have to be post-processed. Specifically, the high and low pressure tap of the differential pressure sensor are not positioned right at the inlet and outlet of the mock-up respectively (see Figure 4.24), therefore both minor and major losses still have to be taken into account. The Raw Pressure Drop will thus be reduced considering all the head losses that take place into the pipe junctions and many valves across the testing circuit.
To get a better idea of how minor and major pressure losses have been estimated, a logic scheme of the test circuit is shown in Figure 4.34. The geometrical diameters are already shown in said picture, while the lengths (which are not in scale in the image) are of the following values:

- $L_1 = L_6 = 12$ cm;
- $L_2 = L_7 = 8$ cm;
- $L_3 = 3$ cm;

- $L_4 = L_5 = 4$ cm;
- $L_8 = 6$ cm;

Once the geometrical characteristics of the circuit were established, the raw pressure drop process have been divided into two sections, minor and major losses.

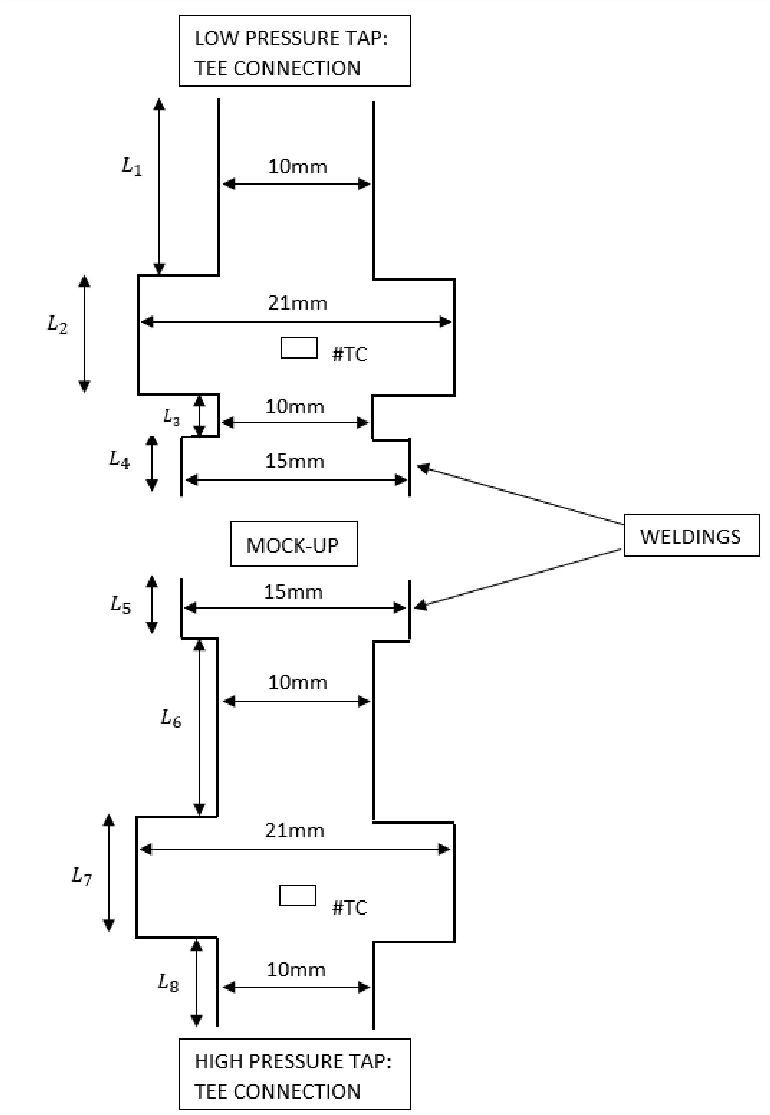

Figure 4.34: Post-process Circuit Logic Scheme.

1. Major Losses

Major losses, which are associated with frictional energy loss per length of pipe depends on the flow velocity, pipe length, pipe diameter, and a friction factor based on the roughness of the pipe and, finally, whether the flow is laminar or turbulent (i.e. the Reynolds number of the flow).
Although the head loss represents a loss of energy, it does not represent a loss of total energy of the fluid. The total energy of the fluid conserves as a consequence of the law of conservation of energy. In reality, the head loss due to friction results in an equivalent increase in the internal energy (increase in temperature) of the fluid.

In general, the major head loss is roughly proportional to the square of the flow rate in most engineering flows (fully developed, turbulent pipe flow).
The two following equations have been used to estimate the major losses of the testing circuit. The former (see Equation 4.2) is the Colebrook equation [48] which is valid as the flow is turbulent, as can be checked by the Reynolds number in Table 4.5, while the latter (see Equation 4.3) is the general equation to define the major losses of a pipe [48].
The roughness used into the Colebrook equation is ϵ = 0.06 mm [49]. Results of the major head losses estimations are shown in Table 4.6.

$$\frac{1}{\sqrt{f}} = -2log\left(\frac{\epsilon/D}{3.7} + \frac{2.51}{Re\sqrt{f}}\right) \tag{4.2}$$

$$\Delta P_{major} = \frac{1}{2} f \cdot \frac{L}{D} \cdot \rho \cdot V_{avg}^2 \tag{4.3}$$

2. Minor Losses

Although they often account for a major portion of the head loss, especially in process piping, the additional losses due to entries and exits, fittings and valves are traditionally referred to as minor losses. These losses represent additional energy dissipation in the flow, usually caused by secondary flows induced by curvature or recirculation. The minor losses are any head loss present in addition to the head loss for the same length of straight pipe.
Like pipe friction, these losses are roughly proportional to the square of the flow rate. The general equation used to estimate the minor losses of the testing circuit (see Equation 4.4 is shown below [48]. K_{loc}, defined as the loss coefficient of each entry, exit, fitting or valve of the pipe, all contributing to the total head loss. Although K_{loc} appears to be a constant coefficient, it varies with different flow conditions. Generally, factors affecting the value of K include: the exact geometry of the component in question; the flow Reynolds Number; proximity to other fittings, etc.
Each minor loss has been calculated using the average velocity of the specific section of pipe, depending on its diameter.

$$\Delta P_{minor} = \frac{1}{2} \cdot \sum K_{loc} \cdot \rho \cdot V_{avg}^2 \tag{4.4}$$

Hereby follow the chosen values of the all the loss coefficients of the testing circuit [48]:

- $K_{loc,1}$ = 1 for the inlet Tee junction between the low pressure tap and the testing circuit;
- $K_{loc,2}$ = 0.8 for the enlargement between L_1 and L_2;
- $K_{loc,3}$ = 0.7 for the presence of a thermocouple inserted into the second section, throughout L_2;
- $K_{loc,4}$ = 0.15 for a welding done on the section of length L_2;
- $K_{loc,5}$ = 0.5 for the shrinkage between L_2 and L_3;
- $K_{loc,6}$ = 0.4 for the enlargement between L_3 and L_4;
- $K_{loc,7}$ = 0.1 for a welding done on the section of length L_4;

- $K_{loc,8}$ = 0.1 for a welding done on the section of length L_5;
- $K_{loc,9}$ = 0.4 for the shrinkage between L_5 and L_6;
- $K_{loc,10}$ = 0.8 for the enlargement between L_6 and L_7;
- $K_{loc,11}$ = 0.7 for the presence of a thermocouple inserted into the seventh section, throughout L_7;
- $K_{loc,12}$ = 0.15 for a welding done on the section of length L_7;
- $K_{loc,13}$ = 0.5 for the shrinkage between L_7 and L_8;
- $K_{loc,14}$ = 1 for the inlet Tee junction between the high pressure tap and the testing circuit;

Results of minor head loss estimation are shown in Table 4.6 while the Mock-up net Pressure Drop is presented in Figure 4.35. Specifically, the equation of that trend curve, which is reported below (see Equation 4.5), follows almost a quadratic behaviour which corresponds to the physics of the problem. A R^2 value (defined in Equation 3.4) of 80% is given by the fit curve when considering both the flow-meter and differential pressure sensor uncertainties. Its relative error area is shown in the cyan in Figure 4.35 below.

$$Y = 0.1453 \cdot X^2 \quad R^2 = 80\% \tag{4.5}$$

Table 4.6: Pure Hydraulic Mock-up Net Results.

Flowrate		**Raw Pressure Drop**	**Major Loss**	**Minor Loss**	**Mock-up Pressure Drop**
$[l/min]$	$[g/s]$	$[mbar]$	$[mbar]$	$[mbar]$	$[mbar]$
200	4.30	10	1.50	6.40	2.10
300	6.45	20	3.30	13.5	3.10
400	8.60	40	5.50	25.8	8.70
500	10.8	60	8.80	38.1	13.1
600	12.9	90	13.1	57.0	19.9
700	15.1	130	17.8	78.9	33.3
800	17.2	180	23.2	104	51.9

Although there is a certain degree of uncertainty into these net mock-up processed experimental results (see Table 4.5, the analysis outcome already seems promising as almost every point and its error bar both fall into the uncertainty R^2 area. A comparison between experimental and simulated CFD results is carried out in Chapter 5.

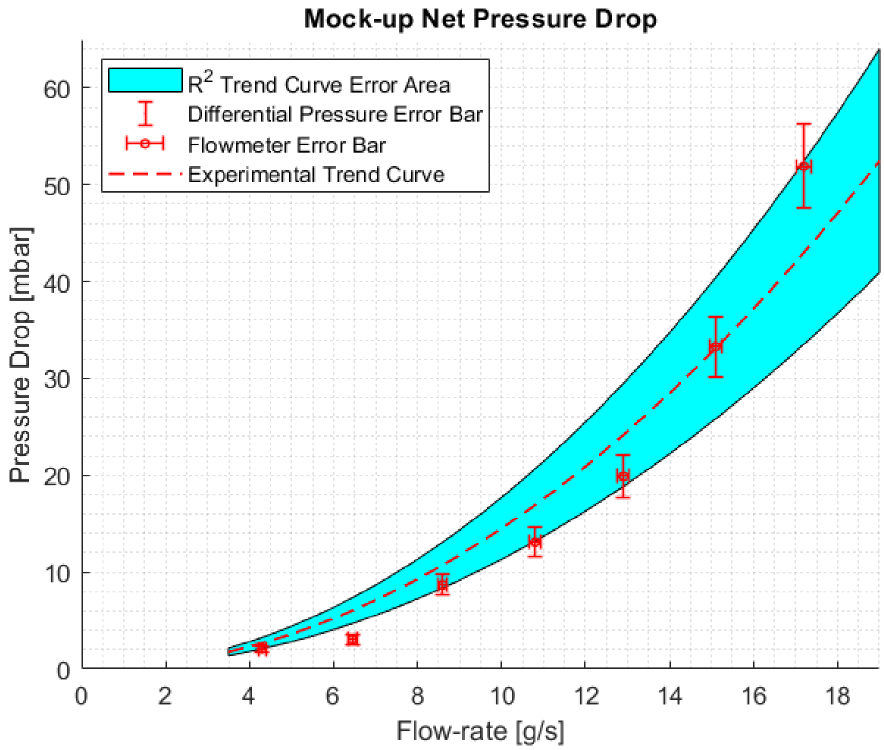

Figure 4.35: Mock-up Net Pressure Drop Curve.

4.6.2 Thermo-Hydraulic Results

Thermal and Fluid Dynamic data have been collected throughout five experimental test sessions. Since every session contains different tests performed at different operating conditions the raw data are presented independently for each of the testing session day. Results are reported by means of two options: a picture and a table for each of the test session.

For a more clear result presentation the former option does not include all of the thermocouple patterns by only few of them that have significant values and that are not redundant. In particular, TCs #1, #3, #5, #10 and #13, whose location is reported in Figure 4.17, are the presented ones which give information on the inlet and outlet temperature (TCs #13 and #10, respectively), central temperature of the target (TC #5) and side temperature of the target area (TCs #1 and #3).

The latter option, instead, includes information about every thermocouple, whose reported temperature values are specifically obtained by an average over the steady state period of each test. Additionally some information about the measuring error is included into the Tables as well. This measuring error is listed for the flowmeter were it depends both on its full scale and on the actual measured value, for the radiometer (see 4.4.2) and the Thermocouples (see 4.4.1) the error is constant and equal to $\pm$ 3% and $\pm$ 1.5 °C, respectively. The constant $\pm$ 1.5 °C error of the thermocouples has to be added to each of the additional statistical error that the TCs take from each test analysis.

- Test Session 1 Results

As previously explained in 4.5.2, this first test session includes three tests of which only two are valid. All the results of this first testing day are reported in Table 4.7, while some TC patterns are shown below in Figure 4.36 where it is clear why the third test is invalid (see also Figure 4.28 for a cross check).

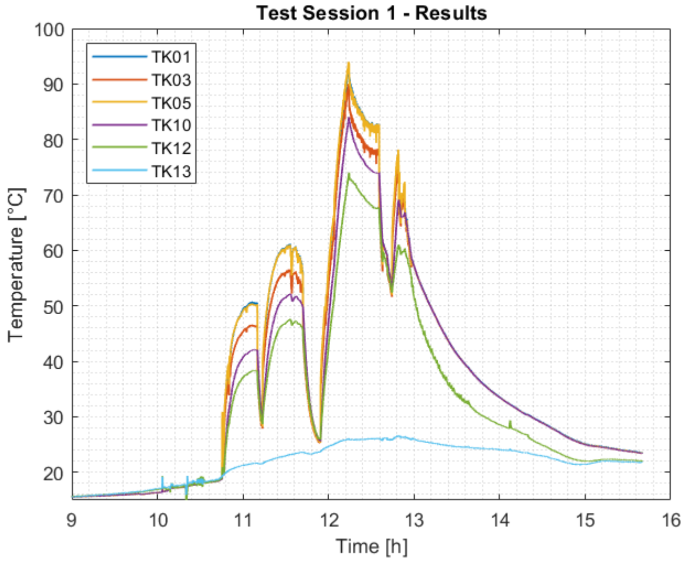

Figure 4.36: Results of the test session 1.

- Test Session 2 Results

As previously explained in 4.5.2, this second test session includes six tests of which five are valid. All the results of this second testing day are reported both in Table 4.7 and Table 4.8 while some TC patterns are shown below in Figure 4.37 where it is clear why the fourth test is invalid (see also Figure 4.29 for a cross check).

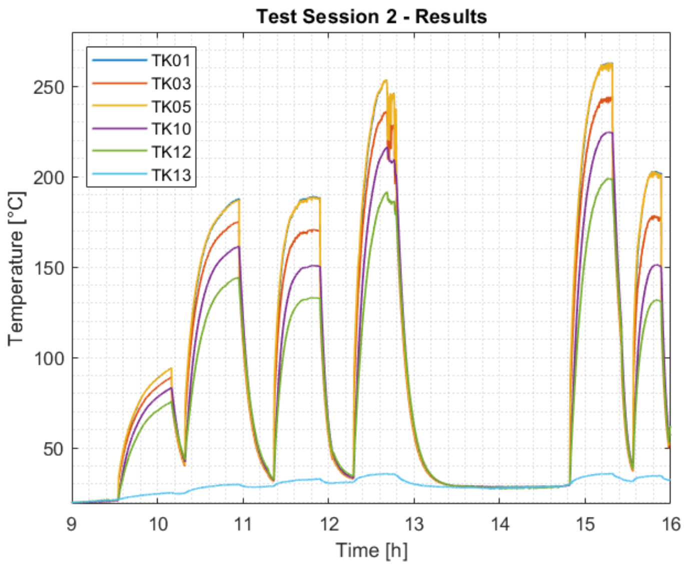

Figure 4.37: Results of the test session 2.

- Test Session 3 Results

As previously explained in 4.5.2, this third test session includes two tests of which only one is valid. All the results of this third testing day are reported in Table 4.8, while some TC patterns are shown below in Figure 4.38 where it is clear why the second test is invalid (see also Figure 4.30 for a cross check).

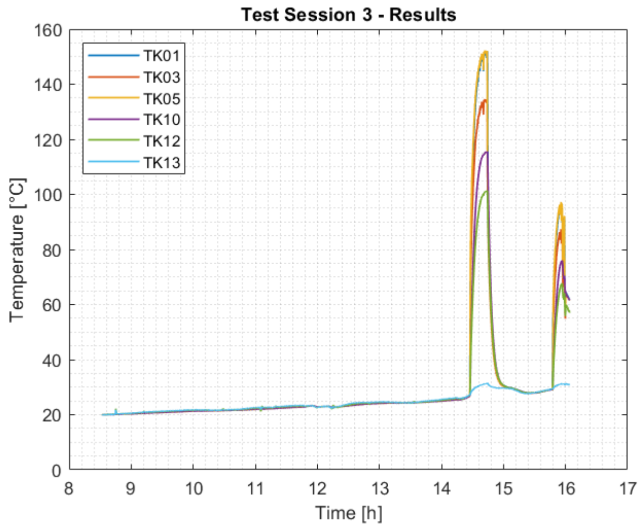

Figure 4.38: Results of the test session 3.

- Test Session 4 Results

As previously explained in 4.5.2, this fourth test session includes four tests of which only one is valid. All the results of this fourth testing day are reported in Table 4.9, while some TC patterns are shown in Figure 4.39 where it is clear why the second test is invalid (see also Figure 4.31 for a cross check). Test #4 which was then lost was performed between the 15:00 and the 16:00 of September 18^{th} 2019.

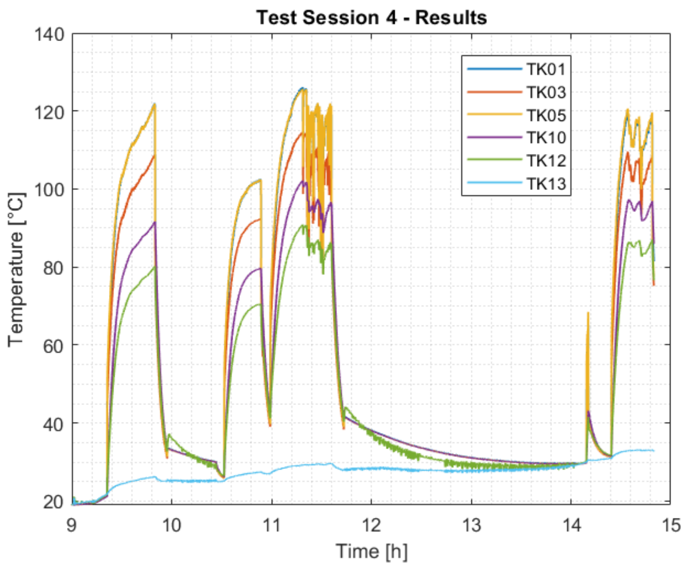

Figure 4.39: Results of the test session 4.

- Test Session 5 Results

As previously explained in 4.5.2, this last test session includes four tests of which only one is not valid (repeated twice). All the results of this last testing day are reported in Table 4.9, while some TC patterns are shown in Figure 4.40 where it is clear why the last test is invalid (see also Figure 4.32 for a cross check).

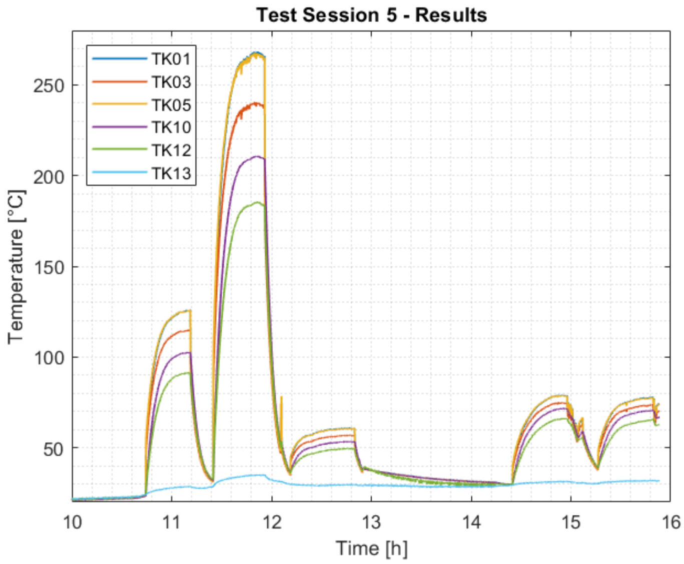

Figure 4.40: Results of the test session 5.

Table 4.7: Thermo-Hydraulic Test Sessions Results - 1.

Results	**#Test -TH Test Session 1**		**#Test - TH Test Session 2**	
	#1-TH1	#2-TH1	#1-TH2	#2-TH2
Flowrate $[l/min]$	300	200	100	100
Flowrate Error $[l/min]$	$\pm$ 4.8	$\pm$ 4.3	$\pm$ 3.8	$\pm$ 3.8
Peak Heat Flux $[kW/m^2]$	107	112	131	308
Radiometer Err $[kW/m^2]$	$\pm$ 3.2	$\pm$ 3.4	$\pm$ 3.9	$\pm$ 9.2
TCs Error [°C]	$\pm$ 1.5	$\pm$ 1.5	$\pm$ 1.5	$\pm$ 1.5
TK-01 [°C]	50.4 $\pm$ 0.4	60.6 $\pm$ 0.6	93.7 $\pm$ 0.9	187 $\pm$ 1.0
TK-02 [°C]	46.0 $\pm$ 0.4	56.6 $\pm$ 0.5	89.1 $\pm$ 1.7	176 $\pm$ 1.0
TK-03 [°C]	46.3 $\pm$ 0.4	56.2 $\pm$ 0.7	88.6 $\pm$ 2.2	175 $\pm$ 1.2
TK-05 [°C]	50.1 $\pm$ 0.4	60.5 $\pm$ 0.8	93.6 $\pm$ 2.4	186 $\pm$ 1.2
TK-06 [°C]	48.8 $\pm$ 0.5	59.0 $\pm$ 0.8	91.7 $\pm$ 3.5	181 $\pm$ 1.1
TK-07 [°C]	49.0 $\pm$ 0.5	59.4 $\pm$ 0.6	92.1 $\pm$ 2.4	184 $\pm$ 1.3
TK-08 [°C]	25.2 $\pm$ 0.4	27.5 $\pm$ 0.2	27.3 $\pm$ 0.2	33.4 $\pm$ 0.2
TK-09 [°C]	42.1 $\pm$ 0.4	51.9 $\pm$ 0.6	83.3 $\pm$ 1.2	162 $\pm$ 1.1
TK-10 [°C]	41.9 $\pm$ 0.4	51.8 $\pm$ 0.4	82.8 $\pm$ 0.6	161 $\pm$ 1.0
TK-12 [°C]	38.2 $\pm$ 0.5	47.2 $\pm$ 0.5	75.1 $\pm$ 0.6	144 $\pm$ 0.9
TK-13 [°C]	21.6 $\pm$ 0.2	23.1 $\pm$ 0.2	25.1 $\pm$ 0.1	29.7 $\pm$ 0.1

Table 4.8: Thermo-Hydraulic Test Sessions Results - 2.

Results	**#Test -TH Test Session 2**			**#Test - TH Test Session 3**
	#3-TH2	#5-TH2	#6-TH2	#1-TH3
Flowrate [l/min]	200	100	300	300
Flowrate Error [l/min]	$\pm$ 4.3	$\pm$ 3.8	$\pm$ 4.8	$\pm$ 4.8
Peak Heat Flux [kW/m^2]	502	500	702	500
Radiometer Err [kW/m^2]	$\pm$ 15	$\pm$ 15	$\pm$ 21	$\pm$ 15
TCs Error [°C]	$\pm$ 1.5	$\pm$ 1.5	$\pm$ 1.5	$\pm$ 1.5
TK-01 [°C]	188 $\pm$ 1.3	262 $\pm$ 2.7	202 $\pm$ 1.5	151 $\pm$ 6.2
TK-02 [°C]	170 $\pm$ 1.3	246 $\pm$ 2.1	176 $\pm$ 2.0	132 $\pm$ 4.5
TK-03 [°C]	170 $\pm$ 1.4	243 $\pm$ 2.4	177 $\pm$ 1.9	134 $\pm$ 5.1
TK-05 [°C]	188 $\pm$ 1.7	261 $\pm$ 3.1	202 $\pm$ 3.2	151 $\pm$ 6.0
TK-06 [°C]	182 $\pm$ 1.5	253 $\pm$ 3.6	192 $\pm$ 2.9	Error
TK-07 [°C]	184 $\pm$ 1.3	258 $\pm$ 3.2	197 $\pm$ 2.5	148 $\pm$ 5.1
TK-08 [°C]	37.6 $\pm$ 5.8	210 $\pm$ 2.8	151 $\pm$ 2.9	127 $\pm$ 3.8
TK-09 [°C]	152 $\pm$ 1.5	227 $\pm$ 3.1	152 $\pm$ 2.0	116 $\pm$ 3.9
TK-10 [°C]	151 $\pm$ 2.3	224 $\pm$ 3.1	150 $\pm$ 2.3	115 $\pm$ 1.9
TK-12 [°C]	133 $\pm$ 1.1	198 $\pm$ 3.8	131 $\pm$ 2.6	101 $\pm$ 2.1
TK-13 [°C]	32.6 $\pm$ 1.4	35.6 $\pm$ 0.4	34.5 $\pm$ 1.5	31.0 $\pm$ 0.4

Table 4.9: Thermo-Hydraulic Test Sessions Results - 3.

Results	**#Test -TH Test Session 4**	**#Test - TH Test Session 5**		
	#2-TH4	#1-TH5	#2-TH5	#3-TH5
Flowrate [l/min]	300	200	200	200
Flowrate Error [l/min]	$\pm$ 4.8	$\pm$ 4.3	$\pm$ 4.3	$\pm$ 4.3
Peak Heat Flux [kW/m^2]	298	299	727	102
Radiometer Err [kW/m^2]	$\pm$ 9.0	$\pm$ 9.0	$\pm$ 22	$\pm$ 3.1
TCs Error [°C]	$\pm$ 1.5	$\pm$ 1.5	$\pm$ 1.5	$\pm$ 1.5
TK-01 [°C]	102 $\pm$ 1.4	125 $\pm$ 1.2	266 $\pm$ 4.0	60.4 $\pm$ 0.6
TK-02 [°C]	90.1 $\pm$ 0.6	114 $\pm$ 1.3	239 $\pm$ 3.1	56.3 $\pm$ 0.5
TK-03 [°C]	91.8 $\pm$ 1.1	114 $\pm$ 0.9	239 $\pm$ 3.4	56.5 $\pm$ 0.6
TK-05 [°C]	102 $\pm$ 1.3	125 $\pm$ 1.0	265 $\pm$ 3.6	60.2 $\pm$ 0.8
TK-06 [°C]	Error	113 $\pm$ 16	252 $\pm$ 49	Error
TK-07 [°C]	98.7 $\pm$ 2.3	122 $\pm$ 1.1	260 $\pm$ 3.7	59.3 $\pm$ 0.5
TK-08 [°C]	98.4 $\pm$ 0.9	47.9 $\pm$ 0.5	79.0 $\pm$ 1.0	37.4 $\pm$ 0.2
TK-09 [°C]	79.1 $\pm$ 0.7	101 $\pm$ 2.1	211 $\pm$ 3.3	52.2 $\pm$ 0.5
TK-10 [°C]	79.1 $\pm$ 0.8	102 $\pm$ 1.1	209 $\pm$ 1.9	53.0 $\pm$ 0.6
TK-12 [°C]	70.1 $\pm$ 0.8	90.8 $\pm$ 2.0	184 $\pm$ 2.4	49.2 $\pm$ 0.6
TK-13 [°C]	27.3 $\pm$ 0.3	28.4 $\pm$ 0.3	34.7 $\pm$ 0.5	29.4 $\pm$ 0.2

- Test Session Issues

It is, indeed, quite common to have some issues when using several measuring instruments like thermocouples are. Some of them were, in fact, malfunctioning during certain periods of time as it is hereby reported in Figure 4.41 and 4.42.

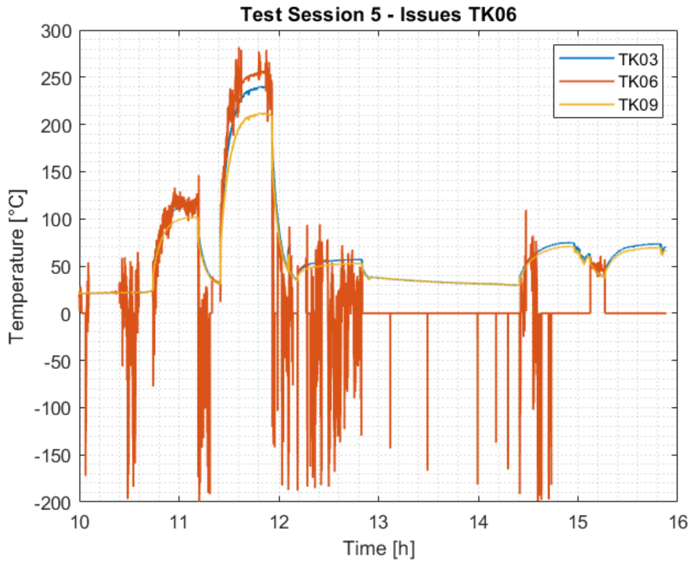

Figure 4.41: Issues on TK06.

TC #6 was experiencing some malfunctioning readings throughout the entire test session #5, which is shown in Figure 4.41 as an example where it is compared with the readings of TC #3 and TC #9 which are the two TCs adjacent to it, and also during test session #3. Apparently no others problem were found with this thermocouple during the other test sessions.

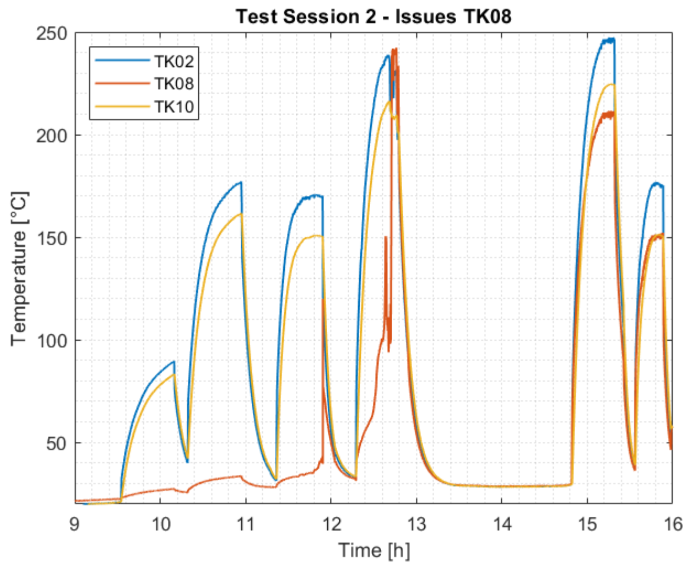

Figure 4.42: Issues on TK08.

TC #8 was experiencing some malfunctioning readings throughout the entire test session #1 and #5. During test session #2,instead, TC #8 seemed to start working for no apparent reason at the middle of the testing day. As an example its behaviour during test session #2 is shown in Figure 4.42 where it is compared with the readings of TC #2 and TC #10 which are symmetric thermocouple (see Figure 4.12) and the outlet thermocouple, respectively. The thermocouple is considered to do not work properly as its temperature readings were much lower than the other TCs readings, specifically even lower than the outlet air temperature read by TC #10.

Apparently no others problem were found with this thermocouple during the test session #3 and #4.

5. Validation of the Computational Model

The overall objective of this chapter is to demonstrate the accuracy of CFD model so that it might be used with confidence for other simulations and that the results can be considered credible for decision making in the design of an entire porous tubular cavity receiver with RRs used as a heat transfer matrix.
Hence, the validation assessment determines if the computational simulations agree with the physical reality, i.e. the experimental results. Therefore, once the computed and experimental results are collected, the science in the models has to be examined through a comparison between the two types of data.
Said comparison is carried out in the following Section 5.2.

5.1 Comparison between the Measured and Computed Hydraulic Characteristic

Both computational and experimental pure hydraulic results are examined throughout this entire work. Final CFD results are already presented in Figure 3.28 (see 3.1, Chapter 2), where the computed values are shown together with a fit curve which also gives a general trend pattern with a coefficient of determination R^2 of 91.5%. Such coefficient is taken into account by representing an uncertainty area around the trend curve equal to 8.5% of the actual pressure value in each point of the fit curve. Computed values that together with their own error bar fall into this uncertainty area are considered to be acceptably reliable results.
Final experimental results are, instead, already presented in Figure 4.35 (see 4.6.1, Chapter 4), where the net processed values (the ones with the minor and major pressure losses taken into account) are shown together with a fit curve which also gives a general trend pattern with a coefficient of determination R^2 of 80%. Such coefficient is taken into account by representing an uncertainty area around the trend curve equal to 20% of the actual pressure value in each point of the fit curve. It is, indeed, quite expected that such R^2 values is smaller in the case of the experimental results as more uncertainty is associated to their collection at the PSA facility due to the degrees of error of the field instrumentation. Computed values that together with their own error bar fall into this uncertainty area are considered to be acceptably reliable results.
The two aforementioned computed and experimental results are compared and shown together in the following Figure 5.1 below.
In Figure 5.1 only the uncertainty coefficient of determination R^2 area of the experimental results is represented in light blue together with its trend curve, whereas the CFD trend curve is not shown as

computed results are instead.
Computed results only have a vertical error bar as the flowrate is a model input and therefore contains no error. That CFD error is due to the grid choice of 2.4 million cells and to the RRs block random pattern independence check (see 2.2.1 and C).
Experimental results, instead, are not shown in order to make a cleaner and easier to understand plot.
A good understanding of the mock-up geometry plays a fundamental role when comparing the two pure hydraulic pressure drop results. Specifically, the real mock-up has two grids at the beginning and ending part of the RRs block which were used to held and contain the Raschig Rings during the designing and manufacturing of the sample. The CFD mock-up geometry, instead, does not contain such two grids which bring a supplementary minor pressure drop across the RRs block. This pressure drop difference between the two curves which should be small at low flowrate is expected to be higher and therefore highlighted when looking at the higher flowrate tests. This expected behaviour could be noticed, for example, as the CFD computed point always fall below the experimental PSA trend curve as shown in Figure 5.1. Finally experimental and numerical results seem to have a very good match between each other as they all fall within the two uncertainty areas. In particular, every red value (computed data) intersect fall within the light blu R^2 uncertainty area of the experimental data. Such a good match provides, indeed, a validation of the computed model since it resembles and represents accurately enough, within the error ranges provided, the physical reality of the problem.

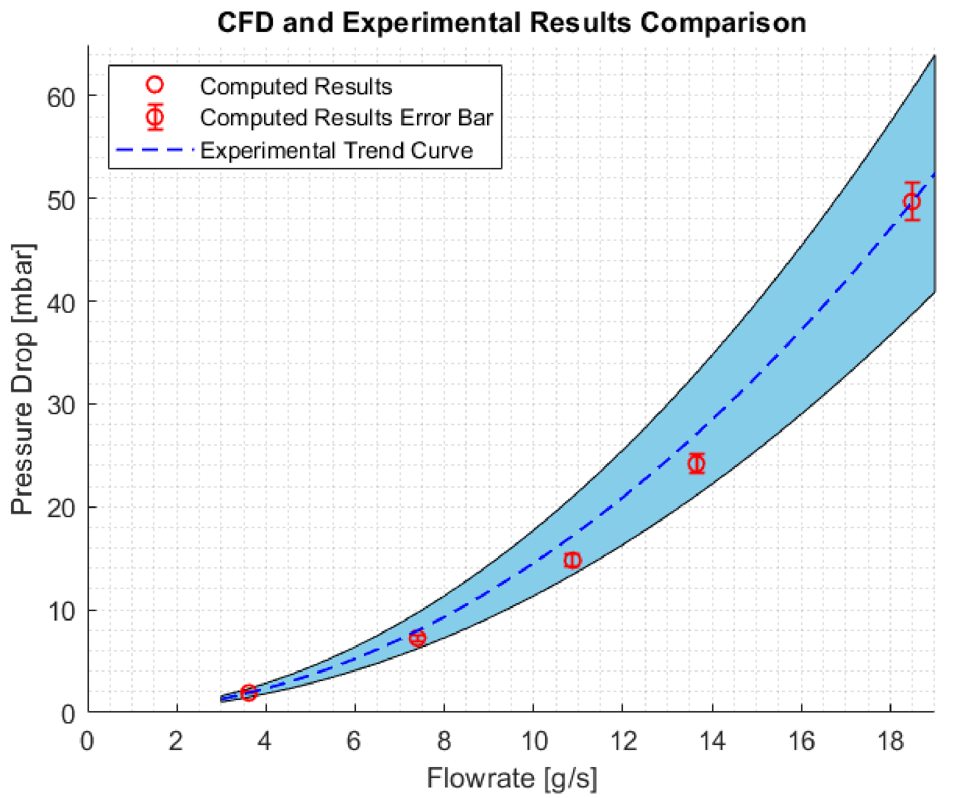

Figure 5.1: Comparison between computed (open symbols) and experimental (dashed line) results: the light blue area represented above is the R^2 Experimental Trend Curve Uncertainty Area.

The positive outcome of the comparison between the CFD and experimental pure hydraulic air mock-up pressure drop results, discussed in the previous Section 5.2, lead to a successful validation of the CFD air model.

Since results of the air case study are considered to be reliable as the validation is confirmed, aforementioned results can be processed together with the previously obtained water case study ones, see [24], to make a hydraulic characteristic of the RRs Mock-up in terms of adimentional numbers so that it does not depend on the utilized fluid properties but only on the geometry of the sample.
The adopted methodology is to consider the pressure drop as if it were only caused by major pressure losses (see 4.6.1) estimating an overall global friction factor which also includes and considers losses across the Raschig Rings block. Indeed, this friction factor is calculated using Equation 4.3 by taking into account the total net pressure drop across the entire mock-up. For simplicity reasons, the localized minor pressure drop due to the smooth cross section increase and decrease before and after the RRs block is included into said global friction factor.
Inputs of the Equation 4.3 are:

- Operating pressure P = 9.5 bar;
- Air density of 11.2 kg/m^3;
- Water density of 997 kg/m^3;
- Air viscosity of 1.83 $\cdot 10^{-5}$ Pa s;
- Water viscosity of 1.05 $\cdot 10^{-3}$ Pa s;
- Mock-up internal diameter of 15 mm;
- Mock-up total length of 84 mm;
- Air computed and experimental mock-up net pressure drop trend curves, Equations 3.3 and 4.5 respectively;
- Water experimental mock-up net pressure drop trend curve, Equation 5.1 shown below [24];

$$Y = 0.0024 \cdot X^2 \quad R^2 = 88\% \tag{5.1}$$

- Various air and water flowrates within the experimental tests range;

Trend curves are preferred to be used as input rather than CFD and experimental pressure drops results in order to get nicer and smoother lines to plot. Uncertainties of each curve is considered by assuming a simple linear dependence between the R^2 trend curve error, differential pressure transmitter error and flowrate error. These errors that amount to, 13%, 24% and 12.2% for the water AREVA (2017) tests, PSA (2019) tests and CFD computed results, respectively, are represented by means of errorbars into the bar plot.
The hydraulic characteristic of the RRs Mock-up, i.e. aforementioned global friction factor, is expected to be a constant value. In fact, the investigated Reynolds (Re) range is quite small, going from an order of 10^4 to a maximum of 10^5 for the air case or 10^6 for the water one. Together with a small Reynolds range it also has to be considered that the RRs porous matrix, which increases and improves by a lot the turbulence of the air fluid, brings the entire motion field to a complete turbulence state where the friction factor starts to become a constant value and does not depend anymore on the

Reynolds number. The higher the roughness of the pipe, the smaller is the value of the Re number where this phenomenon takes place. Therefore, the investigated Reynolds range is expected to be high enough, considering the only major pressure loss assumption made above, for aforementioned phenomenon to happen
The results post-processed into the hydraulic characteristic of the mock-up are shown in Figure 5.2 below.

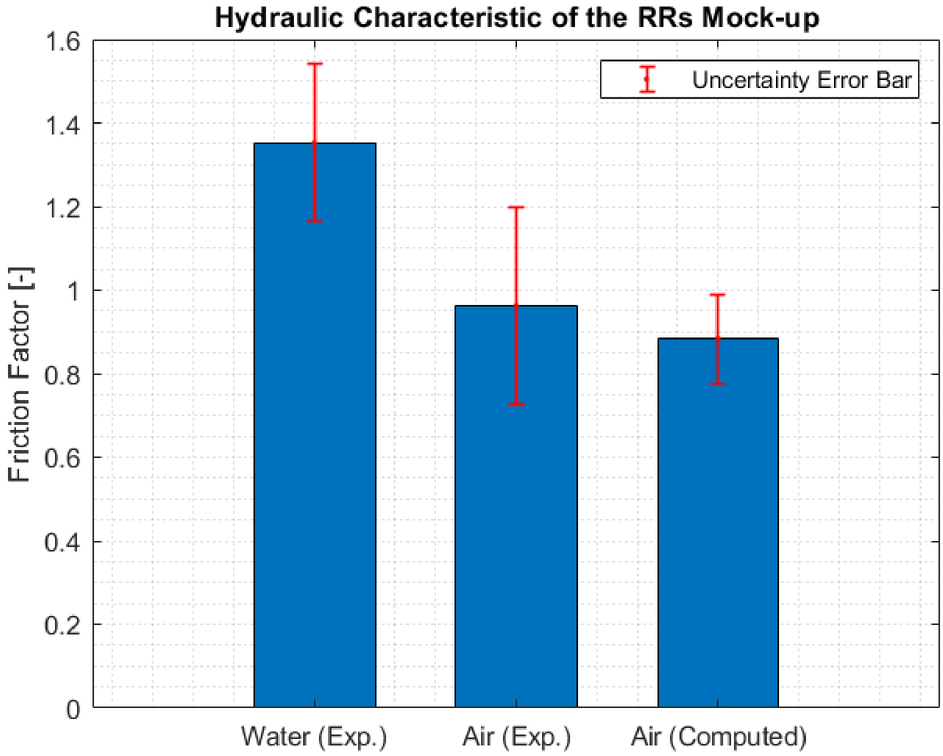

Figure 5.2: Hydraulic Characteristic of the Mock-up.

Results shown in the Figure above are promising as the values follow a behaviours expected by the physical reality. Indeed, as explained above, the friction factor is constant with the increase of the Reynolds number after surpassing the so called complete turbulence region. The absolute values of the friction factor are quite high, for instance an order of magnitude higher than what can be usually found into the Moody chart; this is due to the assumption that all pressure losses, such as minor localized pressure drops, are included into this general friction factor for simplicity. An average almost constant value of 1.1 for high Reynolds numbers is reasonable if considered that the working fluid is passing through a porous media which main drawback is the pressure drop across it.
CFD computed friction factor pattern gives a bit smaller values since, as explained in the previous Section 5.2, the two grids before and after the Raschig Rings block, which cause another additional localized pressure drop, are not considered inside the computed geometry.
On the other hand experimental results give a sligthy higher values as the pressure drop was not collected right at the inlet and outlet of the RRs mock-up. Additionally, its error bar does not contain any information about the measuring instrumentation uncertainty as it was not provided or reported into the official documents of that previous experimental campaign.

Overall results seem to be reasonably acceptable within the provided errors as each one of all of the three curves has an error bar that intersect at least one of the error bars of the other curves, specifically the PSA values, which are in the middle between the computed and the AREVA ones, intersects both the other two.

5.2 Comparison between the Measured and Computed Thermal Characteristic

Thermo-hydraulic exerimental results have been collected, examined and processed throughout this work, see 4.6.2. However, the outcome of the computational model, illustrated in Chapter 3, cannot be compared, at this current stage, to the above-said experimental results.
Thermo-hydraulic computed results are, in fact, an initial attempt to determine the Thermal Characteristic of the RRs mock-up as they have been used as a guide line to be followed during the two weeks experimental campaign at the SF-60 in order to avoid any possible dangerous temperature or operating condition.
Further investigations on the RRs mock-up will be carried out in the next future. The main intent is to make a complete calorimetric analysis to be based on the already collected thermo-hydraulic experimental results in order to modify the thermo-hydraulic computational model accordingly.
Then, the computed data will be compared to the experimental ones. This could possibly validate the model if a good match is found, between the two results, within the provided error.
With the eventual validation of this additional model and confirmation of the validity of the results obtained, this study could be used as a base starting line to design and implement this here-investigated technology in a new CSP receiver of the tubular kind.

6. Conclusions and perspective

The investigation of the exploitability of Raschig Rings as a heat transfer matrix for Concentrated Solar Power applications has been carried out here both numerically and experimentally at the PSA Solar Furnace SF-60.

The test campaign has been carefully designed based on the outcome of a CFD model, suitably developed to account for a suitable geometry, operating pressure, working fluid characteristics and all of the thermo-hydraulic properties of the mock-up as well as its safe maximum temperature of 400°C. Tests have been carried out by using both the flow-rate (ranging from 25 l/min up to 400 l/min) and the solar peak heat flux (ranging from 100 kW/m^2 up to 700 kW/m^2) as parameters, one at a time.

The experimental campaign has been carried out from September 9^{th} to September 20^{th} 2019 during which experimental data of both the pure and thermo-hydraulic characteristic of the RRs Mock-up have been collected, despite the occurred bad weather conditions.

The validation of the pure hydraulic CFD model of the mock-up, equipped with Raschig Rings (RRs) and air as working fluid, has been performed with a comparison to the available results of the experimental campaign carried out at the SF-60 facility, in the Plataforma Solar de Almeria.
The pure hydraulic results are promising, showing a very good match within the provided error bar and a quadratic dependency of the pressure loss on the flow-rate as expected by the theory of the physical phenomenon. The post processing of the experimental results of the previously investigated water case together with the ones of the new air study, have been resumed into a hydraulic characteristic which highlights an average global friction factor of 1.15. This value, which might seem high, is indeed a very reasonable number considering the assumption made and that the mock-up contains a porous matrix. A good match is also achieved here, within the provided uncertainty.

The here presented CFD model could be further developed by means of a calorimetric study to be based onto the thermal experimental data already collected at the SF-60. An energy balance on above-said data, together with the estimation of an absorption coefficient and emissivity of the mock-up could be executed in the next future. This additional analysis could lead to a possible validation of the thermo-hydraulic computed model against the experimental data if a good match is found, within the provided error bar, between the two.
With the eventual validation of this additional thermo-hydraulic model and confirmation of the validity of the results obtained, this study could be used as a base starting line to design and implement

this here-investigated technology in a new CSP receiver of the tubular kind.

References

[1] SolarPACES. How csp works, 2017. https://www.solarpaces.org/csp-technologies/csp-how-it-worksph.

[2] European Commission. Strategic energy technologies information system: Concentrated solar power, 2019. https://setis.ec.europa.eu/technologies/concentrated-solar-energy.

[3] Ranga Pitchumani Joseph Stekli, Levi Irwin. Technical challenges and opportunities for concentrating solar power with thermal energy storage. *ASME The American Society of Mechanical Engineers*, 2013.

[4] European Commission. Smart specialization platform: Concentrated solar power, 2018. https://s3platform.jrc.ec.europa.eu/hu/concentrated-solar-power.

[5] W. Stein Csiro K. Lovegrove. Introduction to concentrating solar power (csp) technology. *ScienceDirect*, 2012.

[6] Solar Energy Industries Association. Concentrating solar power, 2019. https://www.seia.org/initiatives/concentrating-solar-power.

[7] Franz Trieb, Christoph Schillings, Marlene O'sullivan, Thomas Pregger, and Carsten Hoyer-Klick. Global potential of concentrating solar power. In *SolarPACES Conference*, pages 15–18, 2009.

[8] NASA. Surface meteorology and solar energy, 2008. http://eosweb.larc.nasa.gov/sse/.

[9] REN21. Renewables 2014: Global status report, 2014.

[10] REN21. Concentrated solar power increasing cumulative global capacity more than 11% to just under 5.5 gw in 2018), 2019. https://www.evwind.es/2019/06/18/concentrated-solar-power-increasing-cumulative-global-capacity-more-than-11-to-just-under-5-5-gw-in-2018/67630.

[11] Seyed Mehdi Mohaghegh. Csp vs pv – understanding the current situation and future outlook. *ResearchGate*, 2015.

[12] HELIOSCSP. Current status of concentrated solar power (csp) globally, 2017. http://helioscsp.com/current-status-of-concentrated-solar-power-csp-globally/.

[13] CORDIS European Commission. Final report - solhyco (solar-hybrid power and cogeneration plants), 2011. https://cordis.europa.eu/publication/rcn/13318_en.html.

[14] O. Faugeroux G. Olald A. Boubault, B. Claudet. Accelerated aging of a solar absorber material subjected to highly concentrated solar flux. *ResearchGate*, 2014.

[15] F. Stucker P. Pozivil, N. Ettlin and A. Steinfeld.

[16] Zhang-Jing Zheng, Ming-Jia Li, and Ya-Ling He. Thermal analysis of solar central receiver tube with porous inserts and non-uniform heat flux. *Applied Energy*, 185:1152–1161, 2017.

[17] MA Al-Nimr and MK Alkam. Unsteady non-darcian forced convection analysis in an annulus partially filled with a porous material. *Journal of Heat Transfer*, 119(4):799–804, 1997.

[18] MK Alkam and MA Al-Nimr. Improving the performance of double-pipe heat exchangers by using porous substrates. *International Journal of Heat and Mass Transfer*, 42(19):3609–3618, 1999.

[19] AA Mohamad. Heat transfer enhancements in heat exchangers fitted with porous media part i: constant wall temperature. *International Journal of Thermal Sciences*, 42(4):385–395, 2003.

[20] K Ichimiya. A new method for evaluation of heat transfer between solid material and fluid in a porous medium. *Journal of heat transfer*, 121(4):978–983, 1999.

[21] HL Fu, KC Leong, XY Huang, and CY Liu. An experimental study of heat transfer of a porous channel subjected to oscillating flow. *Journal of heat transfer*, 123(1):162–170, 2001.

[22] Devarakonda Angirasa. Experimental investigation of forced convection heat transfer augmentation with metallic fibrous materials. *International Journal of Heat and Mass Transfer*, 45(4):919–922, 2002.

[23] Abdulmajeed A.Mohamad Bogdan I.Pavel. An experimental and numerical study on heat transfer enhancement for gas heat exchangers fitted with porous media. *International Journal of Heat and Mass Transfer*, 47(23):4939–4952, 2004.

[24] L. Savoldi, A. Bertinetti, G.F. Nallo, A. Zappatore, R. Zanino, F. Cau, F. Cismondi, and Y. Rozier. Cfd analysis of different cooling options for a gyrotron cavity. *IEEE Transactions on Plasma Science*, 44(12):3432–3438, 2016.

[25] THALES Group. Report on thermal cavity mock-up experiments, 2017.

[26] S CD-adapco. *STAR CCM+ User Guide Version 13.02*, 2018.

[27] A. Bertinetti, F. Albajar, F. Cau, A. Leggieri, F. Legrand, E. Perial, G. Ritz, L. Savoldi, R. Zanino, and A. Zappatore. Design, test and analysis of a gyrotron cavity mock-up cooled using mini channels. *IEEE Transactions on Plasma Science*, 2018.

[28] Laura Savoldi. Experimental and simulation results on mock-ups equipped with raschig rings and mini-channels, 2017.

[29] Suhas V. Patankar. *Numerical Heat Transfer and Fluid Flow*. 1980.

[30] Engineer ToolBox. Convective heat transfer, 2003. https://www.engineeringtoolbox.com/convective-heat-transfer-d_430.html.

[31] DLR Institute of Solar Research. Ciemat plataforma solar de almería - europe's biggest test center for concentrating solar power (csp), 2003. https://www.dlr.de/sf/en/desktopdefault.aspx/tabid-7176/11942_read-28189/.

[32] CIEMAT. Psa: Largest european research centre devoted to concentrating solar energy. https://www.psa.es/es/instalaciones/pdf/Folleto%20PSA%202013_EN_131202.pdf.

[33] CIEMAT. Facilities, 2018. https://www.psa.es/en/facilities/index.php.

[34] Ricardo Sanchez Moreno. Official psa annual report 2016, 2016.

[35] J. Fernandez J. Rodriguez, I. Canadas and R. Monterreal. The psa solar furnace, a test facility ready to characterize high-concentration solar devices from solar thermal applications to pv cells. SolarPACES.

[36] D.J.Rossouw. *Application of Thermo-Fluidic Measurement Techniques*. 2016.

[37] ReoTemp Instruments. Thermocouple types, 2019.

[38] ProcessParameters. Thermocouple types and ranges, 2019.

[39] DOLSAT Consult. Principiile senzorilor de temperatură, 2019. https://sites.google.com/site/sistemedaq/measurement-fundamentals-main-page/traductoare/2-measuring-temperature-with-thermocouples-rtds-or-thermistors/principiile-senzorilor-de-temperatura?tmpl=%2Fsystem%2Fapp%2Ftemplates%2Fprint%2FshowPrintDialog=1.

[40] MI Roldán and R Monterreal. Heat flux and temperature prediction on a volumetric receiver installed in a solar furnace. *Applied energy*, 120:65–74, 2014.

[41] J Ballestrín and R Monterreal. Hybrid heat flux measurement system for solar central receiver evaluation. *Energy*, 29(5-6):915–924, 2004.

[42] Federica Tarasco. Numerical evaluation of thermal fatigue lifetime of air-cooled tubular receivers for csp plants. Master's thesis, Politecnico di Torino, 2017.

[43] VATTEL Corporation. Use of the thermogage circular foil heat flux gauge. http://vatell.com/vatellwebfiles/Use%20of%20Thermogage%20v2.pdf.

[44] J Ballestrın, S Ulmer, A Morales, A Barnes, LW Langley, and M Rodrıguez. Systematic error in the measurement of very high solar irradiance. *Solar energy materials and solar cells*, 80(3):375–381, 2003.

[45] Bronkhorst. *Mass Flow Controller for Gases*.

[46] Glenn Rager. How do differential pressure sensors work and what are they used for?, 2016. https://www.quora.com/How-do-differential-pressure-sensors-work-and-what-are-they-used-for.

[47] APLISEN. *Differential Pressure Transmitter PRE-28*.

[48] BR Munson, DF Young, and TH Okiishi. Fundamentals of fluid mechanics, 1998.

[49] Neutrium. Absolute roughness of pipe material, 2012. https://neutrium.net/fluid_flow/absolute-roughness/.

[50] Laura Savoldi. Support in the design and analysis of the gyrotron full-size cavity and mock-ups. 2015.

[51] A. Bertinetti. *Development of the Multi-physiCs tool for the integrated simulation of the Cavity and its application for the design of gyrotron cavities for thermo-nuclear applications*. PhD thesis, Politecnico di Torino, 2019.

[52] Hiroyuki Abe and Robert Anthony Antonia. Turbulent prandtl number in a channel flow for pr= 0.025 and 0.71. In *TSFP DIGITAL LIBRARY ONLINE*. Begel House Inc., 2009.

A. Appendix

Material Properties

The temperature dependence of the material properties such as density (ρ), thermal conductivity (k) and specific heat (c_p) of the Glidcop® copper alloy is taken into account in both pure hydraulic and thermo-hydraulic simulations based on the following polynomial functions of the temperature (T) [50]:

$$\rho = 8872 - 0.4563 \cdot T - 8.704E^{-5} \cdot T^2 \quad [kg/m^3] \tag{A.1}$$

$$k = 368.2 - 0.2612 \cdot T + 3.070E^{-4} \cdot T^2 \quad [W/°Cm] \tag{A.2}$$

$$c_p = 383.4 + 0.1413 \cdot T - 2.979E^{-5} \cdot T^2 \quad [J/°Ckg] \tag{A.3}$$

The above Glidcop® polynomial function properties, to be used with a temperature in [°C], are shown below in Figure A.1, A.2 and A.3 respectively.

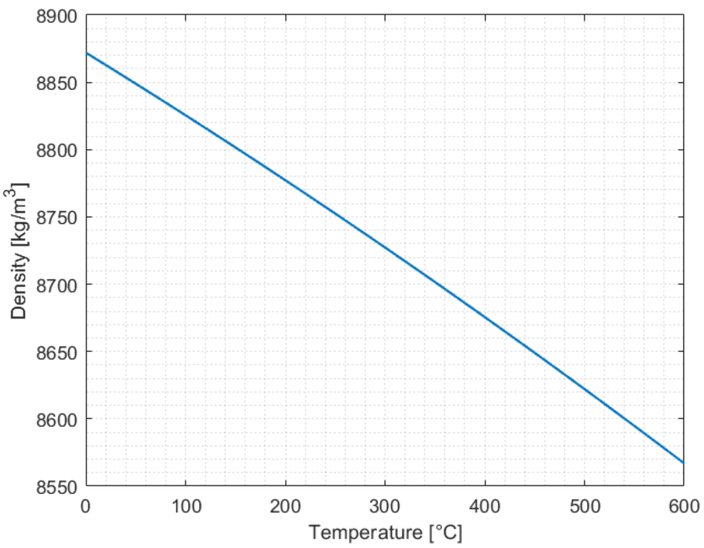

Figure A.1: Glidcop® Density polynomial function of the Temperature.

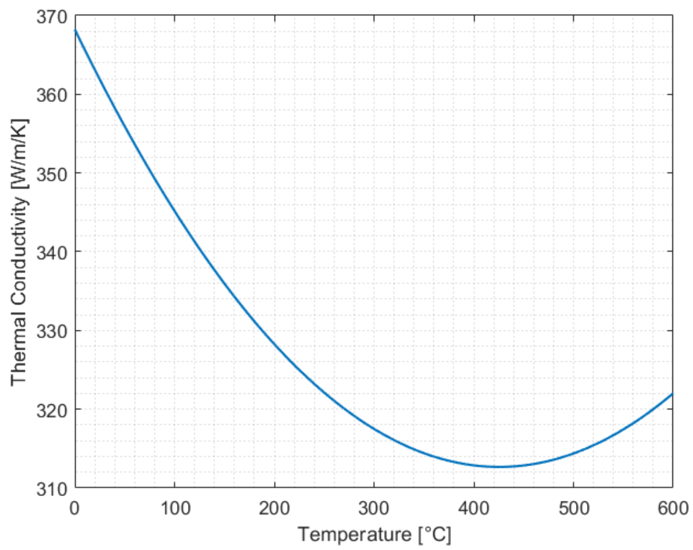

Figure A.2: Glidcop® Thermal Conductivity polynomial function of the Temperature.

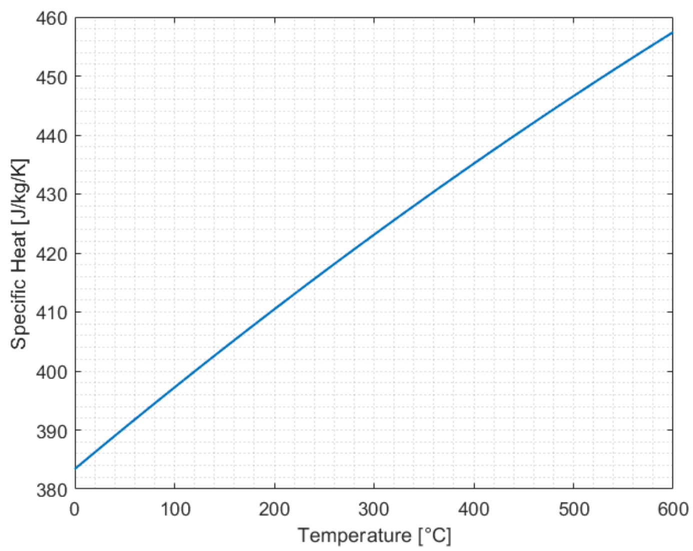

Figure A.3: Glidcop® Specific Heat polynomial function of the Temperature.

The thermal conductivity of the RRs block is, however, different and much higher than the values shown in Figure A.2. The following Equation A.4 [51] shows the adopted value for aforementioned block:

$$k_{RRs} = 2600 \quad [W/mK] \tag{A.4}$$

The following constant molecular weight (W_{air}) and the turbulent Prandtl number (Pr_{air}) [52] are chosen for the simulation of the air:

$$W_{air} = 28.97 \quad [kg/kmol] \tag{A.5}$$

$$Pr_{air} = 0.9 \tag{A.6}$$

The temperature dependence of the material properties such as thermal conductivity (k_{air}), specific heat ($c_{p,air}$) and dynamic viscosity (μ_{air}) of the air is also taken into account in both pure hydraulic and thermo-hydraulic simulations based on the following polynomial functions of the temperature (T):

$$k_{air} = 0.0013 + 9.280E^{-5} \cdot T - 3.301E^{-8} \cdot T^2 + 6.520E^{-12} \cdot T^3 \quad [W/mK] \tag{A.7}$$

$$cp_{air} = 1043 - 0.3660 \cdot T + 9.700E^{-4} \cdot T^2 - 6.595E^{-7} \cdot T^3 + 1.460E^{-10} \cdot T^4 \quad [J/kg/K] \tag{A.8}$$

$$mu_{air} = 3.830E^{-6} + 5.578E^{-8} \cdot T - 2.294E^{-11} \cdot T^2 + 4.935E^{-15} \cdot T^3 \quad [Pa \cdot s] \tag{A.9}$$

The above air polynomial function properties, to be used with a temperature in [K], are shown below in Figure A.4, Figure A.5 and Figure A.6 respectively.

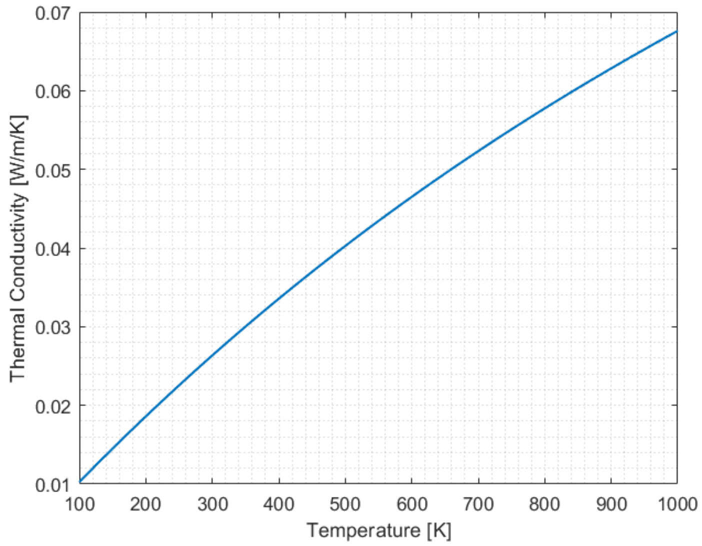

Figure A.4: Air Thermal Conductivity polynomial function of the Temperature.

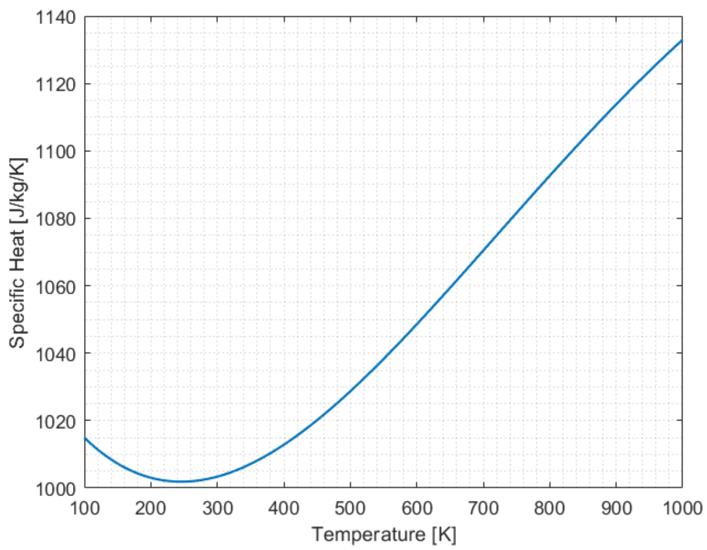

Figure A.5: Air Specific Heat polynomial function of the Temperature.

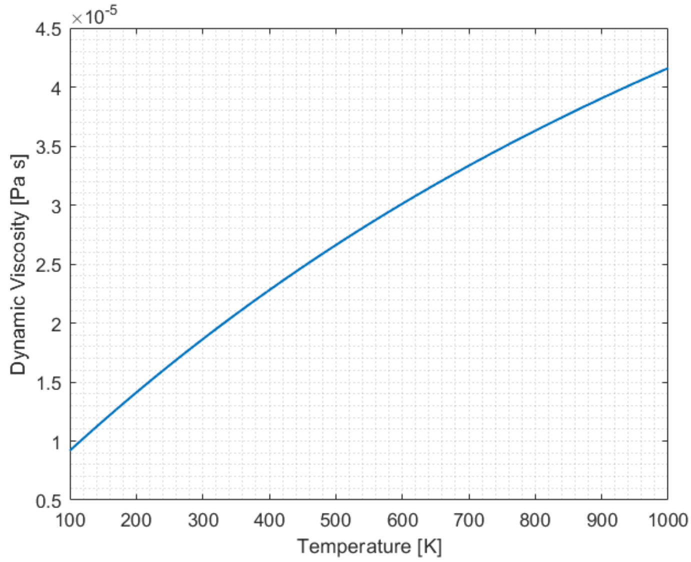

Figure A.6: Air Dynamic Viscosity polynomial function of the Temperature.

There is no polynomial function shown above for the air density as it is not needed to describe it since an ideal gas model is chosen for the fluid, see 2.1.2. Therefore, the air density is evaluated according to the pressure and temperature of the fluid itself.

B. Appendix

Mesh Independence

To make a good Mesh Independence various meshes have to be tested and their results compared. Furthermore, all of the models and boundary conditions of each simulation have to be kept the same in order to have a more significant comparison between results. Additionally, to make a relative error plot when lacking of some reference or literature values, results of the simulation with the finest mesh are considered to be the most precise ones and therefore the reference values for all of the other simulations results.
A synthesis of all of the details of the several tested meshes are reported below in Table B.1.
Note that BS stands for Base-Size and GR for Growth-Rate.

Table B.1: Tested meshes details.

No. of thousands of cells			**Mesh cell properties**			
Total	Fluid	Solid	Nominal BS	External Blocks BS	RRs Block BS	Surface GR
1271	679	592	1.2 $[mm]$	1.0 $[mm]$	0.8 $[mm]$	1.3
1509	797	712	1.1 $[mm]$	0.9 $[mm]$	0.7 $[mm]$	1.3
1906	993	913	1.0 $[mm]$	0.8 $[mm]$	0.6 $[mm]$	1.3
2421	1236	1185	0.9 $[mm]$	0.7 $[mm]$	0.5 $[mm]$	1.3
3538	1795	1742	0.8 $[mm]$	0.6 $[mm]$	0.4 $[mm]$	1.3
6067	3057	3010	0.7 $[mm]$	0.5 $[mm]$	0.3 $[mm]$	1.3

The Mesh Independence simulations, refer to the thermo-hydraulic problem since is it the more complex case between the two types of simulations run and therefore it is assumed that a valid mesh for the thermo-hydraulic case would also be valid for the pure hydraulic one.
Accordingly to what is listed in 2.2.2 (with exception made for the thermal heat losses which are not included), the following boundary conditions are applied:

- Inlet Mass Flow Rate - 500 lt/min;
- Outlet Pressure $P_{out} = 0$ bar;
- Flow Rate Inlet Temperature $T_{in} = 300K$;
- Gaussian Solar Heat Flux - Peak Flux $500kW/m^2$;
- no convective heat losses;
- no radiative heat losses;

The monitored variables considered to be significantly useful to be compared between the different simulations to assess a Mesh Independence are listed below:

1. Maximum Air Temperature - $T_{air,max}$;
2. Maximum Glidcop® Temperature - $T_{Glidcop,max}$;
3. Average Temperature of the Targeted Area - $T_{target,avg}$;
4. Average Temperature of the Glidcop® - $T_{Glidcop,avg}$;
5. Average Outlet Temperature of the Air - $T_{out,avg}$;
6. Maximum Velocity of the Air - $V_{air,max}$;
7. Average Velocity of the Outlet Air - $V_{out,avg}$;
8. Pressure Drop between Inlet and Outlet - P_{drop};

Maximum values are obtained by means of a STAR-CCM+ maximum function over the appropriate domain; average values are estimated with a STAR-CCM+ surface average function in the case of the targeted area and the Glidcop® temperatures while a mass-flow average function is used in the case of the outlet air temperature and outlet air velocity.
For each of the above variable both an absolute and relative grid independence are shown, specifically from Figure B.1 to Figure B.12.
All the obtained results shown in the previous Figures are hereby resumed, in a more compact solution, in Table B.2.

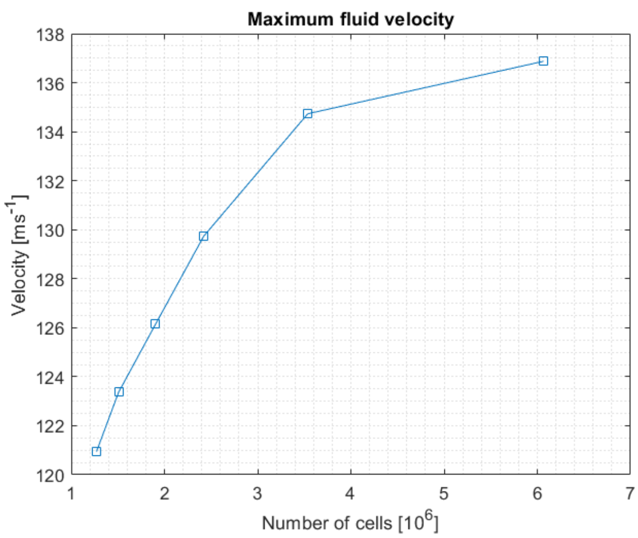

Figure B.1: Absolute Maximum Velocity of the fluid with different meshes.

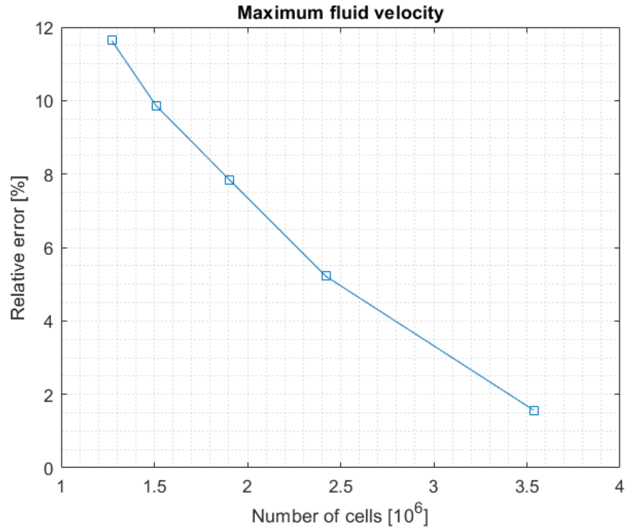

Figure B.2: Relative error of the Maximum Velocity of the fluid with different meshes.

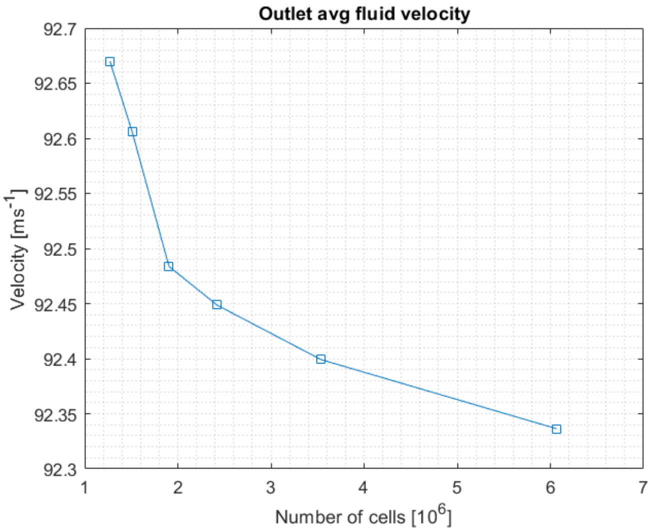

Figure B.3: Absolute Outlet Velocity of the fluid with different meshes.

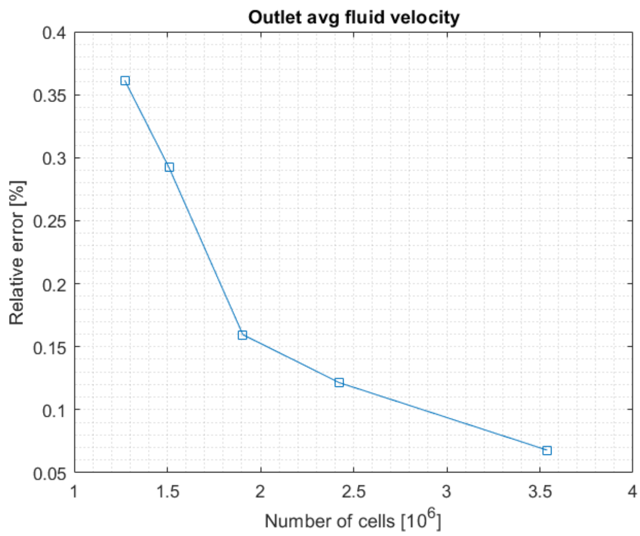

Figure B.4: Relative error of the Outlet Velocity of the fluid with different meshes.

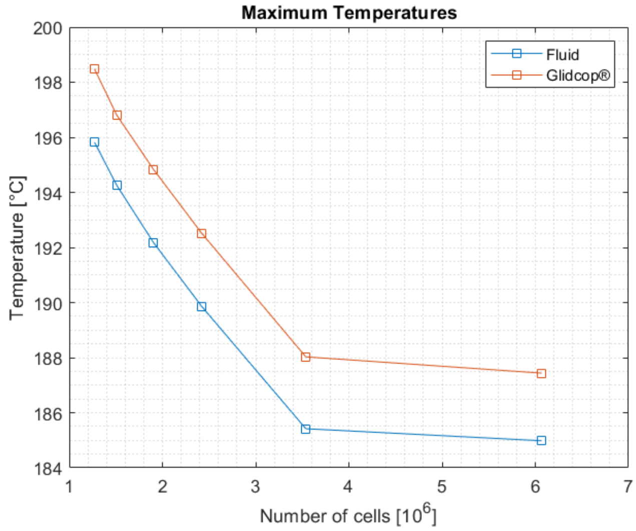

Figure B.5: Absolute Maximum Temperature of the Fluid and Glidcop® with different meshes.

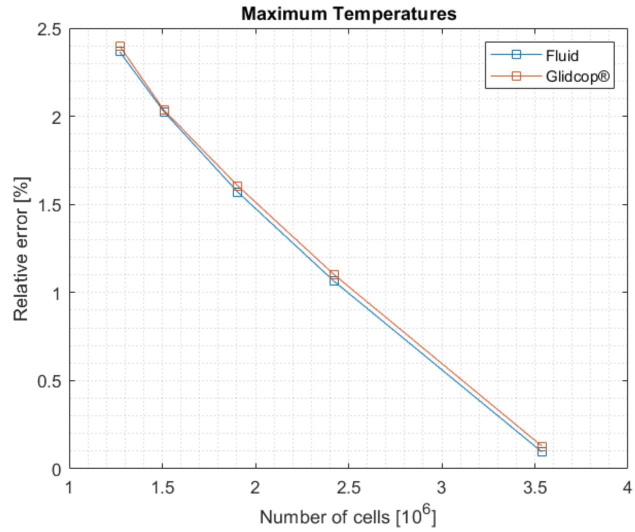

Figure B.6: Relative error, Maximum Temperature of the Fluid and Glidcop® with different meshes.

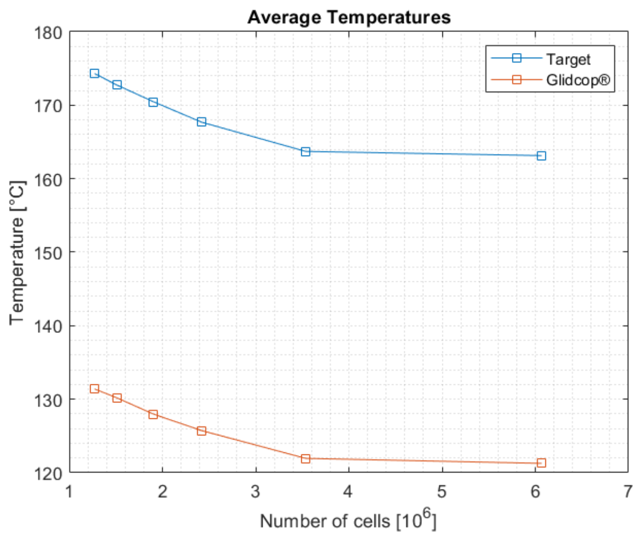

Figure B.7: Absolute Average Temperature of the Target and Glidcop® with different meshes.

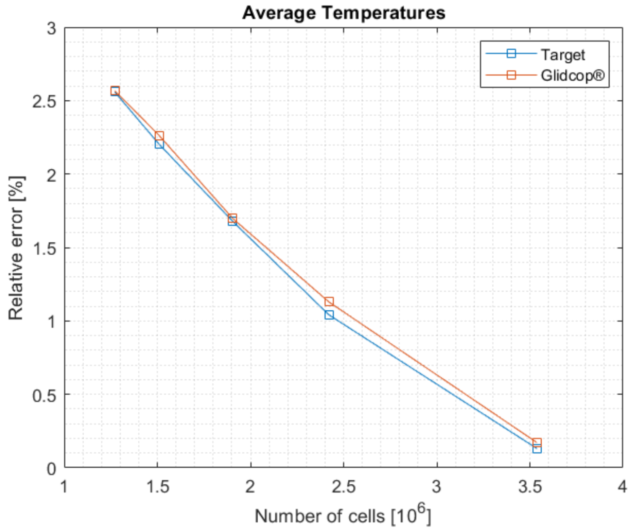

Figure B.8: Relative error, Average Temperature of the Target and Glidcop® with different meshes.

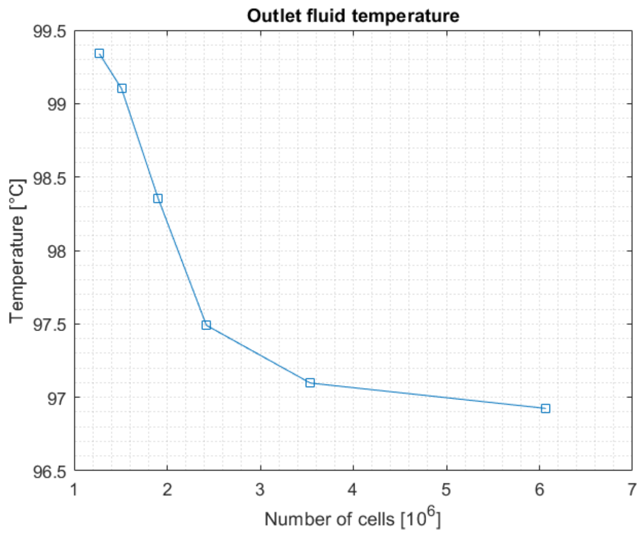

Figure B.9: Absolute Average Outlet Temperature of the fluid with different meshes.

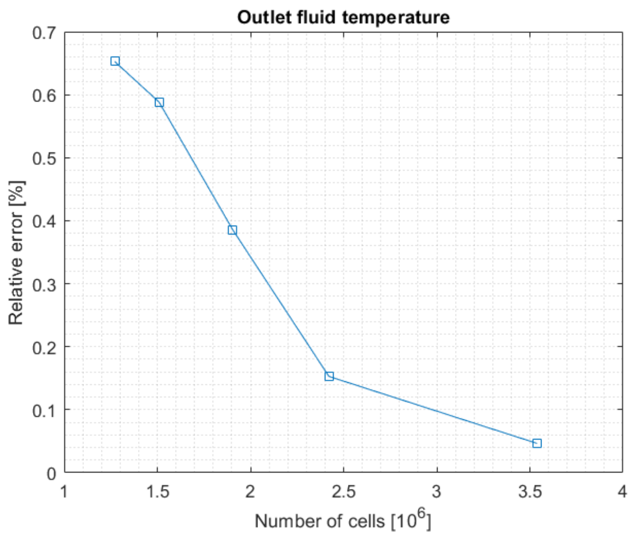

Figure B.10: Relative error of the Average Outlet Temperature of the fluid with different meshes.

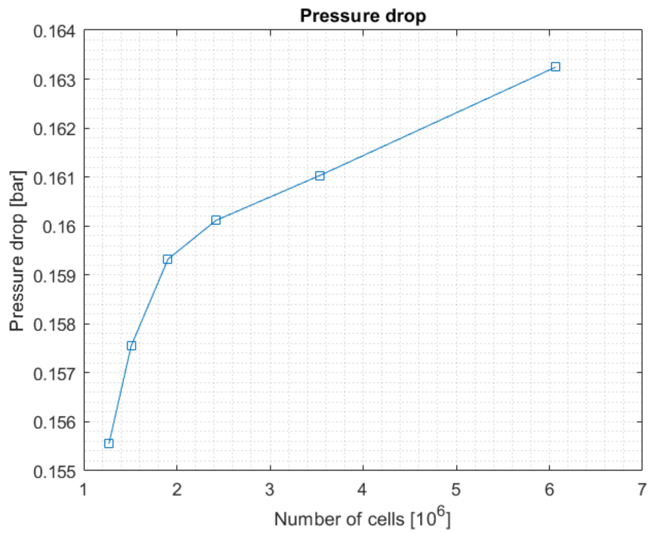

Figure B.11: Absolute Pressure Drop of the fluid with different meshes.

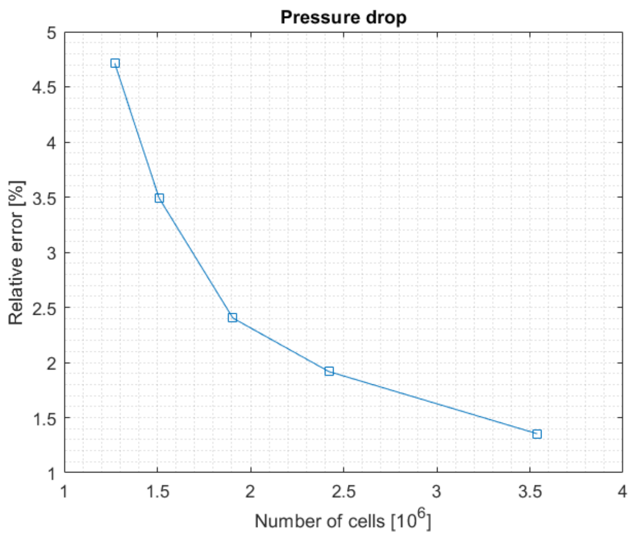

Figure B.12: Relative error of the Pressure Drop of the fluid with different meshes.

Table B.2: Mesh Independence analysis results.

Simulation Results	**No. of thousands of cells**					
	1271	**1509**	**1906**	**2421**	**3538**	**6067**
Maximum Air Velocity $[m/s]$	121.0	123.4	126.2	129.7	134.7	136.9
Average Outlet Air Velocity $[m/s]$	92.67	92.60	92.48	92.45	92.40	92.34
Maximum Air Temperature $[°C]$	195.8	194.3	192.2	189.9	185.4	185.0
Maximum Glidcop Temperature $[°C]$	198.5	196.8	194.8	192.5	188.0	187.4
Average Target Temperature $[°C]$	174.3	172.8	170.5	167.7	163.7	163.1
Average Glidcop Temperature $[°C]$	131.4	130.2	128.0	125.7	122.0	121.3
Average Outlet Air Temperature $[°C]$	99.34	99.10	98.35	97.49	97.10	96.92
Pressure Drop $[mbar]$	155.6	157.5	159.3	160.1	161.0	163.2
Rel. Err. Max. Air Velocity $[\%]$	11.6	9.86	7.83	5.22	1.56	-
Rel. Err. Avg. Outlet Air Velocity $[\%]$	0.36	0.29	0.16	0.12	0.07	-
Rel. Err. Max. Air Temperature $[\%]$	2.37	2.03	1.57	1.06	0.10	-
Rel Err. Max. Glidcop Temperature $[\%]$	2.40	2.03	1.60	1.11	0.13	-
Rel. Err. Avg. Target Temperature $[\%]$	2.56	2.20	1.68	1.04	0.13	-
Rel. Err. Avg. Glidcop Temperature $[\%]$	2.37	2.03	1.57	1.06	0.10	-
Rel. Err. Avg. Outlet Air Temperature $[\%]$	0.65	0.59	0.39	0.15	0.05	-
Rel. Err. Pressure Drop $[\%]$	4.71	3.49	2.40	1.92	1.35	-

As already explained, this Mesh Independence analysis is carried out to understand what is the best grid to adopt and use into the simulations. On one hand the more precise the results the better the mesh is, however computational cost and time needed per simulation is also another fundamental parameter to take into account. In this case the lower the better.

Among the different simulations tested, two meshes stand out as best candidates to be the optimal mesh: the 2.4 million cells and the 3.5 million cells mesh. The 6 millions cells mesh is not considered to be appropriated since almost the same results can be reached with the 3.5 million one saving several days of computation cost (almost up to 4 days saved per simulation).

One of the most significant values to look at in these cases is the relative error which shows how big the error is with each mesh, in particular both the 2.4 and 3.5 million cells meshes have low relative errors in all the investigated values.

C. Appendix

RRs Block Geometry Independence

In order to estimate what the error and the uncertainty of every value associated to the given geometry is, a different domain is tested by re-making the RRs block following the same procedure already described in 2.1.1. Since the algorithm is random it is expected to get different RRs blocks by remaking it and therefore different patterns and ways for the air fluid to follow while passing through the mock-up. The several simulations that have to be compared are run using the same boundary conditions as the ones used for the Grid Independence, see 2.2.1, and using the mesh considered to be the best one as discussed in 2.2.1. Simulations are run until almost the same residual is reached. The two RRs block are shown in Figure C.1 and C.2, respectively, while results of this analysis are hereby shown in Table C.1 and C.2:

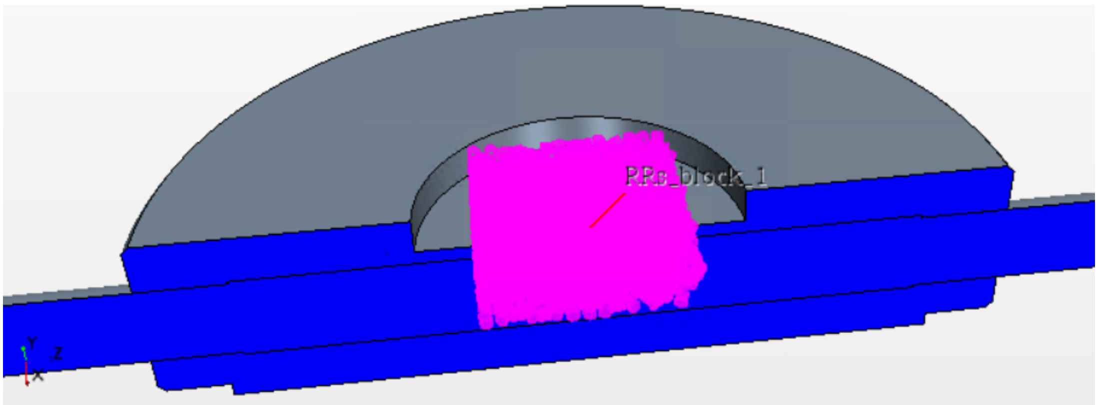

Figure C.1: Close up view of the RRs block #1.

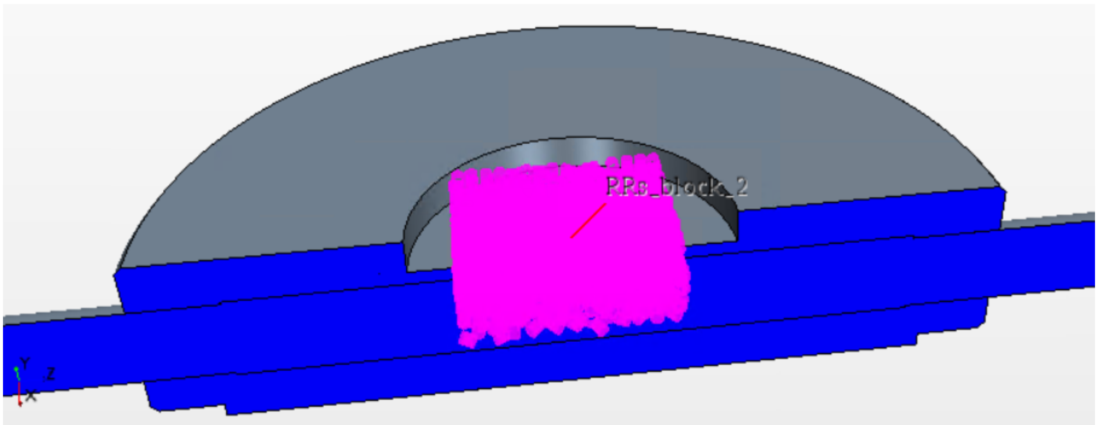

Figure C.2: Close up view of the RRs block #2.

Table C.1: RRs Block Geometry Independence - Results 1.

No. of RRs Block	**Avg. Outlet Air Velocity**		**Max. Air Velocity**	
Block #1	92.45 [ms^{-1}]	Relative Error	129.73 [ms^{-1}]	Relative Error
Block #2	92.55 [ms^{-1}]	0.10 %	127.47 [ms^{-1}]	1.75 %

Table C.2: RRs Block Geometry Independence - Results 2.

No. of RRs Block	**Avg. Outlet Air Temperature**		**Avg. Glidcop Temperature**	
Block #1	97.49 [°C]	Relative Error	125.73 [°C]	Relative Error
Block #2	95.82 [°C]	1.71 %	196.58 [°C]	36.0 %

Results presented in the two tables above show that the random algorithm used to fill the volume with RRs has an acceptably low relative error. This error has to be considered together with the Grid Independence error to address a total uncertainty error to the computed results. Specifically, the two motion fields of block #1 and block #2 are very close to each other, with a maximum error of 1.75% which can be also addressed to the pressure loss as it depends on the velocity field. Temperature wise, the values of the average outlet temperature of the air is, once again, very similar between the two block #1 and #2, with an error of 1.71%, however a bigger error is found for the average Glidcop temperature, this is probably due to some cells that have a much bigger maximum air and Glidcop temperature as the new block #2 may contain some stagnation points.